ABSTRACT

Title of Document: Smart Paint Sensor for Monitoring Structural Vibrations

                            Yaser Alsaffar, Masters of Science, 2010

Directed By: Professor Amr Baz, Mechanical Engineering

A class of smart paint sensors is proposed for monitoring the structural vibration of beams. The sensor is manufactured from an epoxy resin which is mixed with carbon black nano-particles to make it electrically conducting and sensitive to mechanical excitations. A comprehensive theoretical and experimental investigation is presented to understand the underlying phenomena governing the operation of this class of paint sensors and evaluate its performance characteristics. A theoretical model is developed to model the electromechanical behavior of the sensor system as a lumped-parameter system using the Debye and the Cole–Cole equations. The sensor equations are integrated also with a finite element model of a base beam to which the sensor is bonded to. The resulting multi-field model is utilized to predict the behavior of both the sensor and the beam when subjected to a wide variety of vibration excitations.

The predictions of the multi-field finite element model are validated experimentally and the behavior of the sensor is evaluated both in the time and the frequency domains. The performance of the sensor is compared with the performance of conventional strain gages to emphasize its potential and merits.

The presented techniques are currently being extended to sensors that can monitor the vibration and structural power flow of two dimensional structures.

Smart Paint Sensor for Monitoring Structural Vibrations

By

Yaser Alsaffar

Thesis submitted to the Faculty of the Graduate School of the
University of Maryland, College Park, in partial fulfillment
of the requirements for the degree of
[Masters of Science]
[2010]

Advisory Committee:
Professor Amr Baz, Chair
Professor Balakumar Balachandran
Professor Nikhil Chopra

Acknowledgements

Table of Contents

List of Figures

List of Tables

Chapter 1: Introduction

1.1 Overview

Considerable attention has been focused recently on the development of a wide variety of smart paints which can be used as sensors for vibration, noise, and health monitoring applications. These smart paints are radically different from conventional paints which have been traditionally used on structures for providing protective and decorative functions.

Distinct among the available types of smart paints are the smart piezoelectric composite paints which consist of piezoelectric powder embedded in epoxy resins to form the commonly known "0-3" composites to denote that the piezo-particles are randomly dispersed in the polymer matrix (Egusa and Iwasawa, 1998; Hall, 1998a,b; Hall and Tuck, 1999, Aggarwal *et al*., 2005; Zhang, 2005).

This class of paints has received a considerable acceptance as an effective class of sensors as it combines the attractive attributes of both the polymers and the piezoelectric particles. For example, these paints offer the high electro-active properties of the piezoelectrics and the mechanical flexibility of the polymers.

However, the piezoelectric composite must be coated with layers of electrodes and then poled using very high voltage to impart the sensing capability to the paint as shown in Figure 1.1. Such complex manufacturing processes make this type of paint very expensive. Furthermore, expensive charge amplifiers are needed to monitor the capacitive signals of the smart paint sensor.
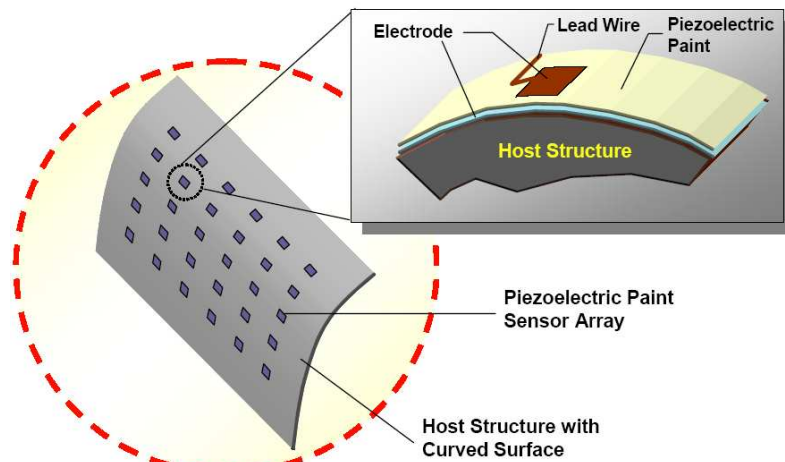
Figure 1.1: Smart piezoelectric composite paint (Zhang, 2005)

Alternatively, the pressure sensitive smart paints which modulate the light intensity through a repeatable chemical interaction of the sensing layer with atmospheric oxygen require the use of an expensive photodetector such as a CCD camera or photomultiplier tube for interrogation of the paint (Greogory *et al*., 2006).

Figure 1.2: Smart pressure sensitive paint (Gregory *et al*., 2006)

Inherently insulating polymers can be made conductive with the incorporation of electrically conducting fillers, which is usually attributed to percolation effect (Zhang and Zeng, 1997).

Carbon black (*CB*) composite is another class of functional material that finds wide applications, e.g., in deformation sensing. The composite consists basically of electrically conductive CB particles embedded in a polymer matrix. The composite conductivity noticeably changes with the applied mechanical deformation.

Extensive research effort has been put forth to studying the percolation theory which is often used to describe the relationship between *CB* contents and the direct current (DC) conductivity (Sichel, 1982). However, investigation of the sensing ability of *CB* composites is focused on the detection of quasi-static effect. For example, the work of Shevchenko *et al.* (1995) focused on graphite filled polypropylene composites, which possess smart properties, such as a positive temperature coefficient of resistance and strain dependent conductivity. Along a similar direction, Kimura *et al.* (1995) experimentally illustrated the linear relationship between the logarithms of the resistance and elongation. Furthermore, they developed a model based on the tunneling junction model. Flandin *et al.* (2000) evaluated the DC electrical and mechanical properties of composites composed of conductive fillers impeded into elastomer matrices. Zhang *et al.* (2001) presented a systematic work on the piezoresistance effects of electrically conducting composites which are subject to uni-axial pressure. The investigation experimentally verified the theoretical model for the piezoresistance. In another work, Zhang and the co-workers

(2000) investigated the time dependence of the piezoresistance of conductor-filled polymer composites. Knite *et al*. (2004) proposed the use of carbon black nanocomposites as tensile strain and pressures sensor. The investigation included experimental results and a theoretical model based on that of Zhang *et al* (2001). In a recent work, Wang *et al*. (2005) studied the conduction mechanism in *CB* composites using impedance spectroscopy. Three equivalent-circuit models are proposed for the various regions of percolation theory curve. Another group of investigators (Lu *et al*., 2006; Moshfegh and Ebrahimi, 2004) studied the piezoresistive behaviors of graphite composites under static pressures. Das *et al*. (2002) is focused on the variation of the resistivity of *CB* and short carbon fiber composites with the degree of strain at constant strain rate.

Recently, carbon nanotubes (*CNT*) have been embedded inside polymers to serve as conducting filler (Mahar *et al*., 2007). The strong dependence of the carbon nanotubes's Raman band structure on mechanical deformations serves as the basis for the development of a wide variety of nanotube-based strain sensors. For example, Zhao *et al*. (2001) used *CNT*-polymer composites to measure the stress field inside the polymer. They showed the potential of *CNT*/polymer composites as strain sensors by relating the stress/strain of the nanotubes to the Raman band shift. The complexity of the experimental setup makes it less attractive for practical in-field applications. In 2004, Li *et al*. developed thin films of nanotubes as strain sensors. In 2010, carbon nanotube forests were spun into a microscale thread which is electrically conductive mechanically strong, and can be easily integrated in polymeric matrices. The resulting

composite is used as a piezoresistive sensor to monitor strain and also to detect damage in the material (Abot *et al*., 2010).

Typical of any emerging and rapidly developing field, *CNT*/polymer composites are limited to a multitude of proof-of-concept prototypes. However, the complexity of operation and high manufacturing cost limit considerably their mass-production or in-field operation.

Therefore, the emphasis in this dissertation is placed on developing CB/polymer composites for vibration monitoring because of the simplicity of their operation and use. More importantly, CB/polymer composites are extremely attractive because of their low manufacturing cost.

1.2 Basics of Carbon Black Composites

1.2.1 Conductivity and percolation threshold

Electrically conducting polymer composites are developed by embedding conducting particles such as carbon black (e.g. Sichel, 1982), carbon fibers (e.g. Mahar *et el*., 2007), or micro-particles of metals (e.g. Bhattacharyya, 1986) into an insulating polymer matrix. Most often these polymer composites are used as electric heating elements or resistors, and recently as strain sensors as in the present study.

The invention of conductive polymers can be credited to Coler (1950) who introduced the first highly-conductive series of polymers which were mixtures of plastics with embedded conducting particles such as metal powders, carbon black or

coated plastics. An excellent review of the history and potential of conducting polymers is given by Inzelt (2008).

It is important to note that in metal-filled polymers, the metal particles remain isolated from each other and contribute very little to the conductivity to the composite, unless their concentration is very high. At high concentrations, the resulting composite becomes stiff and brittle to the extent that limits their practical application.

Therefore, carbon black polymer composites become extremely attractive alternative as the conductivity can be established with relatively low concentration of carbon black. Also, carbon black is typically very light in weight and blends quite readily in the polymer, it results in a composite that retain its structural integrity while maintaining the flexibility of the polymer matrix. Furthermore, carbon black/polymer composites are simple to operate as sensors and have very low manufacturing cost.

The underlying physical phenomena governing the operation of this class of conducting composites are rather interesting and intriguing. A brief summary of these basic phenomena is given in this section in order to gain an insight about the principles, requirements, and constraints which are necessary for effective operation of the class of composites and making these composites acquire conductivities that match those of metals.

However, it is important to recognize the factors that control the formation of the conductive polymer and influence its final structure in order to achieve optimal performance. Distinct among these factors are the shape and size of the conductive particles, the nature of inter-particle contact, and adhesion between particles and polymers. All these factors influence the electrical and mechanical properties of the polymer composites.

An important metric that quantify the conductivity of the polymer is called "*Percolation Threshold*". This threshold defines the concentration of the fillers that makes the polymer conductive. Generally, as the concentration of the filler (e.g. carbon black) increases, the conductivity of the composite increases or the resistivity decreases as shown in Figure 1.3.
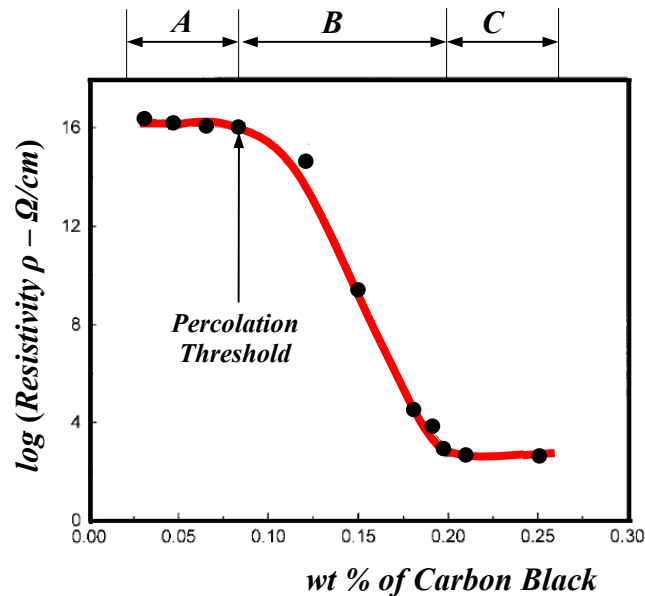
Figure 1.3: Effect of concentration of carbon black on resistivity of polymer composite

However, the rate of increase of the conductivity, or decrease of resistivity, is slow at low concentrations as shown in region *A* of Figure 1.3. The resistivity drops rapidly with further increase in the carbon black as it goes into region *B* where the rate of change increases by more than ten orders of magnitude. Further increase of the carbon black content fails to improve the resistivity as seen during region *C*.

It is important to physically understand the underlying phenomena that are behind such changes in the conductivity of the polymer matrix. At low CB contents, the gap between the CB particles, where the electrons are transmitted, is very large and the resistivity of the composite is approximately that of the polymer matrix. As the concentration increases, the "*percolation threshold*" is reached where the resistivity starts to decrease abruptly as a function of the CB loading. In this region, region *B*, the gap between the CB particles is close but not touching. As a result, the electron must overcome the potential barrier and cross the gap between the CB particles as shown in Figure 1.4.

(a) – CB particles/polymer   (b) – Equivalent circuit
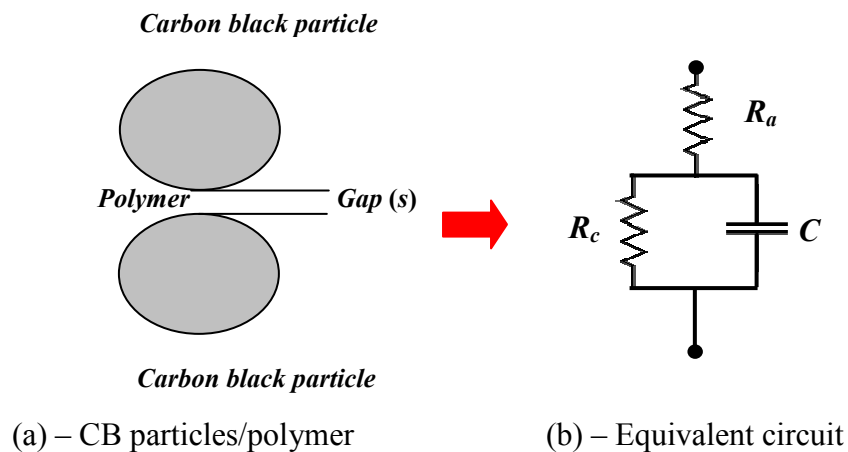
Figure 1.4: Interaction of carbon black and polymer in the percolation region B

The contact resistance (R_c) which is called "*non-ohmic resistance*" quantifies resistance for the passage of electrons through the gap between the CB particles. At the same time, the gap can be approximated by a parallel plate capacitor with an area A, separation distance s, and capacitance $C = \varepsilon A/s$, where ε is the dielectric constant of the polymer. Each CB particle has also a resistance (R_a), the resistance within the particle. The equivalent circuit that describes such an interaction is shown in Figure 1.4 b. The impedance of the equivalent circuit can be written as:

$$Z = R_a + \frac{1}{1/R_c + j\omega C} = R_a + \frac{R_c}{1+(\omega R_c C)^2} - j\frac{\omega R_c^2 C}{1+(\omega R_c C)^2} \quad (1.1)$$

or

$$Z == Z_R + jZ_I \quad (1.2)$$

where
$$Z_1 = R_a + \frac{R_c}{1+(\omega R_c C)^2}, \quad Z_2 = -\frac{\omega R_c^2 C}{1+(\omega R_c C)^2} \quad (1.3)$$

Equation (1.3) yields:

$$\left(Z_R - \frac{2R_a + R_c}{2}\right)^2 + Z_I^2 = \left(\frac{R_c}{2}\right)^2 \quad (1.4)$$

and
$$|Z| = \left(Z_R^2 + Z_I^2\right)^2, \quad \tan(\phi) = Z_I / Z_R \quad (1.5)$$

Equation 1.4 defines a circle which has the circle center at $\left[(2R_a + R_c)/2, 0\right]$ and a radius of $R_c/2$. This circle occurs only for the parallel resistor–capacitor circuit, thus can be used to confirm the existence of the capacitor effect which is in turn suggests the presence within the percolation region. Figure 1.5 shows such a circular

characteristics for CB/polyethylene composite with CB concentration of 15% (Wang *et al.*, 2005).

(a) – Z_R-Z_I Plot   (b) – Magnitude and phase angle
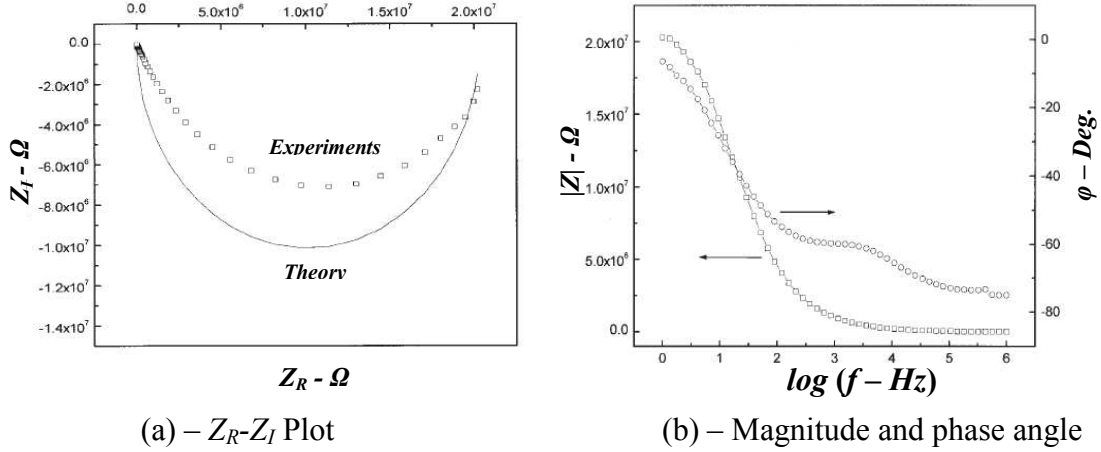
Figure 1.5: Impedance plot of *CB*/polyethylene composite with *CB* concentration of 15% in the percolation region B (Wang et al., 2005)

For higher concentration of *CB*, the gap between the particles is further reduced and the conduction mechanism between particles becomes due to strong contact between the *CB* particles. The classical conduction via ohmic contact chain becomes the leading mechanism of conduction instead of the tunneling in the percolation region where conduction via nonohmic contacting chains dominates. In this case, region *C*, the conduction mechanism and the equivalent electrical circuit are shown in Figure 1.6 where R_c disappeared and L is an inductance to quantify the *CB* chain effect. For this case, the equivalent electrical impedance is:

$$Z = R_a + jL\omega = Z_R + jZ_I \tag{1.6}$$

Hence, $$Z_R = R_a, \quad Z_I = L\omega \tag{1.7}$$

and $$|Z| = \left(Z_R^2 + Z_I^2\right)^2, \quad \tan(\phi) = Z_I / Z_R \tag{1.8}$$

10

(a) – CB particles/polymer   (b) – Equivalent circuit
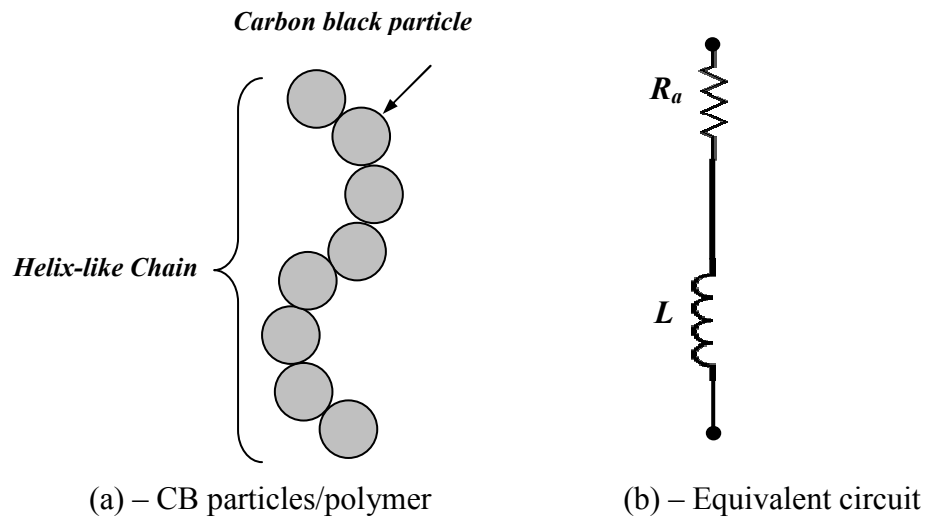
Figure 1.6: Interaction of carbon black and polymer in region C

Equation (1.7) defines equation of a straight line perpendicular to the Z_R axis as shown in Figure (1.7).

(a) – Z_R-Z_I Plot   (b) – Magnitude and phase angle
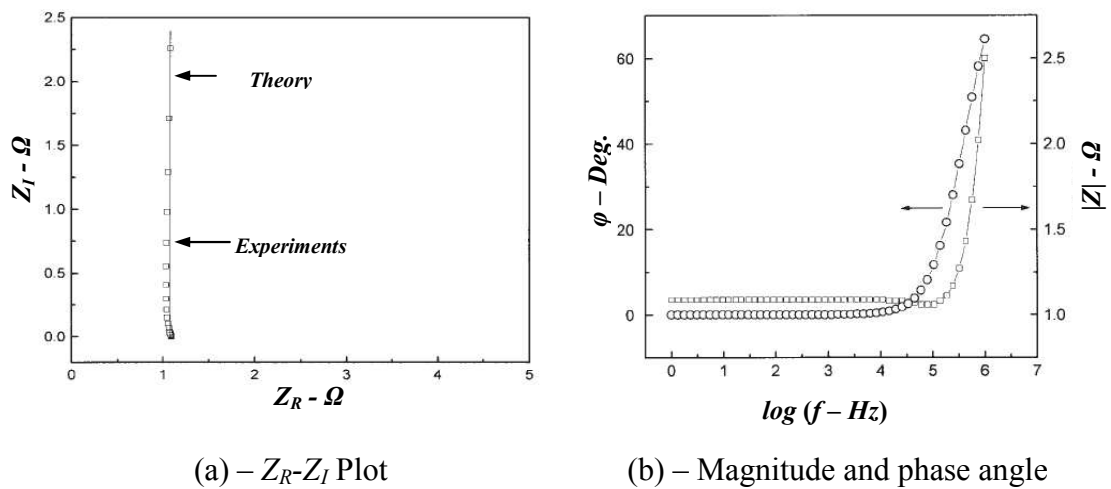
Figure 1.7: Impedance plot of *CB*/polyethylene composite with *CB* concentration of 25% in region C (Wang et al., 2005)

From the above characteristics, it can be seen that for the 15 wt% CB composite, the impedance spectra show that the impedance modulus and phase angle decrease with the increase of the frequency. Furthermore, the imaginary part of the impedance versus the real part of the impedance curve is nearly semicircular. However, the theoretical characteristics do not fit the experimental values exactly because the capacitor is assumed by Wang *et al*. (2005) to be frequency independent which is not true for *CB*/polymer composites.   This discrepancy will be corrected, as will be discussed in details, in Chapter 2.

For the 25 *wt*% *CB*/polymer composite, the impedance spectra show that both the impedance modulus and phase angle are stable until the frequency reaches 1MHz and both abruptly increase with further increase of the frequency. The imaginary part of the impedance versus the real part of the impedance curve is a perpendicular straight line of the real axis. This shape of the curve agrees with the prediction. Therefore, the model of the resistor-inductor series can be used to represent the conduction behavior of the composites at high loading and it is the inductance effect that determines the frequency dependence of the electrical property for the composites at high loading.

1.2.2 Piezoresistivity

Piezoresistivity is a property of conducting polymers which defines changes of the resistance of the polymers due to the application of stresses such as a pressure whether hydrostatic or uniaxial.

It is important here to note here that the piezoresistive effect differs from the piezoelectric effect. In contrast to the piezoelectric effect, the piezoresistive effect only causes a change in electrical resistance; it does not produce an electric potential as the piezoelectric effect.

Generally, the piezoresistance depends on the properties of the polymer matrix, filler properties and filler concentration, and applied load. An excellent account that describes the interactions between all these parameters and their effect on the piezoresistivity of the conducting polymer composite is given by Zhang *et al.* (2001). In their work, Zhang *et al.* developed a physics-based mathematical model to predict the piezoresistivity of polymers impregnated with 11 different fillers.

Figure 1.8 displays a schematic drawing of the micro-structure of a filler/polymer composite.
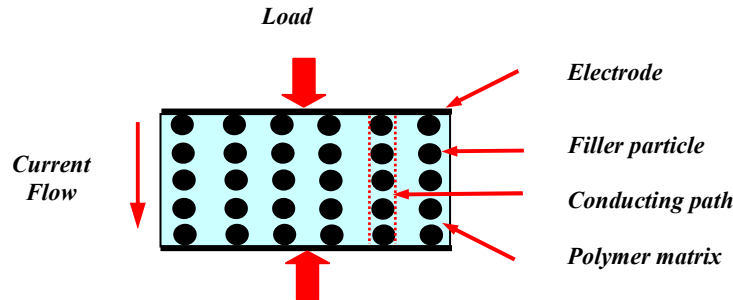
Figure 1.8: Schematic drawing of the micro-structure of a filler/polymer composite.

The total resistance *R* of one conducting path is given by:

$$R = \frac{L(R_c + R_a)}{S}$$ (1.9)

where R_c = resistance between two adjacent filler particles, R_a = resistance across on filler particle, L = number of particles forming one path, and S = number of conducting paths.

13

If the inter-particle separation is very large, no current flows. However, as the separation becomes adequately small, a current I will flow due to the application of a voltage V such that:

$$I = \frac{3\sqrt{2m\phi}}{2s}\left(\frac{e}{h}\right)^2 V e^{\left(-\frac{4\pi s}{h}\sqrt{2m\phi}\right)} \tag{1.10}$$

where m = electron mass, e=electron charge, h = Plank constant, s = separation between two adjacent particles, and ϕ=height of potential barrier between adjacent particles.

Assuming a^2 = the cross sectional area of the conducting particle, then the resistance R_c can be determined from:

$$R_c = \frac{V}{a^2 I} = \frac{8\pi hs}{3a^2\gamma e^2}e^{\gamma s} \tag{1.11}$$

where

$$\gamma = \frac{4\pi}{h}\sqrt{2m\phi} \tag{1.12}$$

Because the conductivity of the particles is very large compared with that between two adjacent particles, then $R_a \cong 0$, reducing equation 1.9 to:

$$R = \frac{L}{S}\frac{8\pi hs}{3a^2\gamma e^2}e^{\gamma s} \tag{1.13}$$

Equation 1.13 can be used to predict the resistance of the conducting polymer composite and it is clear that it varies exponentially with the separation distance s between the particles which is function of the applied load or strain experienced by the composite. This relationship will be used in Chapter 2 in modeling the behavior of the smart sensor and will be confirmed experimentally in Chapter 4.

14

Now, let us assume that the inter-particle separation changes from s_0 to s due to the application of stress, then the fractional resistance change $\left(-\Delta R/R_0\right)$ can be predicted from:

$$-\Delta R/R_0 = 1 - \frac{s}{s_0}e^{-\gamma(s_0-s)} \tag{1.14}$$

where R_0 is the original resistance. Note that s and s_0 can be related to the strain ε and the stress σ by the following relationships:

$$s = s_0\left(1-\varepsilon\right) = s_0\left(1-\frac{\sigma}{E}\right) \tag{1.15}$$

where E = modulus of elasticity of the polymer matrix.

The initial separation distance s_0 is estimated from:

$$s_0 = D\left[\left(\frac{\pi}{6}\right)^{\frac{1}{3}}\theta^{-\frac{1}{3}}-1\right] \tag{1.16}$$

where D = particle diameter and θ = volume fraction of filler.

Accordingly, equation (1.14) reduces to:

$$-\Delta R/R_0 = 1-\left(1-\frac{\sigma}{E}\right)e^{-\gamma D\left[\left(\frac{\pi}{6}\right)^{\frac{1}{3}}\theta^{-\frac{1}{3}}-1\right]\frac{\sigma}{E}} \tag{1.17}$$

Equation (1.17) predicts the piezoresistance changes of conducting polymer composite as function of the applied stress σ, modulus of elasticity of the polymer matrix $\boldsymbol{E}$, filler particle diameter $\boldsymbol{D}$, filler volume fraction θ, and the parameter γ.

Calculation of the parameter γ requires the knowledge of $\boldsymbol{m}$, $\boldsymbol{h}$, and ϕ. Note that the mass of the electron $\boldsymbol{m}$ = 9.180938E-31 kg, $\boldsymbol{h}$ = Plank constant = 6.626E-34 m^{2}kg/s, and ϕ is given in Table 1.1.

Table 1.1: Values of potential barrier height (Zhang *et al.*, 2001)

NO.	COMPOSITE		POTENTIAL BARRIER HEIGHT (*EV*)[*]
	Name	**Abbreviation**	
1	Copper/ Polystyrene	*Cu/PS*	0.39
2	Aluminum/ Polystyrene	*Al/PS*	0.55
3	Tin-lead/ Polystyrene	*Sn-Pb/PS*	0.57
4	Copper/polyethylene	*Cu/PE*	0.09
5	Aluminum/polyethylene	*Al/PE*	0.07
6	lead/polyethylene	*Sn-Pb/PE*	0.09
7	Carbon black/polyethylene	*CB/PE*	0.05
8	Tin-lead /epoxy	*Sn-Pb/epoxy*	023

*electron volt (*eV*) is a unit of energy = $1.602 \times 10{-}19\ J$

Figure 1.9 shows the effect of the applied **STATIC** stress on the fractional resistance changes $\left(-\Delta R / R_0\right)$ as predicted for three conducting polymer composites which are namely: copper/polyethylene (*Cu/PE*), Aluminum/polyethylene (*Al/PE*), and Carbon black/polyethylene (*CB/PE*).
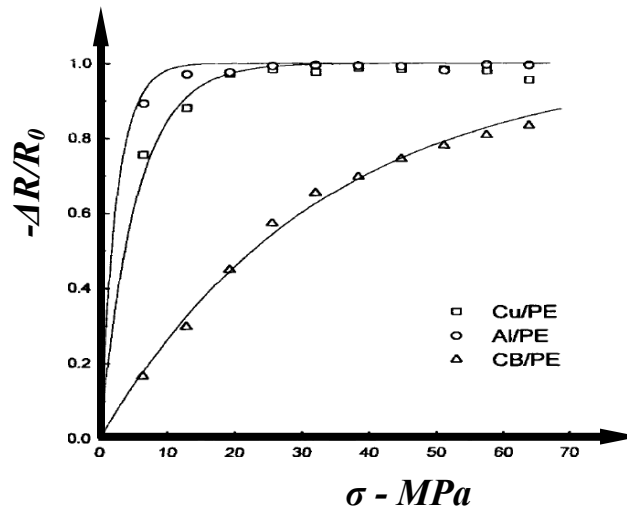
Figure 1.9: Effect of stress on the fractional resistance changes $\left(-\Delta R / R_0\right)$ for three conducting polymer composites

The figure indicates that, for the same applied stress, *Cu/PE* and *Al/PE* composites produce higher fractional resistance changes than *CB/PE* composite. However, the *CB/PE* composite has a wider linear range than both of the *Cu/PE* and *Al/PE* composites.   Such an important feature is one of the reasons for selecting the *CB/PE* composite as the viable candidate for smart paint sensor. The other reasons are attributed to the fact that in metal-filled polymers, such as *Cu/PE* and *Al/PE,* the metal particles remain isolated from each other and contribute very little to the conductivity to the composite, unless their concentration is very high. At high concentrations, the resulting composite becomes stiff and brittle to the extent that limits their practical application.

The effect of varying the concentration of the *CB* on the fractional resistance change is shown in Figure 1.10 as a function of the applied stress.
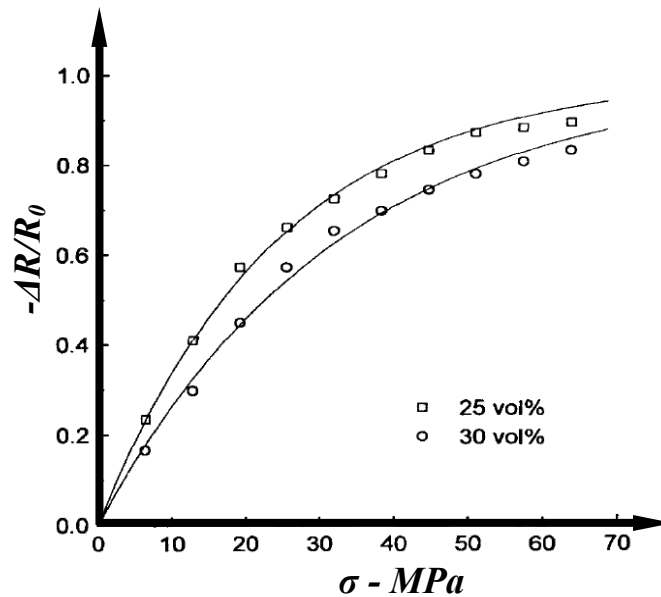
Figure 1.10: Effect of stress on the fractional resistance changes $\left(\Delta R / R_0 \right)$ for CB/PE composites with different *CB* concentration

1.2.3 Conducting polymer sensors

Extensive efforts have been exerted to develop a wide variety of conducting polymer sensors. Four examples of these sensors will be given here to illustrate their limitations as well as the challenges that need to be overcome in order to improve their performance.

In the first example, Wang and Chung (1996) developed a sensor made of unidirectional continuous carbon fiber embedded inside an epoxy matrix. The sensor performance when subject to unidirectional cyclic loading is shown in Figure 1.11. It is very clear that the sensor is incapable of tracking accurately the actual state of strain of the structure even under the considered unidirectional cyclic loading.
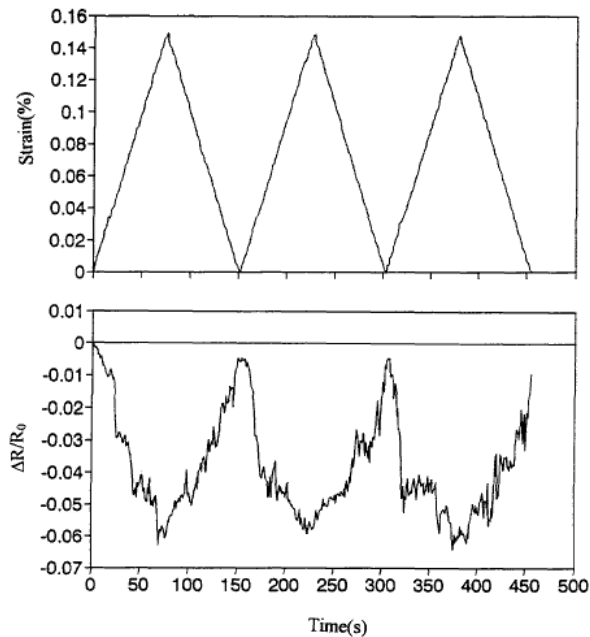
Figure 1.11: Performance of carbon fiber/epoxy sensor subjected to unidirectional cyclic loading (Wang and Chung, 1996)

In the second example, Loh *et al*. (2008) developed a single-walled carbon nanotube-polyelectrolyte composite thin film strain sensor fabricated by a layer by-layer process. The performance of the sensor is shown in Figure 1.12 when it is subjected to bidirectional reversible loading cycle. The sensor could not track the true strain and suffered from a continuous drift.
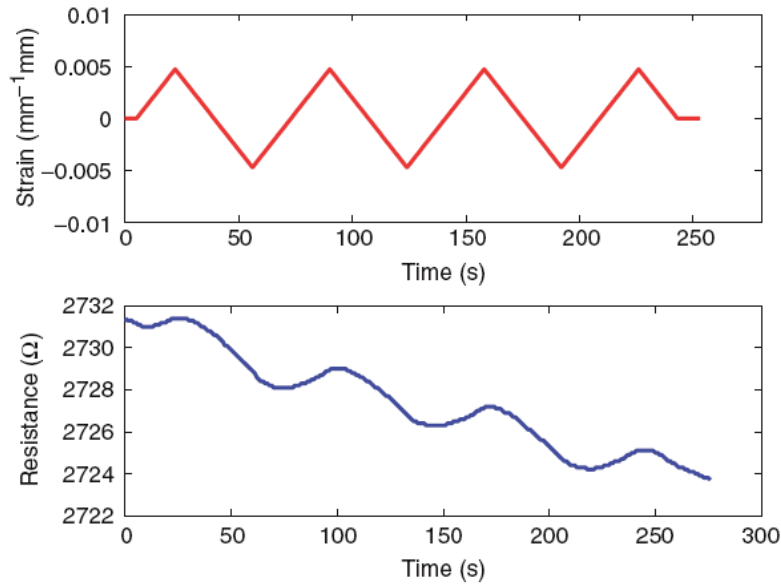
Figure 1.12: Performance of carbon nanotube/ polyelectrolyte sensor subjected to bidirectional cyclic loading (Loh et al., 2008)

In the third type of sensors, Hyatt (2010) developed a nano-composite strain gage material which is manufactured by suspending nickel nano-strands within a silicone matrix. The sensor performance when subject to unidirectional cyclic loading is shown in Figure 1.13. It is clear that the sensor output replicates the actual strain, as measured by the optical marker tracking sensor, but its wave form is distorted particularly near the peaks.
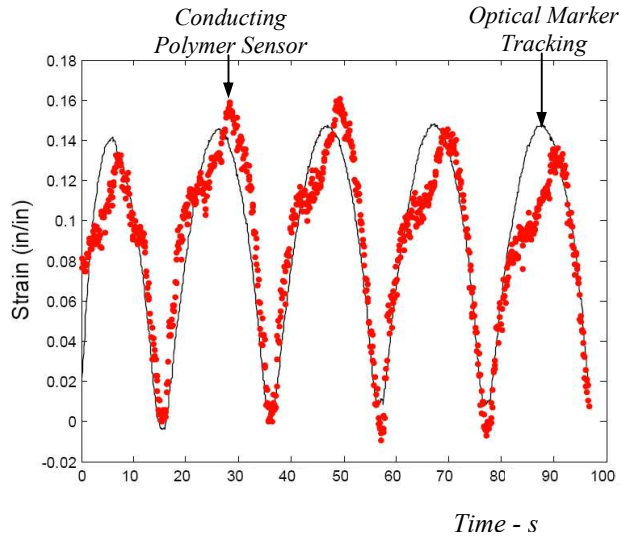
Figure 1.13: Performance of a conducting nickel nano-strands/silicone composite sensor subject to unidirectional cyclic loading (Hyatt, 2010)

In the fourth class of sensors, Mainwaring et al. (2008) developed a thin film sensor which consists of semiconducting carbon nanoparticles embedded inside polyimide polymer. The performance of the sensor under bidirectional loading is shown in Figure 1.14. Note the high nonlinearity and the asymmetry exhibited by the sensor output.
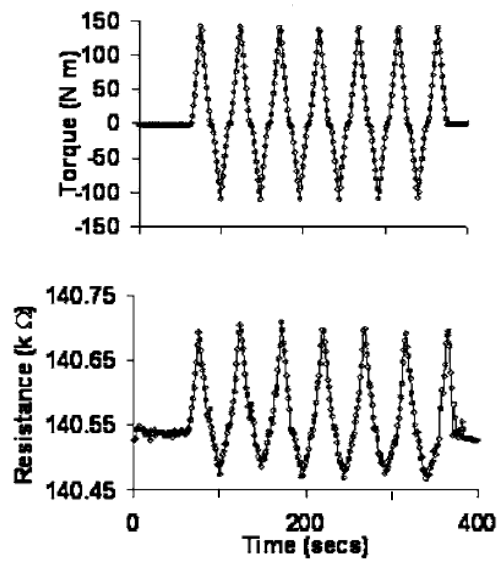
Figure 1.14: Performance of a conducting carbon nano-particles/polyimide composite sensor subject to bidirectional cyclic loading (Mainwaring et al., 2008)

From all the above examples, it is evident that the different types of conducting polymer sensors exhibit one or more of the following characteristics:

a. inaccurate tracking of the true strain state.

b. distortion of the shape of the wave form of the true strain.

c. inaccurate tracking of bidirectional cyclic loading in particular.

d. Nonlinear behavior and asymmetric behavior when measuring bidirectional cyclic loading in particular.

In this dissertation some of these serious limitations will be addressed.

1.3 Scope of the Thesis

In this work, smart paint sensors consisting of carbon black nanoparticles embedded in polymer matrix will be developed, analyzed, and tested. The proposed paint sensor is very simple and capable of monitoring vibration and noise down to a quasi-static frequency of ≈ 0 Hz. Accordingly, simple electrical circuits can be used to measure the changes in the current and voltage developed by the paint sensor.

It is also important to mention that the proposed paint sensor can be easily applied to structures of complex shapes and can act as a continuously distributed sensor over very large areas of structural surfaces. Furthermore, the proposed paint sensor can be used in numerous applications ranging from monitoring infrastructures, payload fairings of launching vehicles, flexible space structures, as well as many other critical structures that are only limited by our imagination.

In the present study, the objective is to model of the performance of the paint sensor system for vibration monitoring applications. A lumped-parameter as well as

finite element models will be developed. The developed models are verified experimentally by examination of the impedance spectrum, piezoresistance, and dynamic response.

The dissertation is organized in six chapters. Chapter 1 briefly summarizes the literature review. In chapter 2, a lumped-parameter model of the paint sensor is developed using the Debye and Cole-Cole equations. Chapter 3 presents details of the procedures which were adopted for manufacturing the sensor. In chapter 4, the experimental performance of the sensor is determined when array of sensors are bonded to beams subjected to bidirectional cyclic loading. In Chapter 5, a finite element model is developed for the sensor/beam assembly. Validations of the predictions of the developed models against the experimental results are also presented in this chapter. Chapter 6 summarizes the major conclusions and recommendations of the present study.

1.4 Summary

This chapter has presented the basic concepts of conducting polymers, a brief review of the literature of the underlying phenomena governing the operation of conducting polymers, conducting polymer sensors, as well as the limitation and challenges of the current conducting polymer sensor technology. The reasons for focusing on the use of carbon black/polymer composite sensors are outlined as compared to other types of conducting polymer sensors which may rely on metal particles, carbon nanotubes, or carbon fiber/polymer composites.

Chapter 2: Theory of Simple Smart Paint Sensor

2.1 Overview

This chapter presents a lumped-parameter modeling of the smart paint sensor. The modeling is based on the analysis of two equivalent circuits for the paint sensor, These circuits are called the Debye and Cole-Cole models. Then the electrical components including capacitance and resistance are estimated using the impedance equations.

An eletromechanical model is derived for the paint sensor system using Hamilton's principle. The model is based on an equivalent circuit representation which treats the real sensor system as a lumped-parameter system. The sensor system equations are integrated with a simple electrical circuit to enable the measurement of the current and voltage developed by the functional paint sensor.

Using the developed equivalent electromechanical models, predictions of the static and dynamic performance are presented along experimental validations.

2.2 Modeling of Smart Paint Sensor

The paint sensor is basically an electromechanical transducer which can be described by the constitutive (characteristic) equations of the sensor and the equations of motion of sensor structure along with the associated boundary conditions. The equivalent lumped-parameter approach can be used to replace the system governing equations with a lumped-parameter electrical circuit whose elements physically

represent the sensor electromechanical properties such as the capacitance, resistance, mass, stiffness, and damping Hilmans (1996). The equivalent circuit method is attractive in the sense that the sensor system can be cast in a single representation. Furthermore, the equivalent circuit method is often used to model and analyze coupled domain devices including electrostatic transducers (Nadal-Guardia *et al.* (2003), piezoelectric devices (Ikeda, 1996), ionic polymer (Newbury and Leo, 2003), and electroacoustic devices (Rossi, 1988).

Two equivalent circuit modeling methods for the paint sensor are presented her. These models include:

2.2.1 Debye model

The equivalent electrical circuit of the Debye model is shown in Figure 2.1.
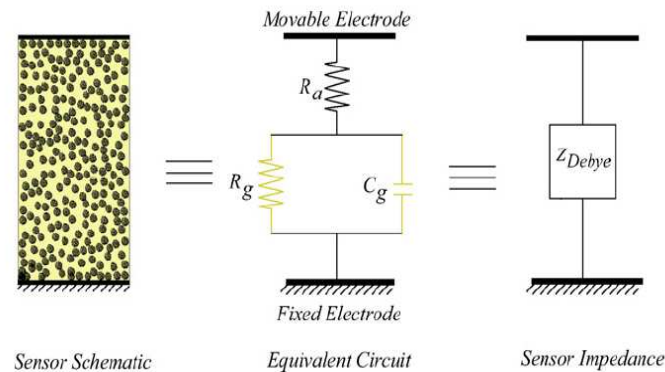
Figure 2.1: Debye model of the smart paint

The circuit consists of two resistances (R_a, R_g) and one capacitance (C_g). The R_g and C_g are resistance and capacitance in the gap between the carbon black particles. The R_a is the overall resistance of the carbon black particles. The R_g and

C_g are connected in parallel circuit and the R_a is connected to the parallel circuit in series.

Therefore, the equivalent total impedance of the modeling circuit is the following:

$$Z_{Debye} = R_a + \frac{R_g}{1 + j\,\omega\,\tau} \tag{2.1}$$

with

$$\tau = R_g C_g, \quad j = \sqrt{-1} \tag{2.2}$$

where $\omega\ (= 2\pi f)$ is the angular frequency and τ is the characteristic time of the equivalent circuit. The real and imaginary parts of the Debye impedance (2.1) can be extracted respectively as

$$Z'_{Debye} = R_a + \frac{R_g}{1 + (\omega\,\tau)^2}$$

$$Z''_{Debye} = -\frac{\omega\,R_g\,\tau}{1 + (\omega\,\tau)^2} \tag{2.3}$$

The ideal components R_a, R_g and C_g can be estimated from the values of Z'_{Debye} and Z''_{Debye}. At low frequency, the value of the real part is $R_a + R_g$, however, this value reduces to R_a at very high frequency. When the frequency reaches $\frac{1}{\tau}$, the imaginary part attains a maximum value of $Z''_{max} = Z''_{Debye}\left(at\ \omega_{max} = \frac{1}{\tau}\right) = -\frac{R_g}{2}$. At this frequency, ω_{max}, the capacitance of the composite can be calculated via $C_g = \frac{1}{R_g \omega_{max}}$.

2.2.2 Cole-Cole model

The Debye model is useful in describing a composite sensor with impedance possessing frequency independent parameters. When the matrix of the composite sensor is made of polymer, the impedance parameters become frequency dependent. For such a case, a good representation can be obtained by the Cole-Cole empirical equation;

$$Z_{C-C} = R_a + \frac{R_g}{1 + (j\omega\tau)^\alpha} \qquad (2.4)$$

where α is a dimensionless positive parameter with values in the range, $1 \geq \alpha \geq 0$. Using *De Moivre* identity, $j^\alpha = \cos(\alpha\pi/2) + j\sin(\alpha\pi/2)$, the impedance (2.4) is expanded as

$$Z_{C-C} = R_a + \frac{R_g}{1 + \omega^\alpha\tau^\alpha \cos(\alpha\pi/2) + j\omega\left(\dfrac{\omega^\alpha}{\omega}\tau^\alpha \sin(\alpha\pi/2)\right)} \qquad (2.5)$$

Letting $\tau = R_g^{1/\alpha} C_g$, the impedance (2.5) is reduced to

$$Z_{C-C} = R_a + \frac{1}{\dfrac{1}{R_g} + \dfrac{1}{r_\omega} + j\omega c_\omega} \qquad (2.6)$$

with frequency dependent resistor and capacitor given by

$$r_\omega = \frac{1}{\omega^\alpha C_g^\alpha \cos(\alpha\pi/2)}$$

$$c_\omega = \frac{\omega^\alpha}{\omega} C_g^\alpha \sin(\alpha\pi/2) \qquad (2.7)$$

26

where R_a, R_g and C_g are frequency independent elements. The real and imaginary parts take form similar to those of the Debye model (2.3) and are given respectively as

$$Z'_{C-C} = R_a + \frac{R_e}{1+\left(\omega\,\tau_w\right)^2}$$

$$Z''_{C-C} = -\frac{\omega\,R_e\tau_\omega}{1+\left(\omega\,\tau_w\right)^2}$$

(2.8)

where

$$\tau_\omega = R_e\,c_\omega, \quad R_e = \frac{R_g r_\omega}{R_g + r_\omega}$$

(2.9)

The equivalent circuit of the Cole-Cole impedance (2.6) can be represented graphically, as shown in Figure 2.2. In Cole-Cole model, four parameters should be estimated; R_a, R_g, C_g and α. The dimensionless positive number α is obtained from fitting the data. The components R_a, R_g and C_g can be estimated from the values of Z'_{C-C} and Z''_{C-C}. For $\alpha = 1$, it should be clear that the resistor term in (2.6), $1/\,r_\omega$, vanishes and the capacitor, c_ω, becomes C_g leading to the Debye model.
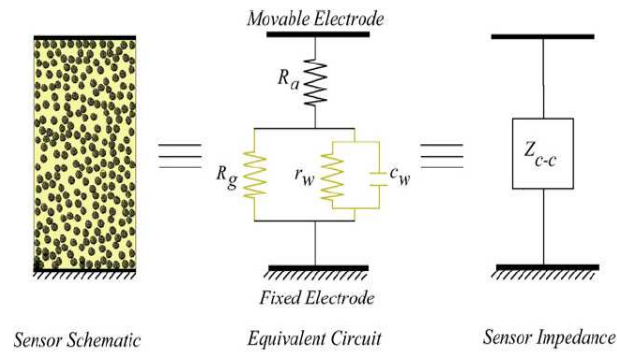
Figure 2.2: Cole-Cole model of the smart paint

2.3 Governing Equations of the Sensor System

The sensor system can be represented schematically as depicted in Figure 2.3.
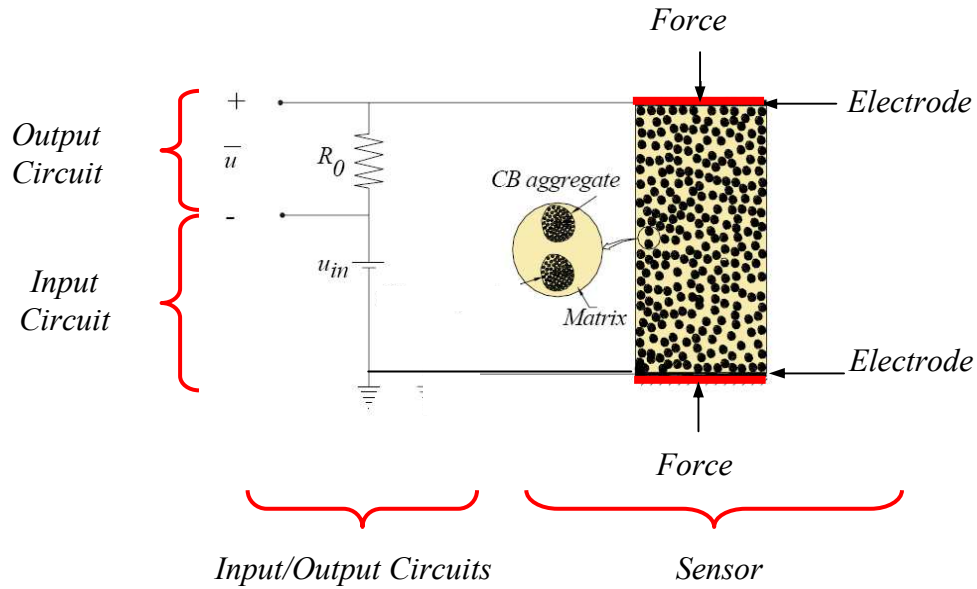
(a) – electrical components
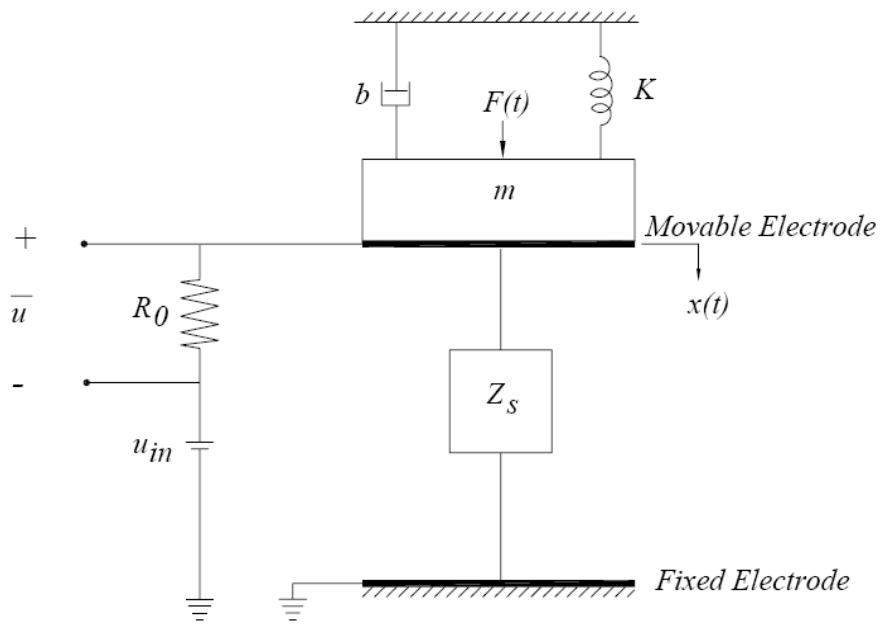
(b) - electrical and mechanical components

Figure 2.3: Schematic drawing of the sensor system

The sensor system enables the measurement of the current and/or voltage developed by the paint sensor as shown in Figure 2.3a. A voltage source, u_{in}, along with a series resistor, R_0, is used to bias the sensor. When the sensor is subject to external vibration excitations, its electrical properties are altered and so are the current and voltage of the bias resistor. The resulting changes are proportional to the external excitations.

In this chapter, the sensor is modeled using a lumped-parameter approach which treats the mechanical domain as a single degree of freedom system. The Debye or the Cole-Cole circuits are utilized to simulate the sensor electrical domain. Depending on which circuit is used, the sensor impedance, Z_s, can be taken from the Debye (2.1) or the Cole-Cole (2.6) equation. The mechanical elements are the equivalent mass, m, the equivalent stiffness, K, and the equivalent damping coefficient, b as shown in Figure 2.3b. When the sensor is disturbed by a force $F(t)$, the mass is displaced by an amount $x(t)$. The mechanical disturbance is converted into electrical current signal which flows in part through the resistor, R_0, thereby changing the output voltage $\bar{u}(t)$. This voltage is considered as measure for the force or velocity.

When the sensor is electrically and mechanically unloaded, the distance between the two electrodes is x_0. But, when the sensor is subjected to only a DC bias voltage, the bias voltage generates an attractive force between the electrodes and an equilibrium state is attained. At the equilibrium state, the two electrodes are separated by a distance x_{dc}, and the sensor is deformed by a distance $d = x_0 - x_{dc}$. The

equilibrium distance x_{dc} is obtained by balancing the sensor stiffness force with the electrostatic force of the dc bias. This is derived as

$$K d = \frac{Q_{dc}^2}{2 \varepsilon A} \Rightarrow x_{dc} = x_0 - \frac{Q_{dc}^2}{2 K \varepsilon A} \tag{2.10}$$

where Q_{dc} denotes the charge in the sensor electrodes due to dc bias, ε denotes the effective permittivity of the sensor, and A denotes the area of the electrodes.

Hamilton's principle for electromechanical systems will be used to derive the governing equations of the sensor system. In the interest of simplicity, the derivation will only consider the Debye equivalent circuit of the sensor as shown in Figure 6. Hamilton's principle yields the following Lagrange's equation for the electromechanical systems (Premount, 2006):

$$\frac{d}{dt}\left(\frac{\partial L}{\partial \dot{z}_i}\right) + \frac{\partial D}{\partial \dot{z}_i} - \frac{\partial L}{\partial z_i} = P_i$$

and
$$\frac{d}{dt}\left(\frac{\partial L}{\partial \dot{\overline{Q}}_k}\right) + \frac{\partial D}{\partial \dot{\overline{Q}}_k} - \frac{\partial L}{\partial \overline{Q}_k} = E_k \tag{2.11}$$

with the Lagrangian given by

$$L = T^* - V - W_e \tag{2.12}$$

The Lagrangian (2.12) accounts for all the conservative elements in the system and

$$\delta W_{nc} = \sum_{i=1}^{n} P_i \, \delta z_i + \sum_{k=1}^{l} E_k \delta \overline{Q}_k \tag{2.13}$$

is the virtual work of all non-conservative elements. Where P_i includes all the non-conservative mechanical loads which are not accounted for in the dissipation function, and E_k denotes the non-conservative voltage.

With reference to Figures 2.4, the electrical charges in the sensor system are given by

$$\overline{Q}_1(t) = Q_{1dc} + Q_1(t)$$

(2.14)

and

$$\overline{Q}_2(t) = Q_{2dc} + Q_2(t)$$

where Q_{idc} $(i = 1, 2)$ is the charge due to a DC bias and $Q_i(t)$ is the charge created by the excitation.
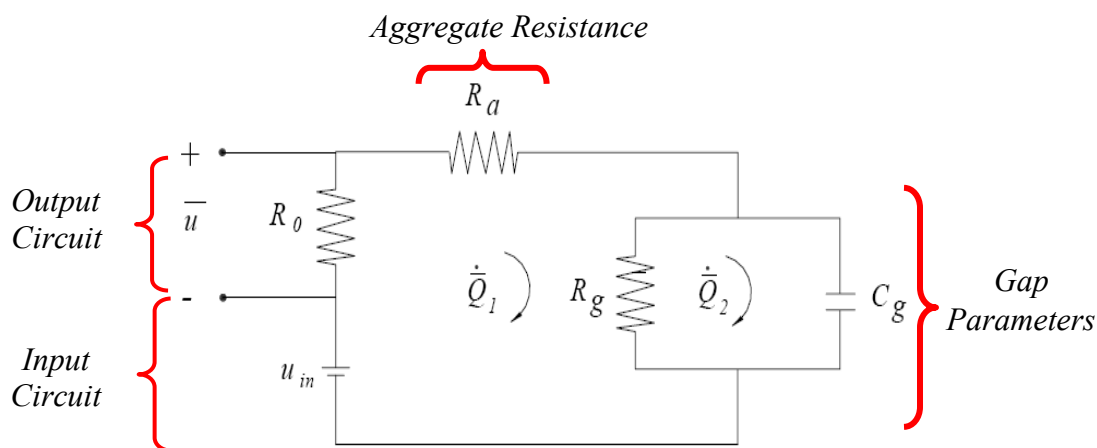
Figure 2.4: Electrical circuit of the sensor system

For Debye model, the various energy contributions to the Lagrangian are

$$T^* = \frac{1}{2}m\,\dot{x}^2$$

$$V = \frac{1}{2}K(x+d)^2$$

(2.15)

31

and
$$W_e = \frac{1}{2\,C_g} \overline{Q}_2^{\,2}$$

where T^* is the kinetic energy, V is the potential energy, and W_e is the electrical energy of the sensor system.

With reference to Figures 2.3 and 2.4, the dissipation energy function is given as

$$D = \frac{1}{2}\left(b\,\dot{x}^2 + (R_0 + R_a)\dot{\overline{Q}}_1^{\,2} + R_g\left(\dot{\overline{Q}}_1 - \dot{\overline{Q}}_2\right)^2 \right) \tag{2.16}$$

and

$$\delta W_{nc} = F(t)\delta x + u_{in}\,\delta\overline{\overline{Q}}_1 \tag{2.17}$$

The capacitance of the overall gap, C_g, varies with displacement of the movable electrode about the equilibrium position according to

$$C_g = \frac{\varepsilon\,A}{x_{dc} - x(t)} \tag{2.18}$$

Furthermore, the overall gaps resistance R_g varies with the sensor deformation according to Chapter 1 (equations 1.11 through 1.17) and to Zhang *et al.* (2001)

$$R_g = R_{gdc}\left(1 - \frac{x(t)}{x_{dc}}\right)e^{-\gamma s_0\left(\frac{x(t)}{x_{dc}}\right)} \tag{2.19}$$

with

$$\gamma = \frac{4\pi}{h}\sqrt{2\,m_e\varphi} \tag{2.20}$$

$$s_0 = D\left(\sqrt[3]{\pi/6\theta} - 1\right) \tag{2.21}$$

where R_{gdc} is the overall gap resistance at equilibrium, D is the CB aggregate diameter, θ is the CB volume fraction, h is the Plank constant, m_e is the electron mass, and φ is the height of the potential barrier between adjacent carbon black aggregates.

Using equations (2.14) through (2.18) in the Lagrange's equation (2.11) and carrying out some mathematical manipulations yields the governing equations:

$$m\,\ddot{x} + b\,\dot{x} + K\,x - \frac{Q_{2dc}}{\varepsilon\,A}Q_2 = F,$$

$$\left(R_0 + R_a\right)\dot{Q}_1 - R_g\left(\dot{Q}_2 - \dot{Q}_1\right) = 0, \tag{2.22}$$

and

$$R_g\left(\dot{Q}_2 - \dot{Q}_1\right) + \frac{x_{dc}}{\varepsilon\,A}Q_2 - \frac{Q_{2dc}}{\varepsilon\,A}x = 0.$$

The above equations (2.22) represent the nonlinear dynamic behavior of the sensor system. The nonlinearity is seen in the terms containing R_g where $x(t)$ is embedded. The displacement, $x(t)$, is coupled with the electrical charge $Q_2(t)$ via the electromechanical coupling factor $\dfrac{Q_{2dc}}{\varepsilon\,A}$. Furthermore, the displacement, $x(t)$ which is hidden in the R_g terms, can affect the electrical response of the system.

In general, the output voltage drop in the resistor R_0 and the voltage across the paint sensor are available for measurement. Since they differ only by the excitation voltage, which is known u_{in}, it is sufficient to consider only one of them. The voltage drop in the resistor R_0 is given as

33

$$\bar{u} = R_0 \ddot{Q}_1 \tag{2.23a}$$

or

$$\bar{u} = u_{dc} + u(t) = R_0 \dot{Q}_{1dc} + R_0 \dot{Q}_1 \tag{2.23b}$$

The first term in (2.23b) is the voltage drop in the resistor at equilibrium, while the second term is due to the mechanical excitation. Solving the system (2.22) for a given excitation $F(t)$ provides solutions for $x(t)$, $Q_1(t)$, $Q_2(t)$ and their derivatives. This solution set can readily be used to obtain $u(t)$ and $\bar{u}$.

2.4 Verification of Models

a. Impedance spectrum

To obtain quantitative information from the sensor model presented in section 2.3, one must first determine values for several electrical parameters. Experimental impedance spectroscopy is employed in this work to verify the validity of the Debye and Cole-Cole models and to obtain the electrical parameters. All of the experiments were performed on a paint sensor which consists of 10% *wt CB* aggregates embedded in a polyurethane matrix. A Tissue Tearor mixer (Model 985370, BIOSPEC Products, Inc., Bartlesville, OK, (http://www.biospec.com) is used to ensure the homogeneity of the paint.

The CB used was acetylene black, from Alfa Aesar Company, with an average particle size 42-nm, a surface area $75\,m^2/g$, a density $1.75\,g/cm^3$ and a bulk density

94.5-102.5 kg/m^3. The matrix used was 60A polyether based urethane, from Forsch

Polymer Corp., with a density 1.08 g/cm^3 and an elastic modulus 2-3.8 MPa. The

loss factor of the urethane is 0.14, which was obtained experimentally. The relative

dielectric constant of the urethane is 5.0-8.8.

Samples were fabricated by hand mixing the urethane and CB and pouring the

mixture in a metal mold for one day. The samples were then cut into disk shape,

coated with surface electrodes made of conductive silver paint, and connected with

leads. The samples were 24.6-mm diameter and 0.942-mm average thickness. Details

of manufacturing the sensor samples are given in Chapter 3.

The impedance spectra were measured at room temperature using impedance

analyzer, Hewlett Packard 4192A LF, over the frequency range from 5 Hz to 4 MHz.

The analyzer was set on a series mode, and the samples were excited by a signal with

amplitude of 50 mV

.

Figure 2.5 shows the real Z' and imaginary Z'' impedance spectrum in the

frequency range from 5 to 4×10^6 Hz. The figure contains plots from the

experiments, Debye and Cole-Cole models. The Debye curves are calculated using

equation (2.3) and values of R_a, R_g and C_g that best fit the experimental data and as

described in section 2.2.1. Similarly, the Cole-Cole spectra are determined using

equation (2.8) and values of R_a, R_g, C_g and α that best match the experiments and as

described in section 2.2.2. The evaluated values of the parameters are given in Table 2.1.
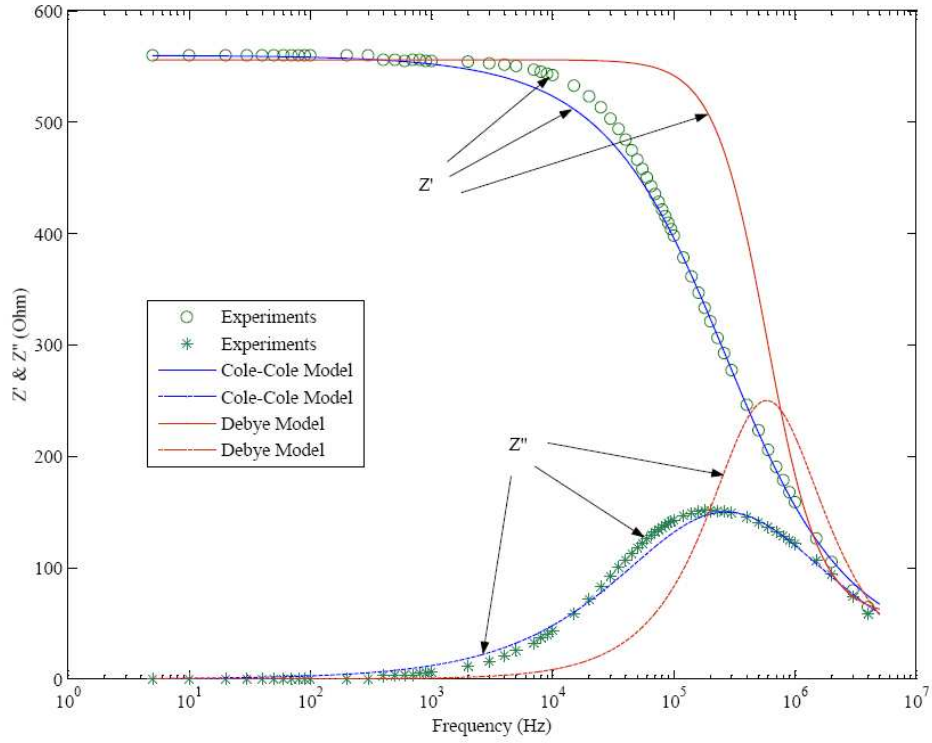
Figure 2.5: Real and imaginary impedance spectra of smart paint

Table2.1: Estimated electrical parameters of equivalent circuits (Mechanically unloaded).

MODEL	R_G (Ω)	R_A (Ω)	C_G $(\times 10^{-11}\,\mathrm{F})$	α
Debye (50 mV excitation)	500	56	54.332	-
Cole-Cole (50 mV excitation)	540	20	3.4332	0.645
(3 V excitation)	485	15	3.461	0.655

36

When compared to the experimental results, it is observed that the Debye model provides good predictions for frequency range less than one kHz. On the other hand, the Cole-Cole predictions agree quite well with the experimental results for all frequencies. Furthermore, Figure 2.5 shows that the imaginary impedance Z'' is close to zero at frequency below one kHz. This indicates that the current bypasses C_g and flows only thru R_g branch.

To further confirm the validity of the models, the results are plotted in the complex impedance spectrum as shown in Figure 2.6. Here again the Cole-Cole results agree well with those of the experiments, while the Debye curve matches the experimental data only at low and very high frequencies.
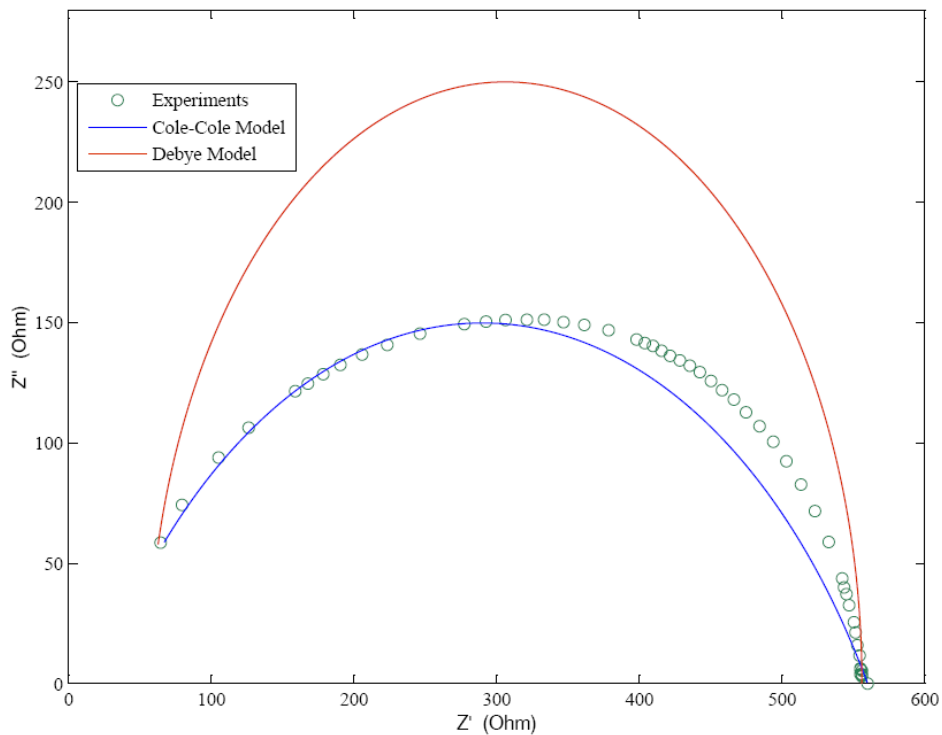
Figure 2.6: Complex impedance spectra of smart paint

Since the proposed sensor system operates under the influence of an external DC excitation, the effect of a DC bias on the impedance spectrum is also investigated. Figure 2.7 shows the complex spectrum of a paint sensor biased by a signal with amplitude of 3 V. At low frequency, it can be seen that the presence of a bias voltage reduces the values of R_a and R_g when compared with those of an unbiased sensor. The bias voltage creates attractive force between adjacent aggregates which decreases the separation distance and the sensor resistance. At very high frequency, the bias voltage has no effect on the impedance.
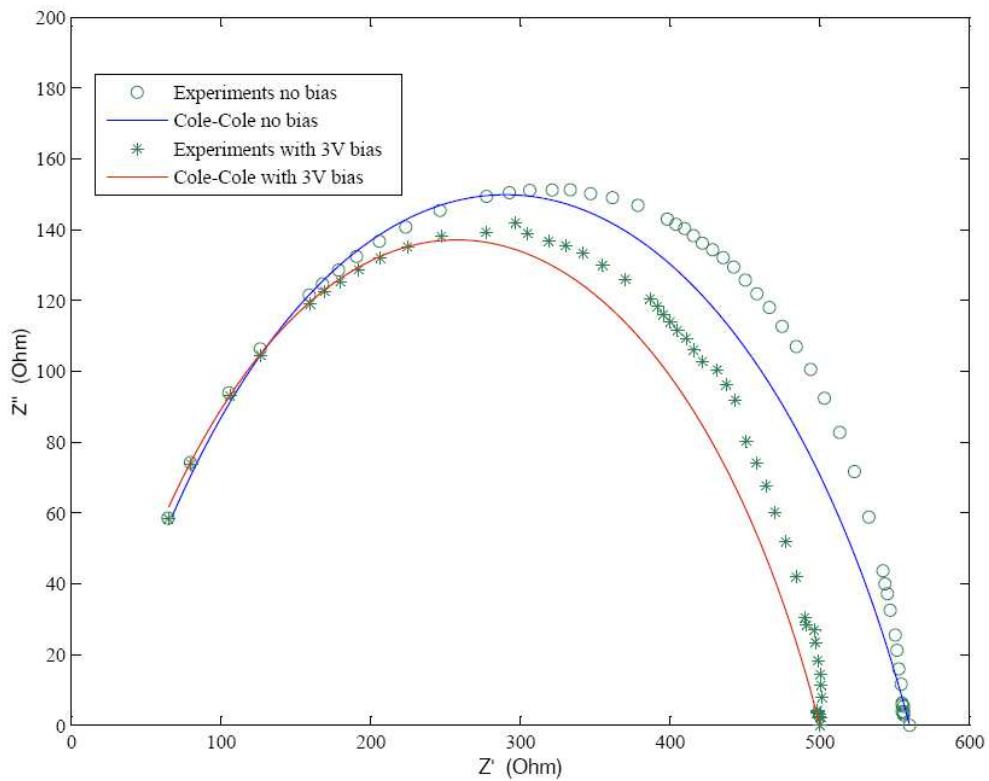
Figure 2.7: Complex impedance spectra of smart paint biased by a 3V signal

2.5 Piezoresistance

The paint sensor described in section 2.3 is used here to verify the piezoresistance model (2.19). The sensor is subjected to compressive stresses created by weights, and the sensor resistance was measured by a digital multimeter. Figure 2.8 shows the measured and the predicted relative resistance change as function of the applied stress. Clearly, the predicted results are in good agreement with the experiments verifying the validity of the model (2.19). At small applied stress, the results show that the relative resistance varies almost linearly with the compression stress.
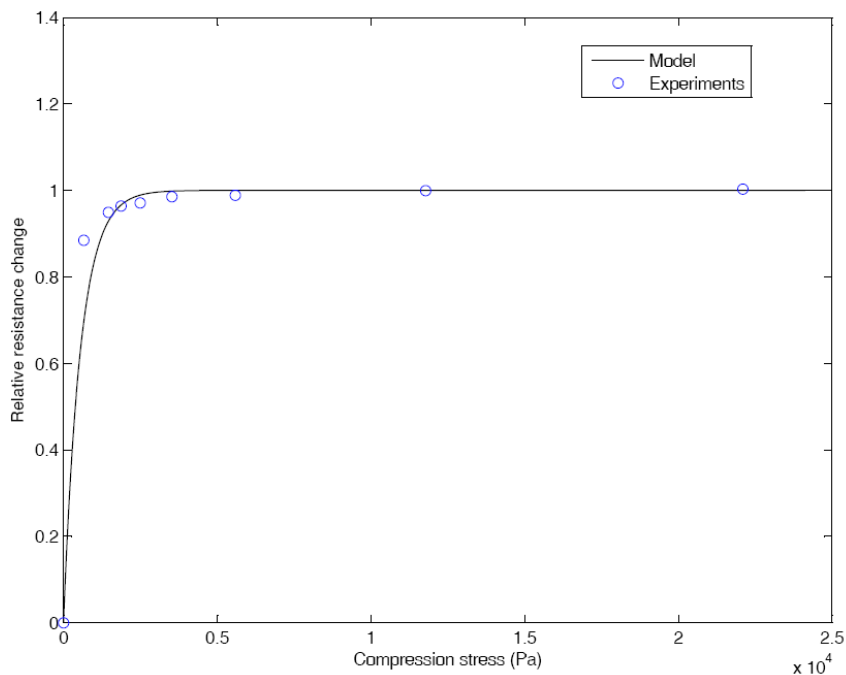
Figure 2.8: Complex Measured and predicted relative resistance changes

2.6 Summary

In this chapter, a simple model is presented representing the paint sensor as a resistance connected in series with parallel RC elements. Two different modeling equations, Debye and Cole-Cole is used in modeling the electrical circuit. Debye is for the impedance representation independent from frequency while Cole-Cole is for the impedance representation dependant from frequency. Using the Hamilton's Equation, the coupling between eletromechanical constitutive equations were developed. This model reveals nonlinear relationship between the electrical and mechanical variables. The nonlinearity is caused by the gap resistance. In comparisson with experimental data, the Debye model shows a reasonable minic in frequency below 1kHz while Cole-Cole model shows a matching results in all frequencies. The study shows the validation of the piezoresistive effect of the sensor.

Appendix A – Mechanical Elements

The mechanical elements of the composite sensor are represented in Figure 2.4 by K, m, and b. For an axial bar, an expression for the mechanical equivalent stiffness can be derived by considering the quasi-static relationship between applied force and the produced deformation. For small deformations, the axial load and the deformation are related through

$$F = \frac{E'A}{x_0} x \tag{A.1}$$

with (Zhang and Yi, 2002)

$$E' = E'_p \left(1 + 2.5\,\phi + 14.1\,\phi^2 \right) \tag{A.2}$$

where E' is the sensor elastic (storage) modulus (the elastic modulus of the composite sensor is complex due to the polymer matrix), E'_p is the elastic (storage) modulus of the polymer matrix, and ϕ is the volume fraction of the CB filler.

Equation (A.1) leads to the sensor equivalent stiffness

$$K = \frac{E'A}{x_0} \tag{A.3}$$

Similarly, the equivalent mass of the sensor is obtained for composite bar. This is achieved by combining the quasi-static bar stiffness with the bar's natural frequency. For axial vibration, the fundamental frequency of a fixed-free bar is

$$\omega = \frac{\pi}{x_0} \sqrt{\frac{E'}{\rho}} \qquad (A.4)$$

where ρ is the composite sensor density. This density can be estimated by using the rule of mixture.

For a one degree of freedom system the relationship

$$\omega = \sqrt{\frac{K}{m}} \qquad (A.5)$$

can be used to estimate the equivalent mass of the paint sensor. Solving equations (A.3) through (A.5) for the equivalent mass yields

$$m = \frac{4\,x_0}{\pi^2} \rho\,A \qquad (A.6)$$

Finally, the damping term is derived using the damping the complex modulus $E = E' + jE''$ of the composite sensor and the relationship (Inman, 2007)

$$\omega = \eta \frac{K}{b} \qquad (A.7)$$

with the loss factor

$$\eta = \frac{E''}{E'} \qquad (A.8)$$

where E'' denotes the loss modulus.

The equivalent damping coefficient is obtained by solving equations (A.3), (A.4) and (A.7).

$$b = \frac{2}{\pi} \eta \, A \, \sqrt{\rho \, E'} \qquad\qquad (A.9)$$

It should be mentioned that equation (A.2) is also applicable to determine the loss modulus (E'', E_p'' instead of E' and E_p', respectively).

Chapter 3: Manufacturing the Smart Paint Sensor

3.1 Overview

This chapter presents details of the procedures adopted to manufacture samples of the smart paint sensors which are made of polyurethane polymer mixed with nano-particles of carbon black (CB).

3.2 Manufacturing of the Smart Paint

Manufacturing of Carbon Black Polyurethane (CBP) is carried out by mixing the carbon black (CB) particles into a mixture of polyurethane polymer. The liquid polyurethane polymer, used in this study, is manufactured by Forsch Polymer Corporation. The polyurethane polymer consists of two components, A: Isocyanate and B: Polyol, as shown in Figure 3.1. The two components are mixed such that the mixture has 40 parts of A and 100 parts of B. When these two components are mixed by a stirring-mixing process, a chemical reaction occurs which forms the polyurethane polymer. The carbon black (CB) particles must be blended completely with the polyurethane components before the chemical reaction is completed, which usually takes about 15-25 minutes at room temperature as listed in Table 3.1.

Figure 3.1: Liquid Polyurethane mixtures (A and B) from Forsch Polymer
Corporation (Englewood, Co)

Table 3.1: Main properties of Polyurethane 60A
[Forsch Polymer Corporation (Englewood, Co)]

NO.	PROPERTY	VALUE
1	Working Time @77 Deg. F	15-25min
2	80% -90% Physical Properties @77 Deg F	2 days

3	100% Physical Properties @77 Deg F
	  ▪ Hardness, Shore A 58-62
	  ▪ Density, 1,080 kg/m^3
	  ▪ Tensile Strength, Ultimate, psi 1250
	  ▪ Elongation, % 475
	  ▪ Tear Strength PLI 165
	  ▪ Linear Shrinkage
	    D-2566(1.125" Deep) .0005 in/in
		7 Days

3.2.1. Preparation of the constituents

Depending on the desired weight percentage of the CB, the correct weights of

the CB and the polyurethane components A and B can be calculated. For example, to

manufacture a sample of CBP that weighs 30g with 15% of CB weight, the weight

calculations of the different ingredients is as shown in the Table 3.2.

Table 3.2: Ingredients for a 30g CBP with 15 weight % CB

CB WEIGHT	$30 \times 15/100$	**4.5G**
Part A	$(30-4.5) \times 40/140$	**7.3g**
Part B	$(30-4.5) \times 100/140$	**18.2g**
Total Weight		**30g**

The CB used, in this study, is acetylene black, from Alfa Aesar Company (Ward Hill, MA), with an average particle size 42 *nm*, a surface area 75 *m²/g*, a density 1.75 *g/cm³* and a bulk density 94.5–102.5 *kg/m³*.

After the weight calculations are done, each ingredient is weighted using a digital weighing scale as shown in Figure 3.2.
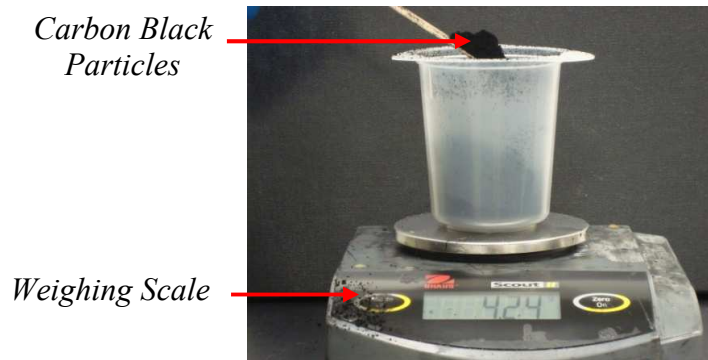
Figure 3.2: Carbon black nano-particles is weighted on a digital weighing scale

3.2.2 Preparing the mold

The CBP is manufactured in the form of thin films which will be suitable for the use as sensors that can be easily bonded to the surfaces of flexible structures. The films are manufactured to by pouring the CBP mixture into mold which is pretreated with a mold release. The Resin Craft's PolyVinylAcetate (PVA) is used in this study as the mold release agent. It is applied to the walls and the sides of the mold in order to facilitate the extraction of the CBP thin film from the mold once it is cured and also to protect it from any damages that may occur during the process of disassembling the mold. The mold release must be applied using a smooth brush to minimize in development of any air bubbles on the surface of the cavity as shown in Figure 3.3.

Mold Release Agent (PVA)
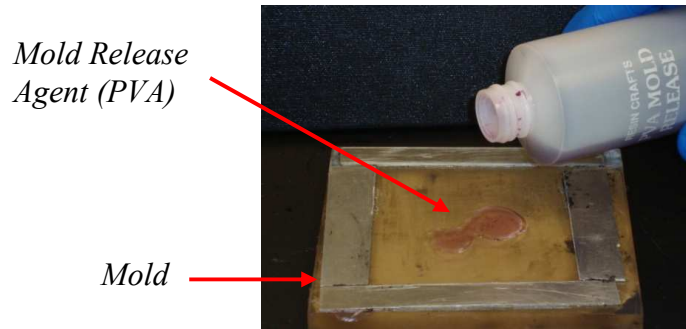
Mold

Figure 3.3: Application of mold release liquid

3.2.3 Mixing process

The ingredients with the correct weights are poured into a glass container and stirred with a wooden tongue presser. At the beginning of the mixing process, the rate of the stirring must be slow in order to prevent the CB nano-particles from dispersing away from the container. As the stirring continues for about a minute, the mixture becomes a rough-textured compound as the CB nano-particles blend into the ingredient of the polyurethane. Then, using a heavy-duty rotary mixer, the resulting mixture is continually mixed until the texture of the compound become smooth and silky as shown in Figures 3.4 through 3.6.

Figure 3.4: Beginning stage of mixing

Figure 3.5: Mixing using a heavy-duty mixer

Figure 3.6: Silky texture indicates complete mixing

After the mixing is completed, the silky compound is placed under a vacuum chamber in order to remove any air bubbles or pockets that may have been entrapped or formed in the compound during the mixing process. The air removal process inside the vacuum chamber is repeated twice to ensure complete removal of the air bubbles as their presence would affect the quality and integrity of the manufactured thin films. A photograph of the set-up is shown in Figure 3.7.
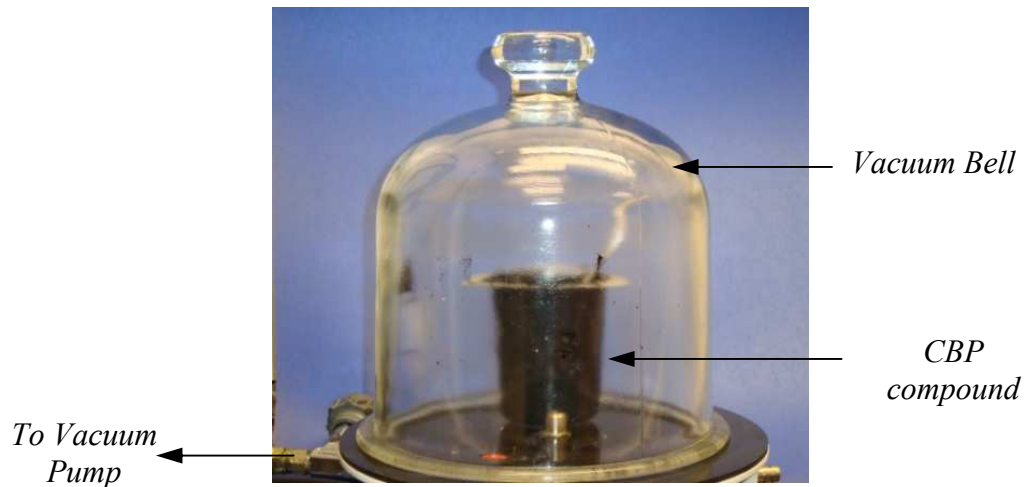
Figure 3.7: Removes air bubbles using a vacuum chamber
(American 3B Scientific, http://www.a3bs.com/vacuum/vacuum-bell-jar-u21851,p_83_110_123_0_1470.html)

3.2.4 Molding process

After the mixing and vacuum processes are completed, the mixed compound is poured into the pretreated mold which has the desired dimensions of the thin film as shown in Figures 3.8 and 3.9. Then, the top cover of the mold is placed slowly in order to avoid air entrapment. In often times, vacuuming is done during this sandwiching process in order to remove any air bubbles entrapped inside mold. After the CBP compound is sandwiched completely inside the mold as shown in the Figure 3.10, the mold is pressed using a hydraulic press as can be seen from Figure 3.11. The CBP takes about 24 hours until it cures completely. The thin CBP film can then be removed from the mold as shown in Figure 3.12. Then it can be rinsed with water in order to remove the water-based mold release as indicated in Figure 3.13.
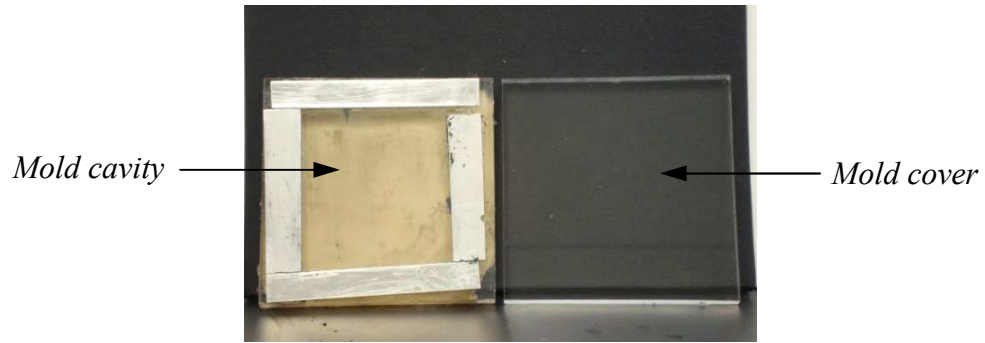
Figure 3.8: A 6 × 6 × 1/32 inches mold

Figure 3.9: Pouring the CBP into mold cavity
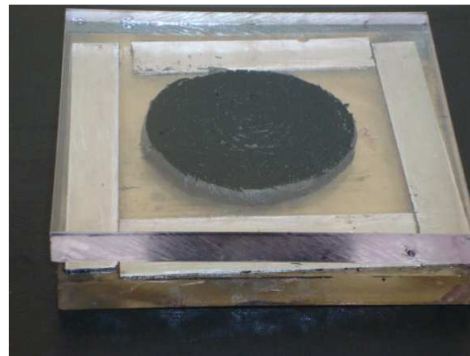
Figure 3.10: Sandwiching the CBP inside the mold
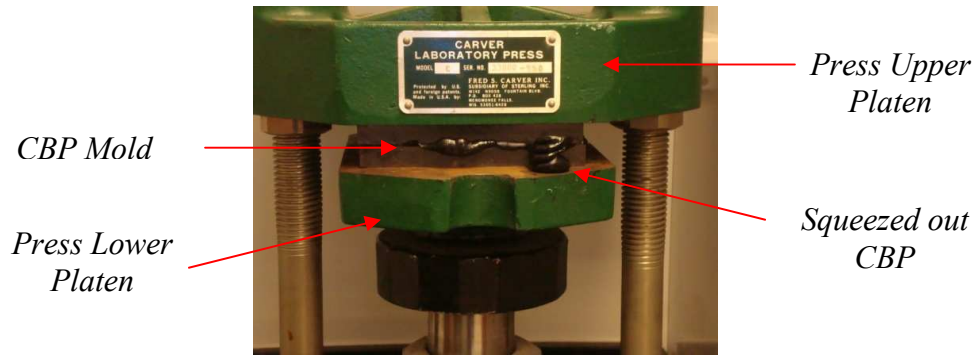
Figure 3.11: Pressing the mold using a hydraulic press
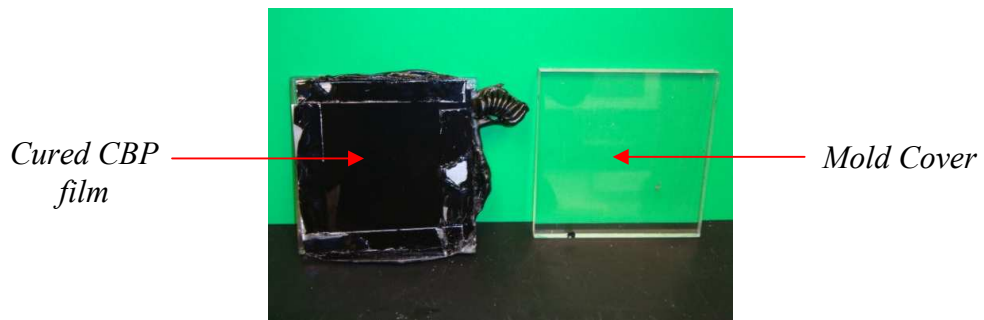
Figure 3.12: Cured CBP film after 24 hours
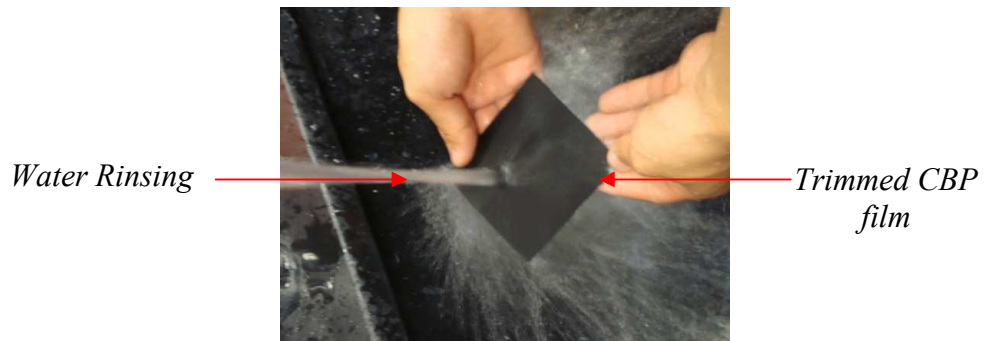
Figure 3.13: Rinsing water-based mold release with water

3.2.5 Applying electrodes

After the CBP film is dried from rinsing the mold release, a conductive epoxy, shown in Figure 3.14, is applied over both the top and bottom sides of the film in order to form the surfaces of conducting electrodes. The conductive epoxy obtained

from Al Technology, Inc. consists of two components which are mixed such that their mixing volume ratio is 1 to 1. After the conductive epoxy is applied very thinly as shown in Figure 3.15, the CBP film is placed in an oven at 30 ° C for 6 hours to cure and dry.

Figure 3.14: Components of the conductive epoxy (Al Technology Inc.)

(a) application of conducting epoxy   (b) – CBP film with electrodes

Figure 3.15: Electrodes of the CBP film

3.2.6 Preparation of smart paint sensor

The electroded CBP films can now be cut to the proper dimensions according to the sensor size needed for any particular application. Conducting copper strips are bonded to the electrodes, as shown in Figure 3.16, to which wires are soldered as to connect the sensor to a bridge and a computer to monitor the changes in the sensor resistance and capacitance.

Circular Sensor　　　　*Rectangular Sensor*

Conducting copper strip

Sensor with conducting copper strips and wires　　　　*Sensor with conducting copper strips*
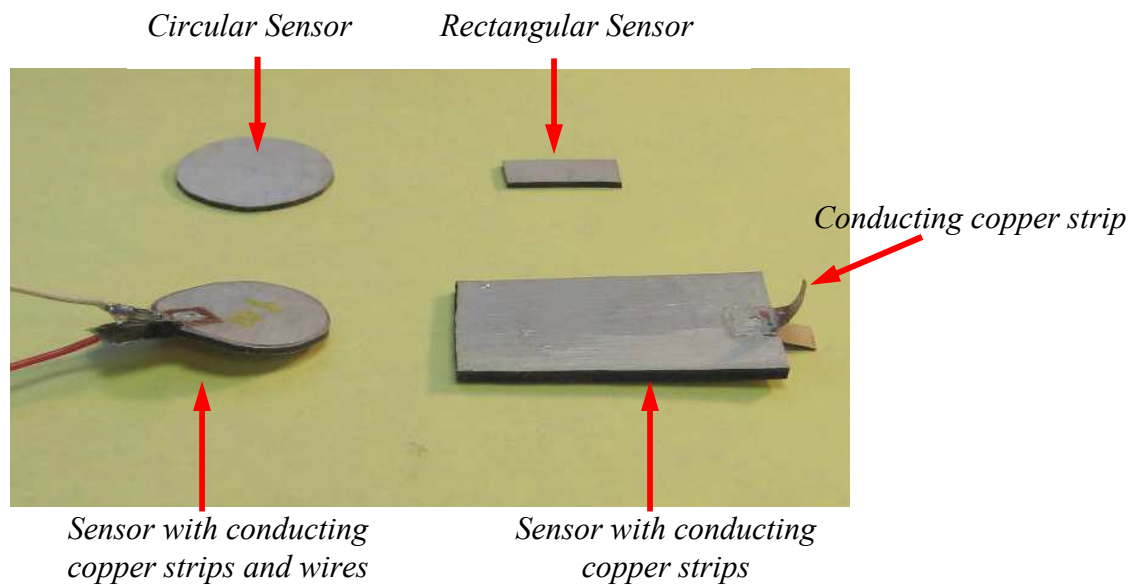
Figure 3.16: Configurations of the CBP smart paint sensor

3.3 Summary

This chapter has presented the details of procedures adopted for manufacturing the smart paint sensor including: selection of the ingredients, mixing, air bubble removal, mold preparation, molding, pressing, releasing, rinsing, depositing electrodes, oven curing, and sensor preparation.

Chapter 4: Experimental Characteristics of the Smart Paint Sensor

4.1 Overview

This chapter presents the experimental characteristics of the smart paint sensor. The effect of the applied load on the piezoresistance properties of the sensor is measured, the viscoelastic characteristics of the sensor material are measured as function of the operating temperature and frequency, and the response of the sensor both in the time and frequency domain are determined. Comparisons are also established between the response of the smart paint sensor and conventional strain gage sensors in order to quantify the potential, merits, and limitations of the sensor.

4.2 Piezoresistance Characteristics of Sensor

4.2.1 Materials and measuring instruments

The piezoresistance characteristics of the smart paint sensor are measured experimentally under no load to determine the effect of carbon black concentration on the resistivity in an attempt to quantify the percolation threshold. Also, the piezoresistance is measured for a sensor sample that has carbon black concentration exceeding the percolation threshold when it is subjected to static tensile and compressive loads.
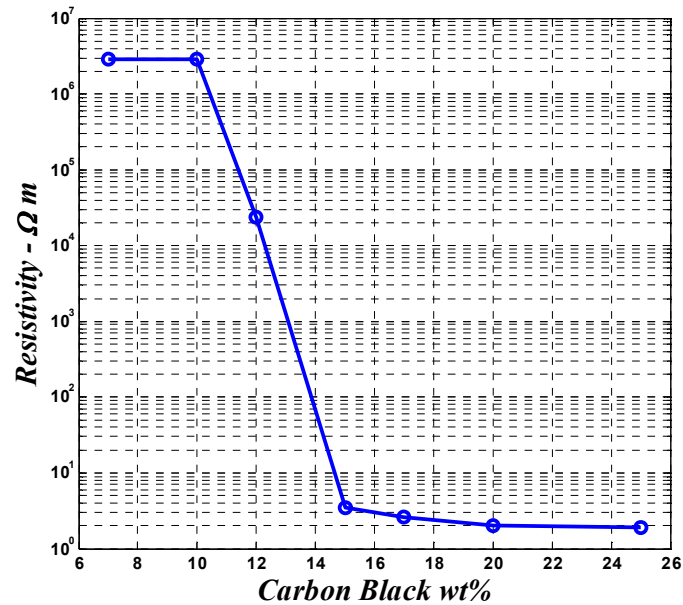
4.2.2 Percolation threshold

Figure 4.1 shows the effect of carbon black concentration on the resistivity of the smart paint sensor. Several samples are manufactured with CB concentrations varying from 7 to 25% by weight. The resistance of these samples is measured by a multimeter under no load condition. The resistivity ρ_s of each sample is determined from:

$$\rho_s = RA/L_s \qquad (4.1)$$

where R = resistance of sensor, A = cross sectional area of sensor, and L_s = sensor length. Table 4.1 and Figure 4.1 summarize the effect of the concentration of the carbon black on the resistivity of the smart paint sensor. The figure indicates that the zone between CB concentration of 10-20% is the percolation zone where the maximum drop of the resistivity occurs. Note that the resistivity at 10% concentration is six orders of magnitude that at the end of the percolation zone.

Table 4.1: effect of the concentration of the carbon black on the resistivity of the smart paint sensor

CB CONCENTRATION (*WT%*)	7	10	12	15	17	20	25
Resistivity (Ωm)	2.91E6	2.90E6	2.4E4	3.42	2.60	2.00	1.90

Figure 4.1: Effect of carbon black concentration on the resistivity of the smart paint sensor

In the remaining of this study, all the investigations are carried out on smart paint sensor with CB concentration of 20%. For this concentration, the effect of the capacitance becomes negligible and the sensor acts primarily as a resistive strain gage sensor.

4.2.3 Effect of load on piezoresistance of paint sensor

Figure 4.2 shows the experimental set-up used in measuring the piezoresistance-load characteristics.

A sample of the smart paint which has 20% carbon black concentration, by weight, and is 2.75" long, 0.3765" wide, and 0.04" thick is placed between the jaws of the test set-up. The sample is subjected to a static load applied by the power screw arrangement and the resulting load is measured by the load cell (LC201-25, Omega Engineering, Stamford, CT). The specifications of the load cell are listed in Table

4.2. The output of the load cell is read using a strain meter/controller/amplifier unit (DP25B-SA, Omega Engineering, Stamford, CT). The specifications of the strain meter/controller/amplifier are listed in Table 4.3.
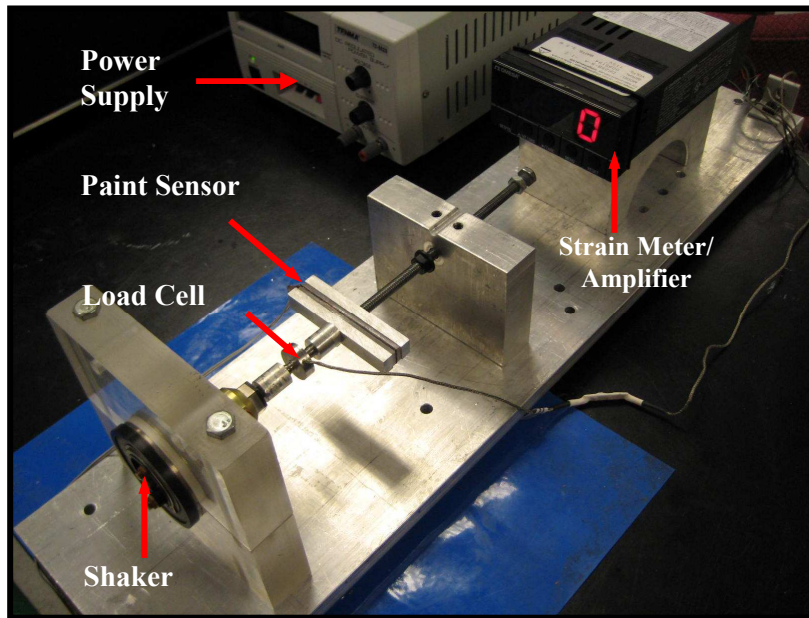
Figure 4.2: Set-up for measuring the piezoresistance characteristics of the smart paint sensor

Table 4.2: Specifications of the load cell
(LC 201-25, Omega Engineering, Stamford, CT)

PROPERTY	VALUE
Excitation	10 Vdc, 15 Vdc max
Output	2 mV/V nominal
Accuracy	±1.0% FSO linearity
Zero Balance	±2% FSO
Operating Temp Range	-54 to 121°C (-65 to 250°F)
Photograph and Dimensions	

Table 4.3: Specifications of the strain meter/amplifier
(DP 25B-SA, Omega Engineering, Stamford, CT)

PROPERTY	VALUE
Display	4-digit, 9-segment, 21 mm (0.83") high [...]en LED (programmable)
Analog-to-Digital Technique:	Dual slope
Internal Resolution	15-bit
Read Rate	3/s
Power	115 Vac or 230 Vac ±10%, 10 to 32 Vdc, 26 to 56 Vdc; 8 W max (DP25B-TC or -RTD), 11 W max (DP25B-E or -S); 240 Vrms overvoltage protection
Isolation:	Dielectric strength to 2500 V transient per 3 mm spacing based on EN61010 for 260 Vrms or Vdc
Operating Temperature	0 to 50°C (32 to 122°F)
Relative Humidity	90% @ 40°C (104°F), non-condensing
Dimensions	48 H x 96 W x 152 mm D
Photograph	

Figure 4.3a shows the effect of applied stress on the piezoresistivity characteristics of the smart paint sensor. The figure displays the results obtained from two sets of experiments. It is clear that the relationship between stress and resistivity is nonlinear and the rate of change is different when the stress is tensile or compressive. The experimental result confirms the nonlinear behavior exhibited by equations 1.17 and 2.19.

Figure 4.3b displays the obtained piezoresistivity results in a non-dimensional manner in the $\Delta R / R_0 - Stress / E$ plane which is also the $\Delta R / R_0 - Strain\ (\varepsilon)$ plane.
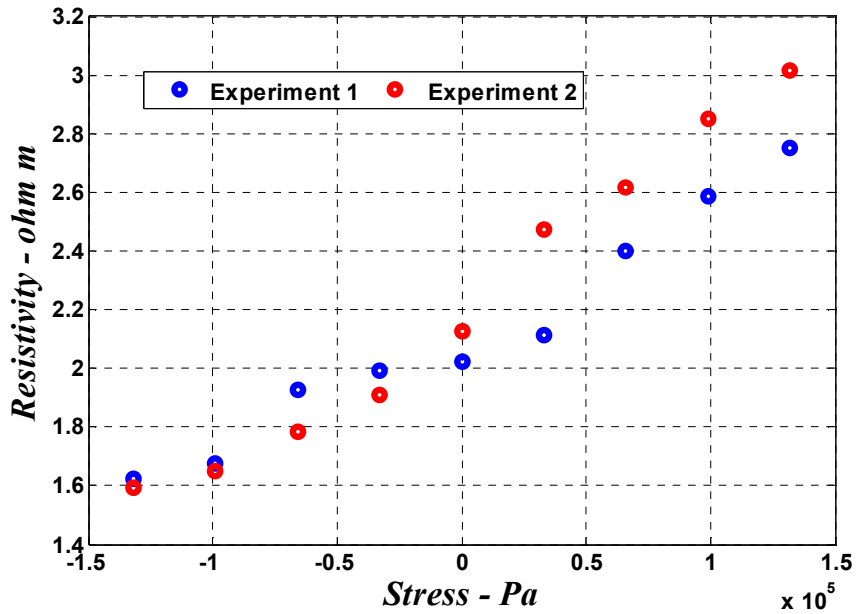
(*a*) – stress – resistivity characteristics
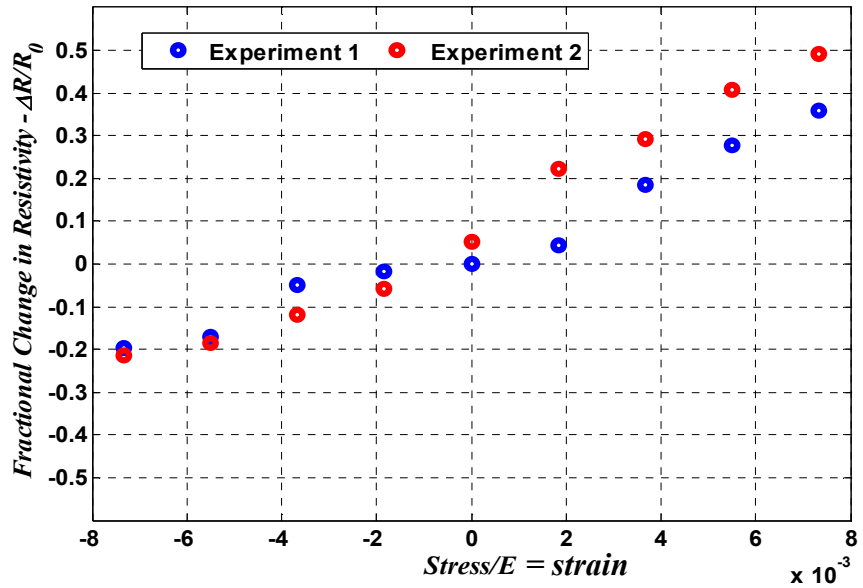
(*b*) – stress – fractional changes in resistivity characteristics

Figure 4.3: Effect of stress on the piezoresistivity characteristics of the smart paint sensor

Note that equation 1.17 can be rewritten as:

$$-\Delta R / R_0 = 1 - \left(1 - \frac{\sigma}{E}\right) e^{-\gamma D\left[\left(\frac{\pi}{6}\right)^{\frac{1}{3}} \theta^{-\frac{1}{3}} - 1\right]\frac{\sigma}{E}} \tag{4.2}$$

or

$$\frac{\left[1 + \Delta R / R_0\right]}{\left(1 - \frac{\sigma}{E}\right)} = e^{\bar{\gamma}\frac{\sigma}{E}} \tag{4.3}$$

where

$$\bar{\gamma} = \gamma D\left[\left(\frac{\pi}{6}\right)^{\frac{1}{3}} \theta^{-\frac{1}{3}} - 1\right] \tag{4.4}$$

From Figure 4.3b, as $\sigma / E < 0.01$, then equation 4.3 can be simplified to:

$$\left[1 + \Delta R / R_0\right] \cong e^{\bar{\gamma}\frac{\sigma}{E}} \tag{4.5}$$

Taking the natural logarithm of both sides of equation 4.4, gives:

$$ln\left[1 + \Delta R / R_0\right] \cong \bar{\gamma}\frac{\sigma}{E} = \bar{\gamma}\,\varepsilon \tag{4.6}$$

Equation 4.6 indicates that the relationship between $ln\left[1 + \Delta R / R_0\right]$ and the σ / E (or ε) is a straight line with a slope of $\bar{\gamma}$. This relationship is the basis for the operation of the smart paint sensor. Further, the relationship is drawn in Figure 4.4. It is clear that $\bar{\gamma} = 50$. Note that using equation 4.4, the theoretical value of $\bar{\gamma} = 54.97$ indicating that the theoretical model over predicts $\bar{\gamma}$ with an error of 9.97%.
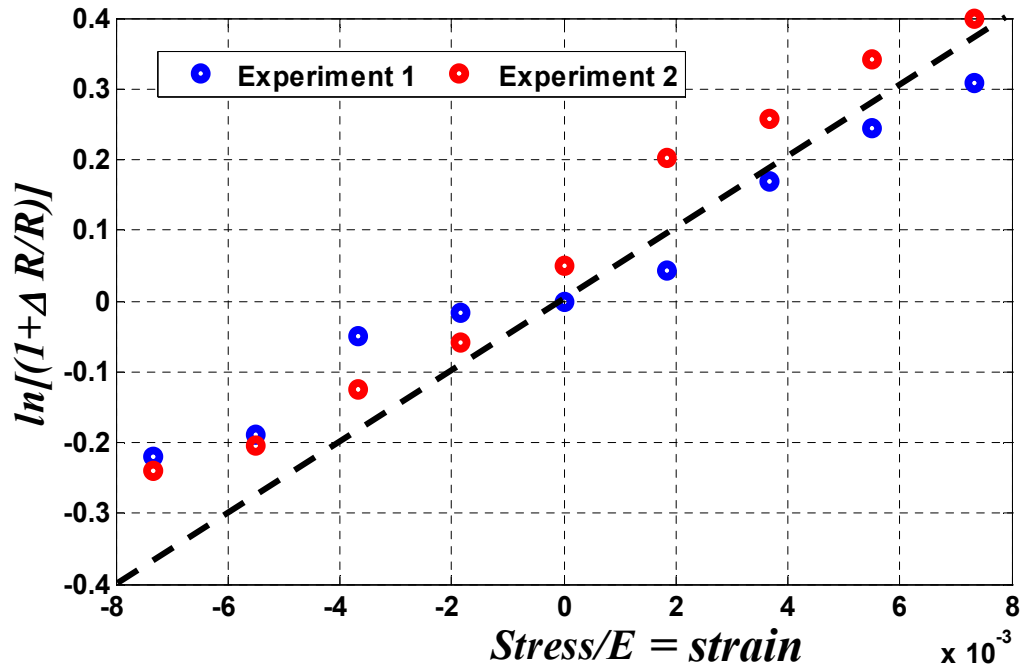
Figure 4.4: Fitting the piezoresistivity characteristics to mathematical model

Note that equation 4.6 can be approximated to:

$$\varepsilon = \frac{1}{\overline{\gamma}} ln \ \left[1 + \Delta R / R_0 \right] \cong \frac{1}{\overline{\gamma}} \Delta R / R_0 \qquad (4.7)$$

This indicates that the relationship between the strain ε and the fractional change in the resistance $\left[\Delta R / R_0 \right]$ is a straight line with a slope of $1/\overline{\gamma}$. This relationship, as shown in Figure 4.5a, can accurately approximate the exact logarithmic relationship if the fractional change in the resistance $\left[\Delta R / R_0 \right]$ lies within the following range:

$$-0.2 < \left[\Delta R / R_0 \right] < 0.2 \qquad (4.8)$$

This results in a maximum error of 10% as shown in Figure 4.5b.
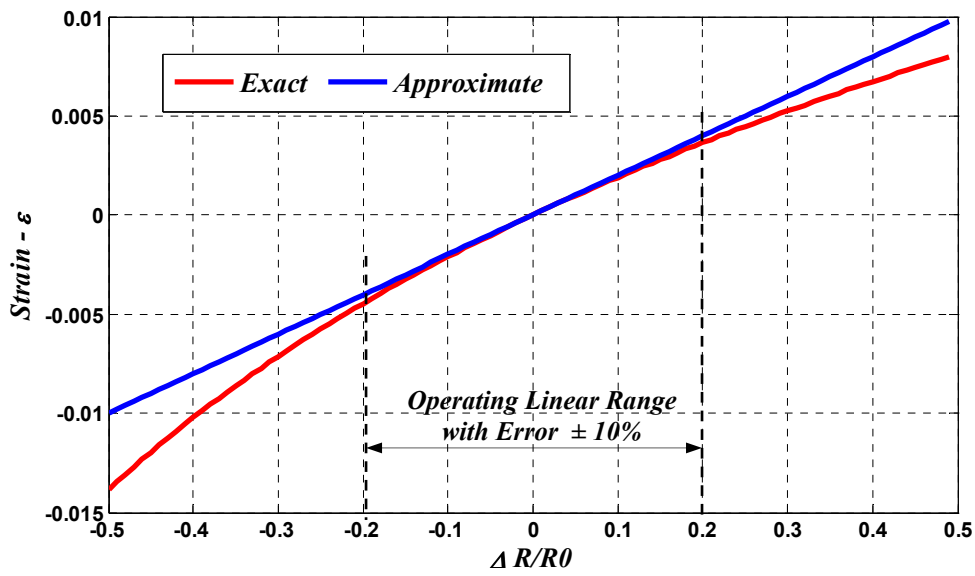
(a) – comparison between exact and approximate models
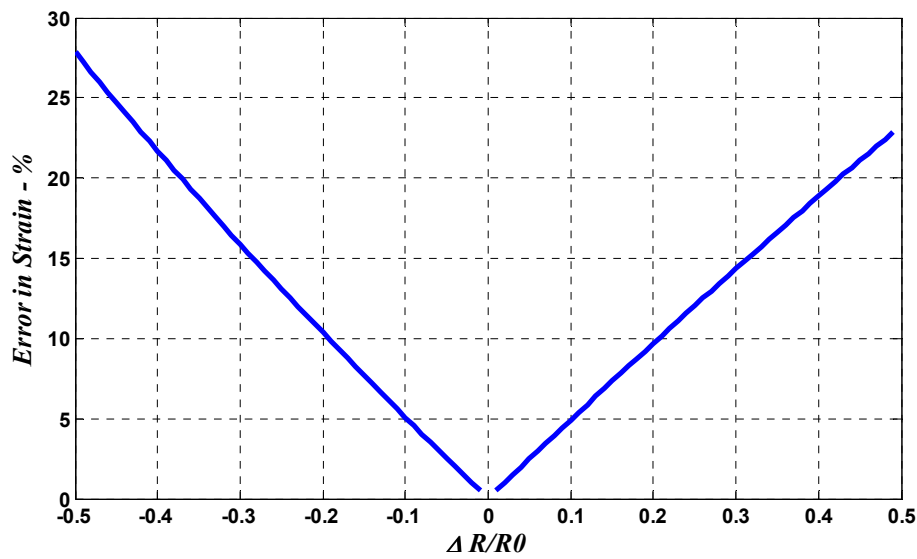
(b) – error between exact and approximate models

Figure 4.5: Comparison between exact and approximate piezoresistivity models of the smart paint sensor

4.3 Viscoelastic Properties of the Smart Paint Sensor

The viscoelastic properties of the smart paint sensors are determined using the Dynamic, Mechanical, and Thermal Analyzer (DMTA) of Polymer Laboratories for temperatures between 25 and 85°C.

Figure (4.6) shows the DMTA system, main components, and different types of heads.

(a) – The DMTA system
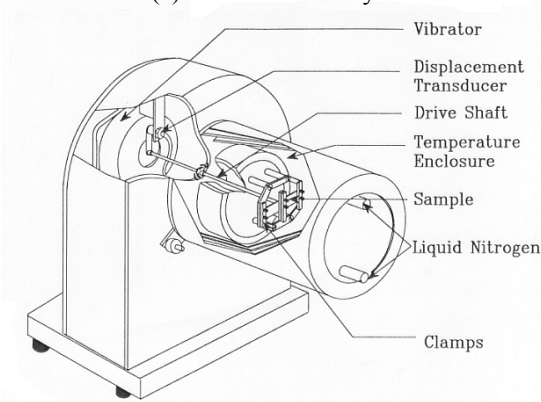
(b) – Main components of the DMTA
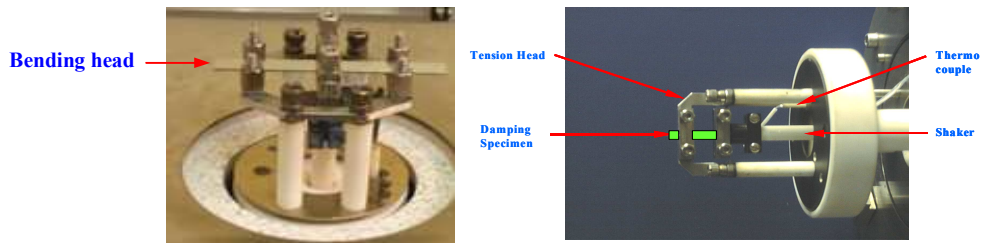
(c) - Different types of DMTA heads

Figure 4.6: The Dynamic, Mechanical, and Thermal Analyzer (DMTA)

Figures 4.7a and 4.7b show respectively the storage modulus and the loss factor of the urethane polymer and the polymer when filled with 20% CB. It can be seen that adding the CB to the polymer increases its storage modulus and decreases its loss factor.
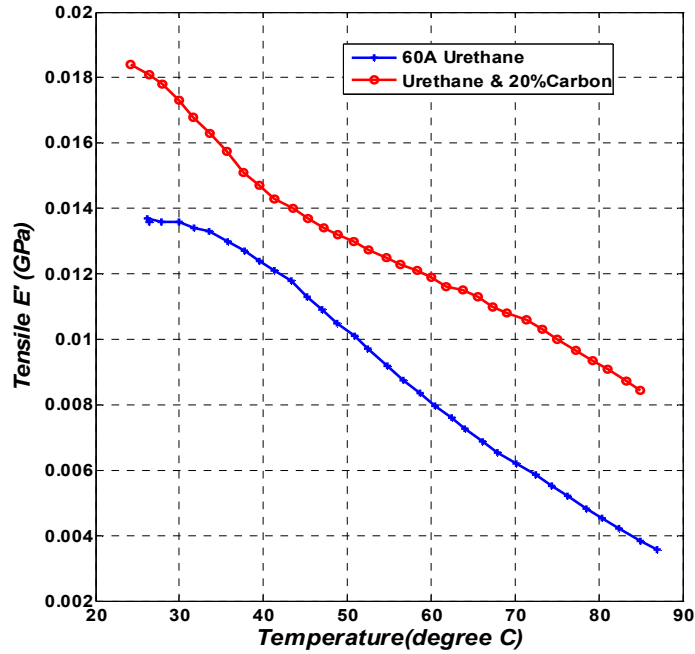
(a) – storage modulus
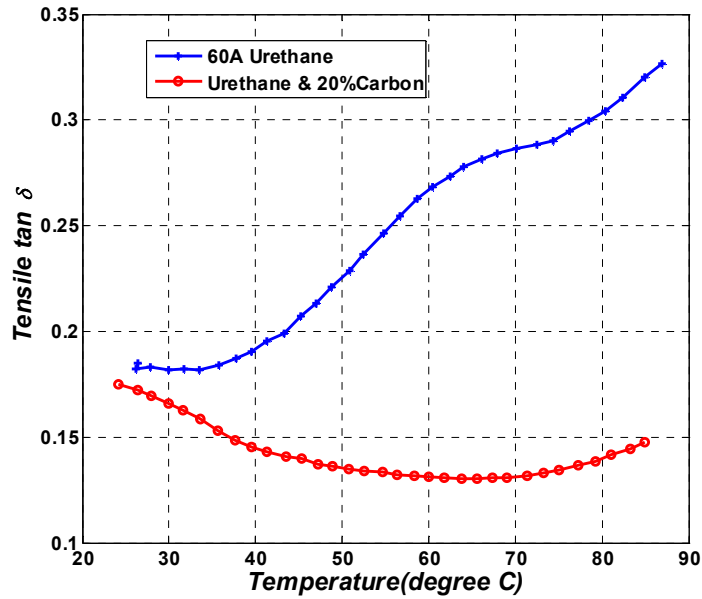
(b) – loss modulus

Figure 4.7: The viscoelastic properties of the smart paint sensor

4.4 Dynamic response of Sensor

4.4.1 The experimental facilities

The dynamic response of the paint sensor is measured using the experimental set-up shown in Figures 4.8 and 4.9. The paint sensor is placed on one side of a cantilevered beam near its root which is excited by an electromagnetic shaker. A strain gage sensor is bonded to the opposite side of the beam in order to serve as means for evaluating the output of the smart paint sensor and establishing its merits and limitations. The paint sensor is powered by a power supply connected to the voltage divider circuit shown in Figures 4.9a and 4.9b whereas the strain gage is connected to a Wheatstone bridge powered by a 5Volt power supply as displayed in Figures 4.10a and 4.10c. The main dimensions of the test beam and sensors are shown in Figure 4.11.
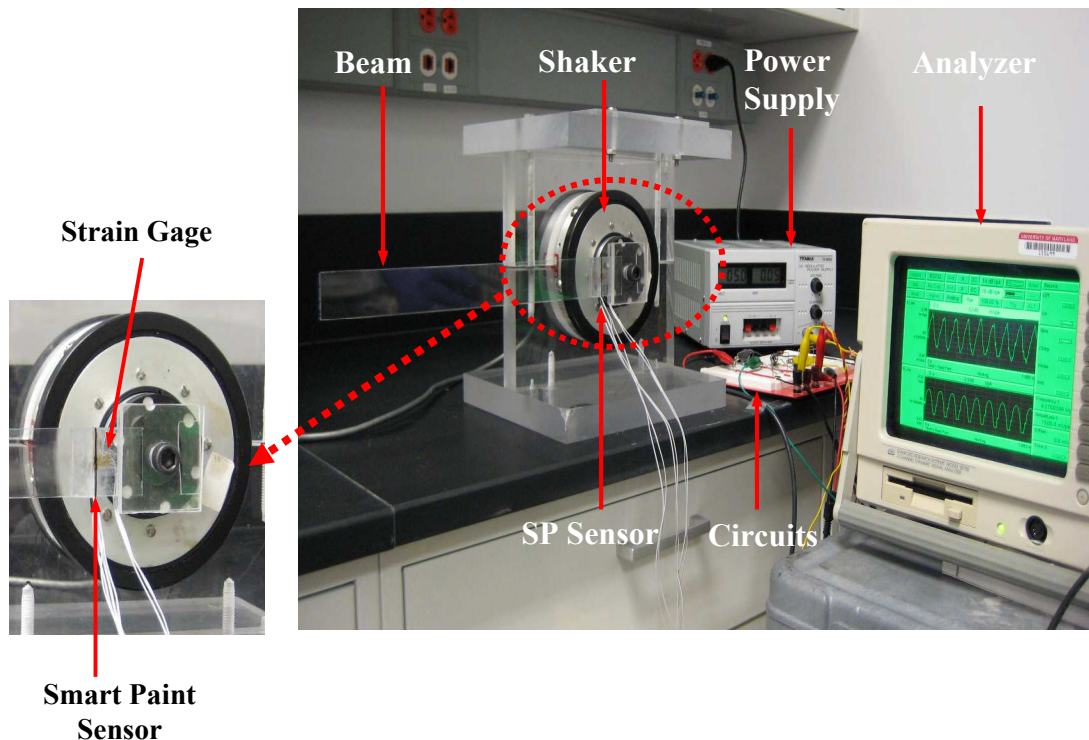
Figure 4.8: Experimental set-up for measuring the dynamic characteristics of the smart paint sensor
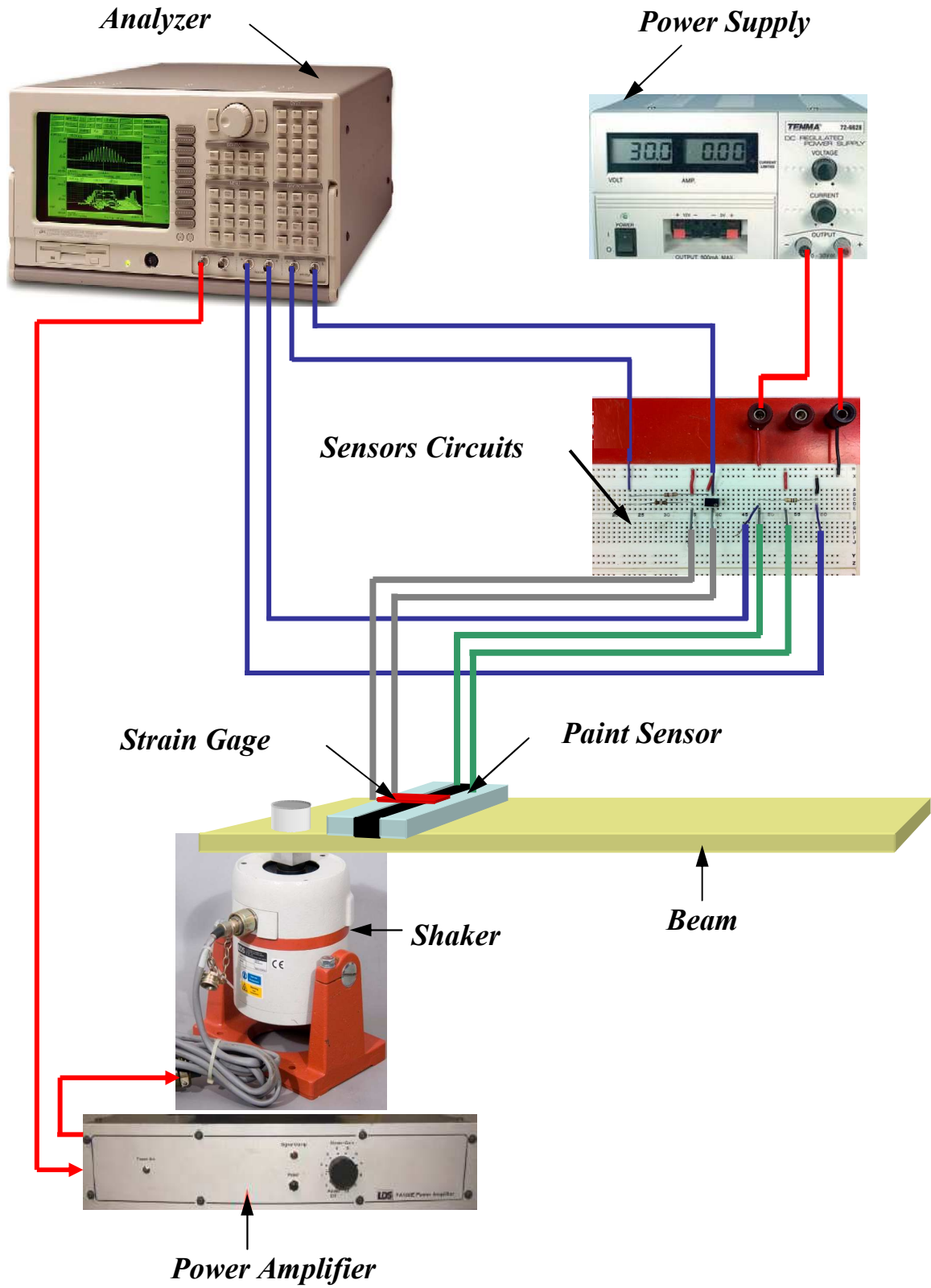
Figure 4.9: Schematic drawing of the experimental set-up for measuring the dynamic characteristics of the smart paint sensor

Strain gage Output
to Analyzer

5 Volts

To Paint
Strain gage

To Paint
Sensor

Paint Sensor Output
to Analyzer
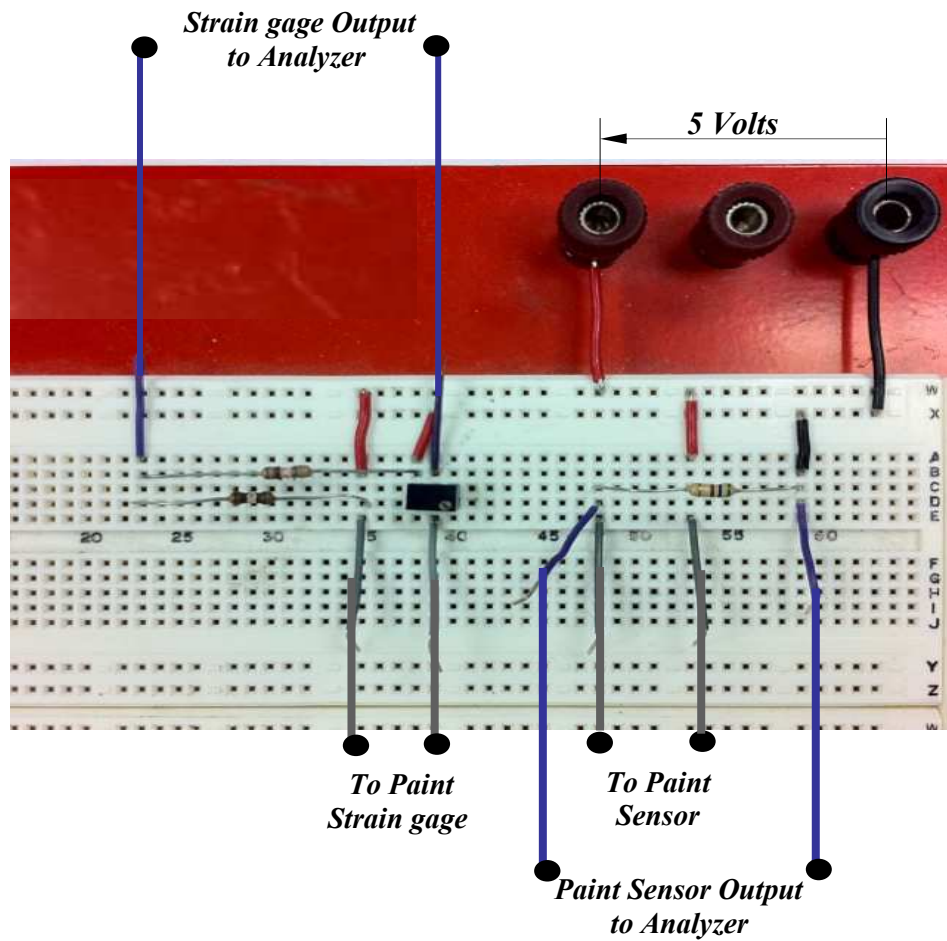
(a) – photographs of sensors circuits

Smart Paint
Sensor

Power
Supply

Resistor
555 Ω

To Analyzer
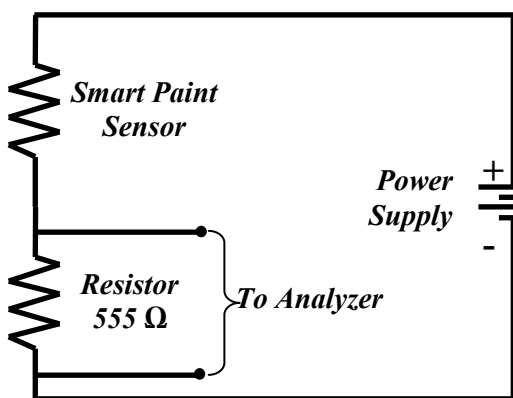
(b) - circuit of paint sensor

Strain
Gauge

Resistor
120 Ω

To Analyzer

Potentiometer

Resistor
120 Ω

Power
Supply
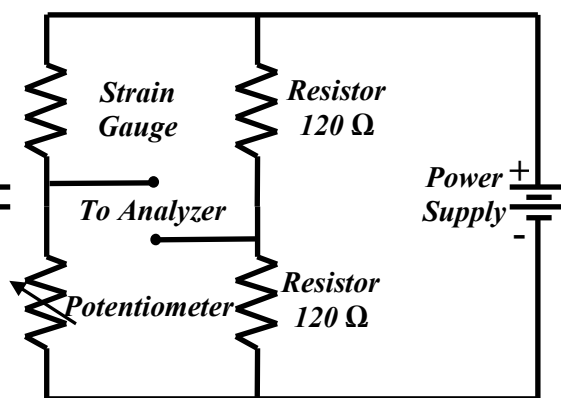
(c) – strain gage bridge

Figure 4.10: Photograph and diagrams of sensors circuits
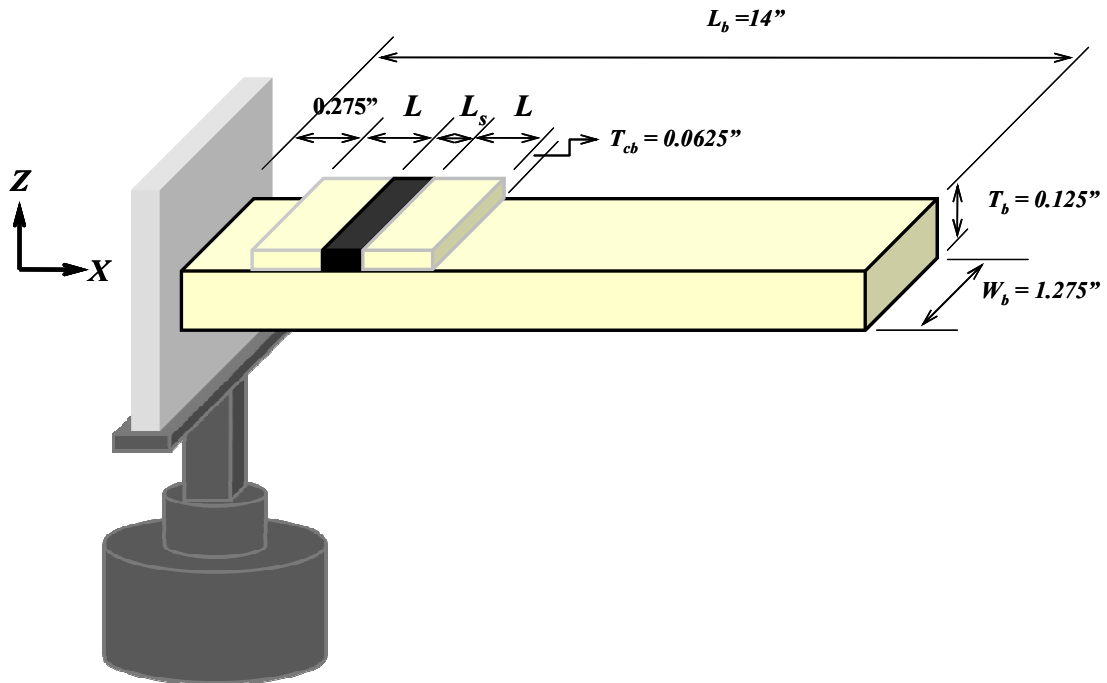
Figure 4.11: Main geometrical parameters of the beam/paint sensor assembly
(L=0.275", Ls=0.040")

The specifications of the electromagnetic shaker (V408, from LDS Test and Measurement LLC, Middleton, WI) are listed in Table 4.4. Table 4.5 lists the specifications of the power amplifier of the shaker (PA100E, from LDS Test and Measurement LLC, Middleton, WI).

Table 4.4: Specifications of electromagnetic shaker
(V408 – LDS Test and Measurement LLC, Middleton, WI)

PROPERTY	VALUE
System sine force paek (naturally cooled)	98 N
System sine force paek (forced cooling)	196N
Shaker max random force rms	89N
Max acceleration sine peak	100g
System velocity sine peak	1.78m/s
System continuous displacement (pk-pk)	17.6mm
Moving element mass	0.2kg
Usable frequency rang	5-9,000Hz

Table 4.5: Specifications of power amplifier of shaker
(PA100E – LDS Test and Measurement LLC, Middleton, WI)

PROPERTY	VALUE
Rated sinusoidal power output matched	147W
Resistive load	2.9Ω
Max. continuous sinusoidal VA output, 0.5pf	147VA
Frequency range at rated power	10Hz-10kHz
Total harmonic distortion at rated output 20Hz-10kHz	Type 0.5%
Max. output voltage	20V rms
Max. no load voltage	32 V rms
Voltage regulations	3%
Output current at rated VA	7A rms
Random output	14A pk
Over-current trip level	10A rms
Input sensitivity for max output (4kHz)	1 V rms
Signal to noise ratio	>75dB
Amplifier efficiency	58%

4.4.2 Time response characteristics

The dynamic characteristics of the smart paint sensor are measured both in the time and frequency domains. Comparisons are also established between the sensor response and that of conventional strain gage sensor in order to determine the merits and limitations of the smart paint sensor.

In this section, the time response characteristics are presented when the beam/sensor system is excited at its first three modes of vibration.

a. Typical Time Response

The response of the smart paint and the strain gage sensors when the beam is excited at first mode of vibration (*i.e.* at 5.369 Hz) are shown in Figure 4.12.
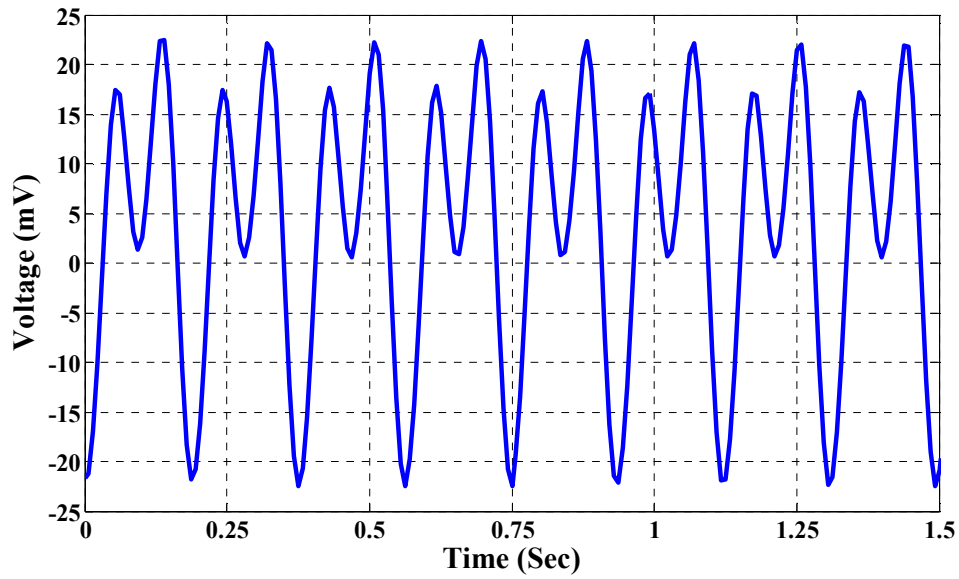
(a) – smart paint sensor
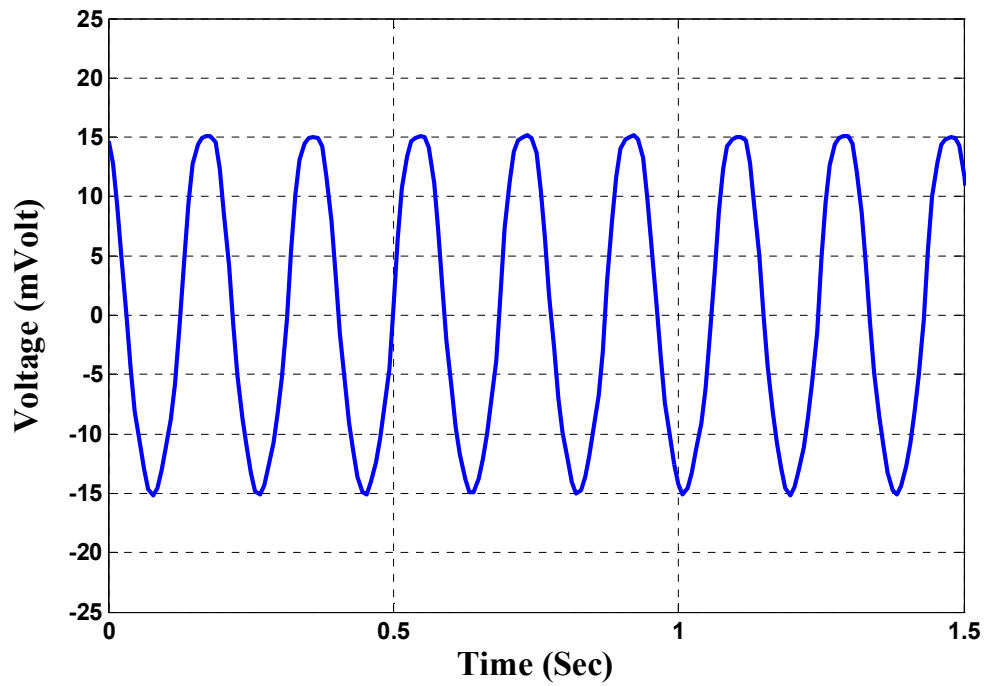
(b) – strain gage

Figure 4.12: Comparison between the time response of the smart paint sensor and the strain gage when the beam/sensor system is sinusoidally excited at first mode of vibration (5.369Hz)

The figure indicates clearly that the output of the smart paint sensor does not replicate the exact strain field as measured by the conventional strain gage sensor. The is an obvious distortion experienced by the smart paint sensor paricularly near the positive peaks of the strain signal. Note that similar wave distortions have been experienced by other investigators as illustrated, for example, in Figure 1.11 (Wang and Chung, 1996) and Figure 1.13 (Hyatt, 2010).

Such distortions are eliminated completely by subjecting the smart paint sensor to a low poling voltage of 10 volt for a period of 5 minutes. The response of the paint sensor improves noticably immediately after the poling. However, it starts replicating the response of the strain gage after almost 120 hours following the poling. Examples of the paint sensor response at different time instants following the poling are presented for the first three modes of vibrations of the beam/sensor assembly.

b. Effect of Poling on Time Response at the first three modes of vibration

Figure 4.13 displays the sequence of improvements that the smart paint sensor undergoes following the initial poling by 10 volts for a period of 5 minutes. The displayed results are recorded before poling, immediately after poling, and then five days after poling on steps of one day. It is clear that the distortion near the peak decreases gradually and after the fifth day, the smart sensor dramatically replicates the response of the strain gage which is shown in Figure 4.13h for the sake of comparison. Note the linearity and sysmmetry of the paint sensor response.
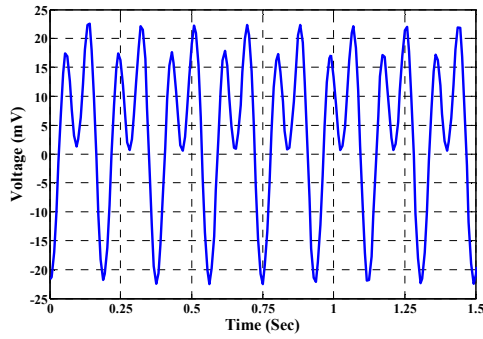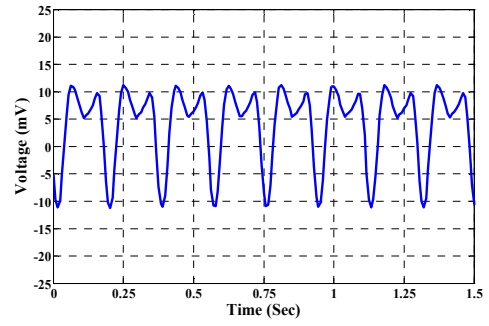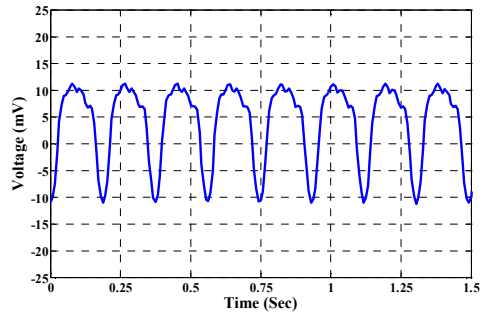
71

(a) – without poling

(b) – immediately after poling

(c) – 24 hours after poling

(d) – 48 hours after poling

(e) – 72 hours after poling

(f) – 96 hours after poling

(g) – 120 hours after poling
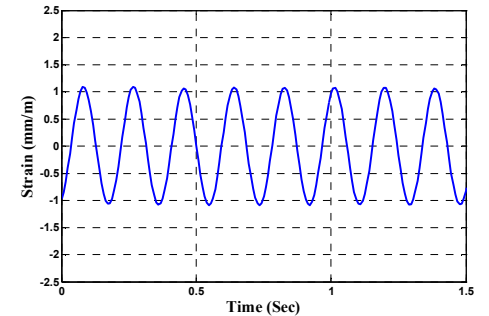
(h) – strain gauge

Figure 4.13: Effect of duration after poling on the time response of the smart paint sensor and the strain gage when the beam/sensor system is sinusoidally excited at the first mode of vibration (5.369Hz)

Similar results are displayed in Figures 4.14 and 4.15 for the effect of the duration after poling on the response of the smart paint sensor and the strain gage when the beam/sensor system is excited at its second and third modes of vibration, *i.e.* at 33.11 Hz and 94.27 Hz respectively.

Note that similar conclusions can be drawn from the results displayed in Figures 4.14 and 4.15 regarding the ability of the paint sensor to replicating the exact state of strain of the beam as recorded by conventional strain gages. Furthermore, the paint sensor maintains the linear and sysmmetrical nature as the strain gage sensor.

(a) – without poling

(b) – immediately after poling
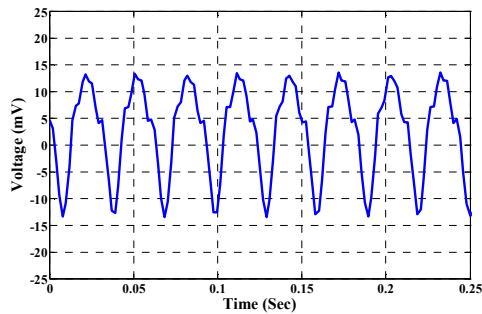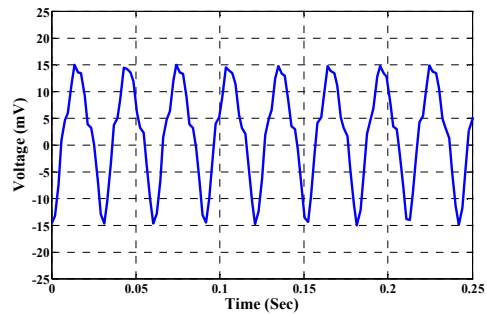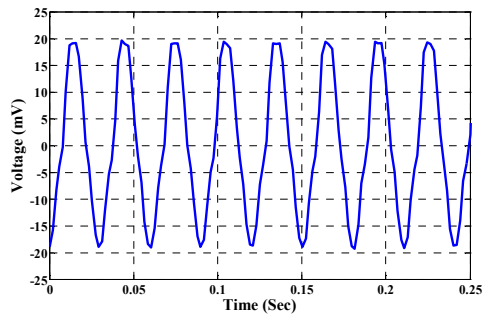
(c) – 24 hours after poling

(d) – 48 hours after poling

(e) – 72 hours after poling
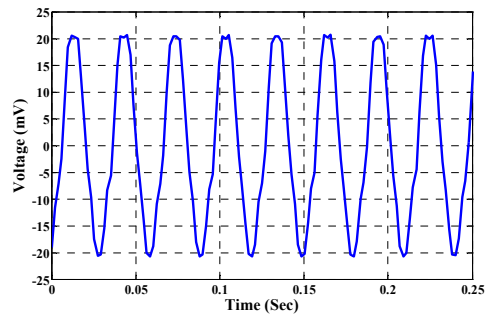
(f) – 96 hours after poling
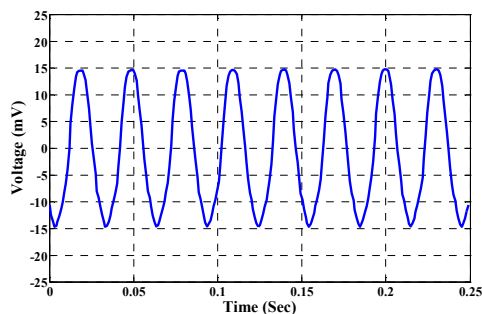
(g) – 120 hours after poling
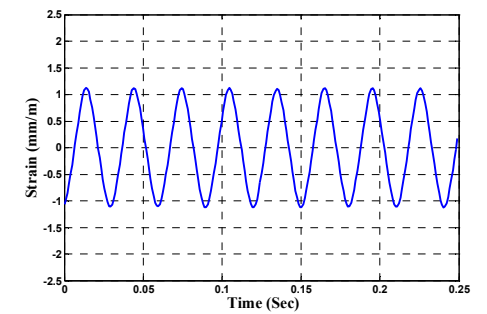
(h) – strain gauge

Figure 4.14: Effect of duration after poling on the time response of the smart paint sensor and the strain gage when the beam/sensor system is sinusoidally excited at the second mode of vibration (33.11Hz)
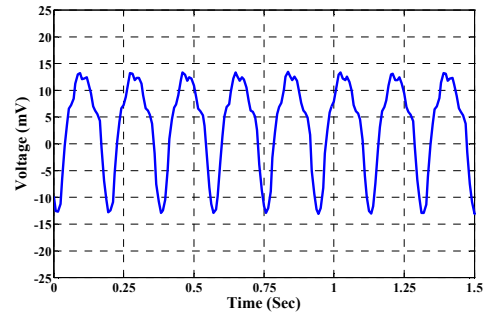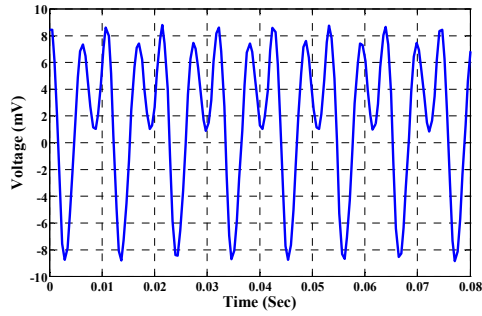
(a) – without poling
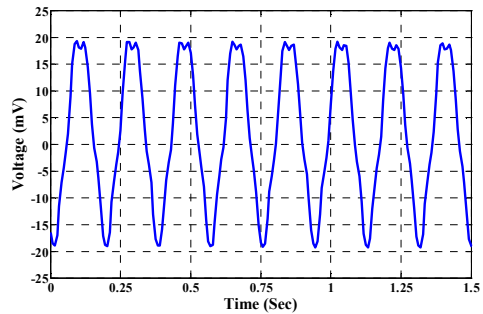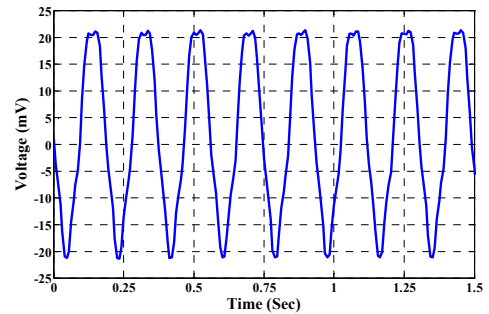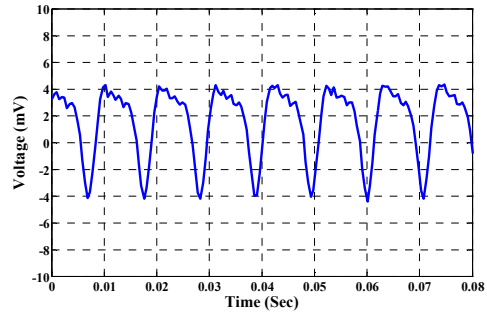
(b) – immediately after poling
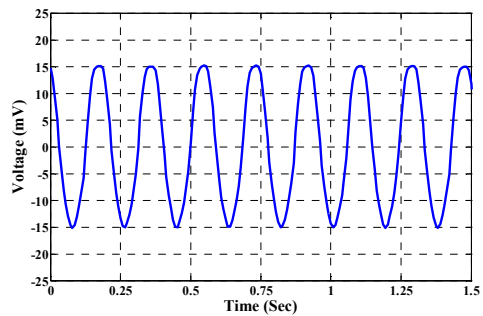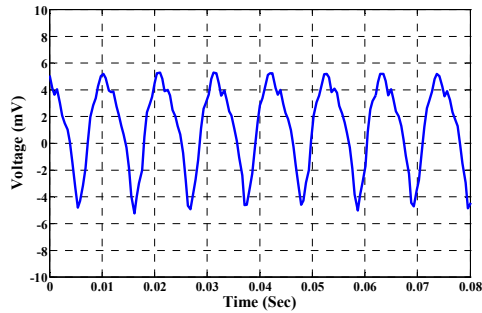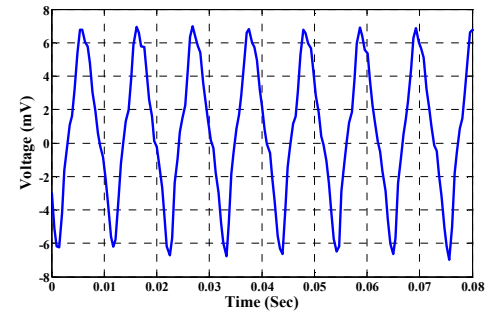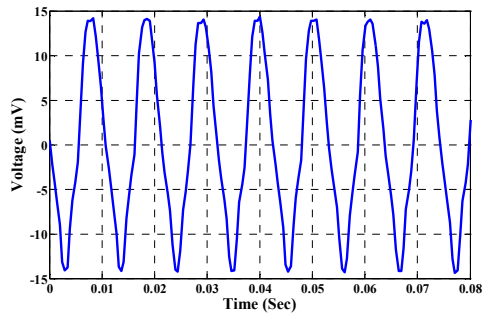
(c) – 24 hours after poling

(d) – 48 hours after poling

(e) – 72 hours after poling
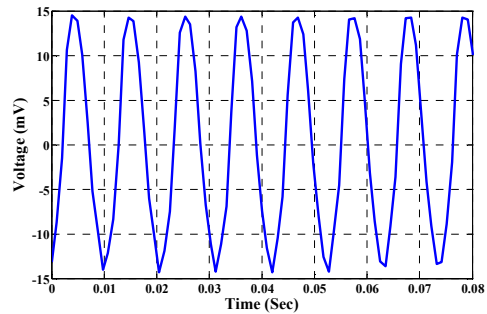
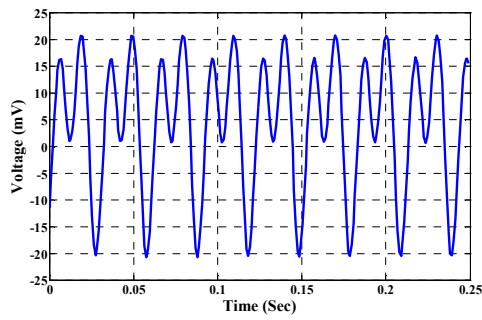(f) – 96 hours after poling

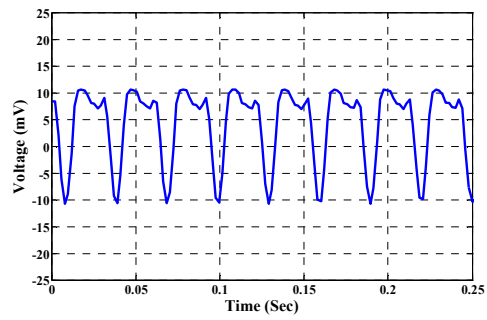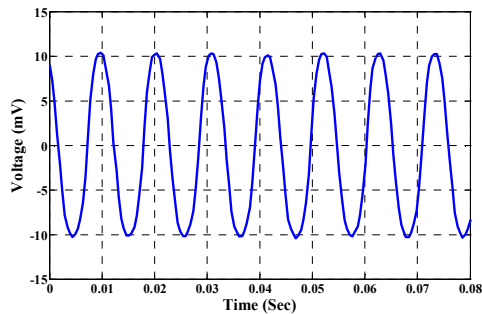(g) – 120 hours after poling
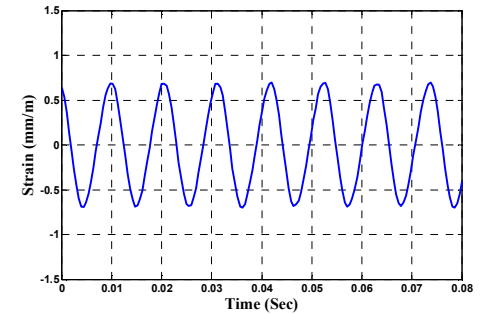
(h) – strain gauge

Figure 4.15: Effect of duration after poling on the time response of the smart paint sensor and the strain gage when the beam/sensor system is sinusoidally excited at the third mode of vibration (94.27Hz)

c. **Comparison between Time Response of Paint Sensor and Strain Gage Characteristics**

In order to establish a quantitative comparison between the paint sensor and the strain gage, the output voltage of the sensor is converted to strains. The conversion is carried out using equation 4.7 which relates the strain ε to the fractional change in the resistance $\Delta R / R_0$ of the paint sensor:

$$\varepsilon \cong \frac{1}{\gamma} \Delta R / R_0 \qquad (4.9)$$

The changes in the resistance $\Delta R / R_0$ can be related to the output voltage V of the paint sensor using the circuit diagram shown in Figure 4.16.
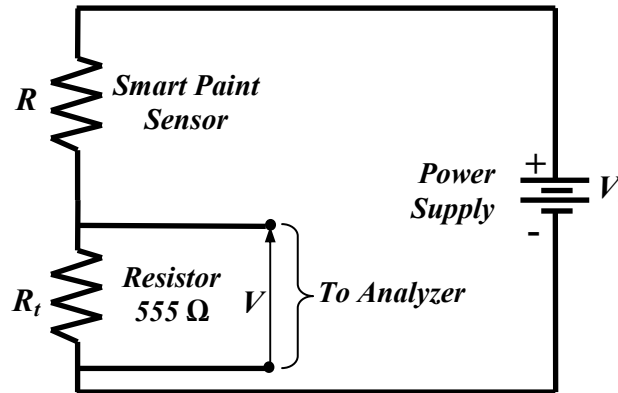
Figure 4.16: Circuit diagram of the paint sensor

Such a relationship, under any loading condition, is given by:

$$V = \frac{R_t}{R + R_t} V_i \qquad (4.10)$$

where R = resistance of the paint sensor, R_t = resistance of voltage divider, and V_i = input power supply voltage as shown in Figure 4.16.

Initially, the paint sensor resistance, at no load conditions, is R_0 then the initial output of the voltage divider circuit is:

$$V_0 = \frac{R_t}{R_0 + R_t} V_i \tag{4.11}$$

Hence, the net change in the sensor output due to the applied load is:

$$
\begin{aligned}
V - V_0 &= \frac{R_t}{R + R_t} V_i - \frac{R_t}{R_0 + R_t} V_i \\
&= \frac{r_t (1 - r)}{(r + r_t)(1 + r_t)_t} V_i
\end{aligned}
\tag{4.12}
$$

where $r = R / R_0$ and $r_t = R_t / R_0$. If r_t is selected such that $r_t \gg r \gg 1$, then equation 4.12 reduces to:

$$V - V_0 = \frac{(1 - r)}{r_t} V_i = -\frac{(\Delta R / R_0)}{r_t} V_i \tag{4.13}$$

Equation (4.13) indicates that the sensor net output voltage $(V - V_0)$ is linearly proportional to the sensor resistance r $(i.e.\ r = R / R_0)$. Note that R_0 for the considered sensor is $31.373\,\Omega$.

Combining equations 4.9 and 4.13 gives:

$$V - V_0 = -\left(\bar{\gamma} \frac{V_i}{r_t} \right) \varepsilon \tag{4.14}$$

Hence, equation 4.14 suggests that the paint sensor output voltage $(V - V_0)$ is linearly proportional to the strain ε.

77

Figures 4.17, 4.18, and 4.19 show comparisons between the strains as predicted by the paint and the strain gage sensors when the beam is excited at the first, second, and third modes of vibration respectively. The figures demonstrate clearly the ability of the paint sensor to replicate the exact state of strain as measured by the strain gage. Note that the displayed results are for a poled paint sensor after 120 hours of curing.
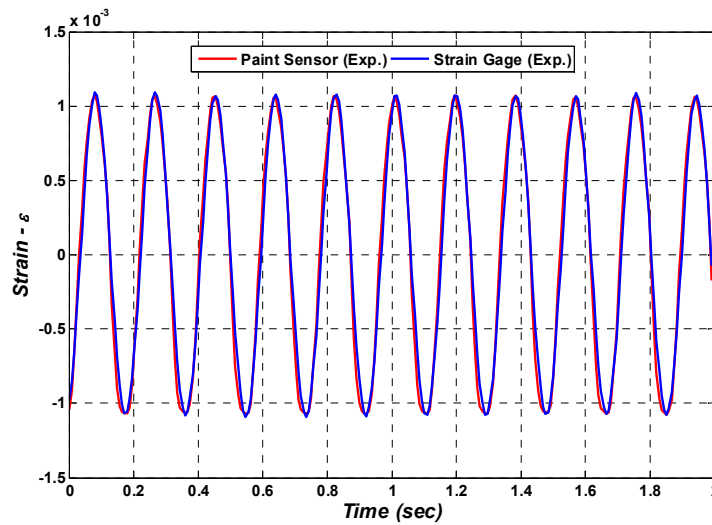
Figure 4.17: Comparison between the strains measured by the paint and the strain gage sensors at the first mode of vibration Frequency (5.36 Hz)
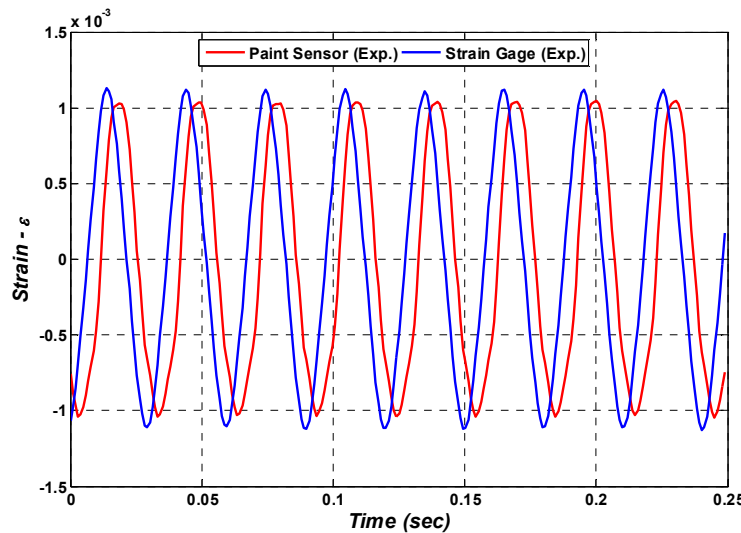
Figure 4.18: Comparison between the strains measured by the paint and the strain gage sensors at the second mode of vibration Frequency (33.11 Hz)
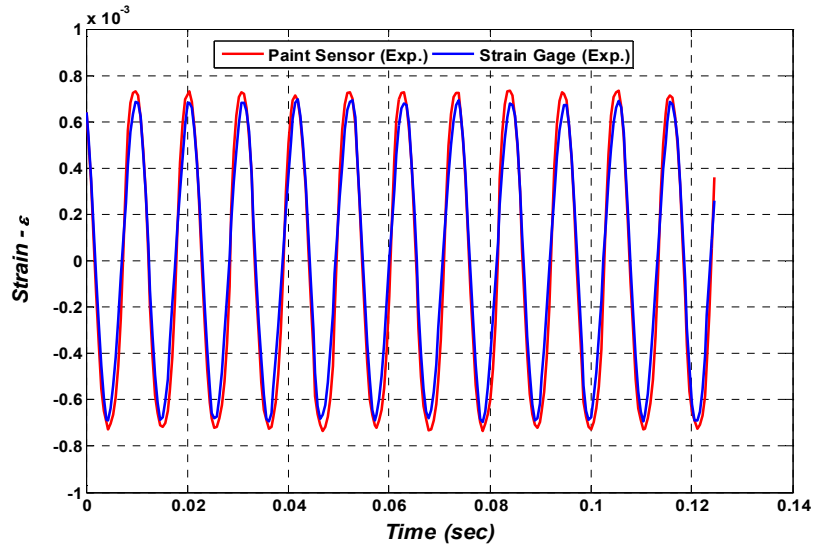
Figure 4.19: Comparison between the strains measured by the paint and the strain gage sensors at the third mode of vibration Frequency (94.27 Hz)

4.4.3 Frequency response characteristics

The dynamic characteristics of the smart paint sensor are measured in the frequency domain by subjecting the beam/sensor assembly to swept sine wave excitation. Comparisons are also established between the sensor response and that of conventional strain gage sensor in order to determine the merits and limitations of the smart paint sensor.

In this section, the frequency response and transfer function characteristics are presented when the beam/sensor system.

a. Typical Frequency Response

A typical frequency response of the un-poled smart paint and the strain gage sensors are shown in Figure 4.20. Note that the paint sensor has a clear distortion between the second and third modes of vibration.
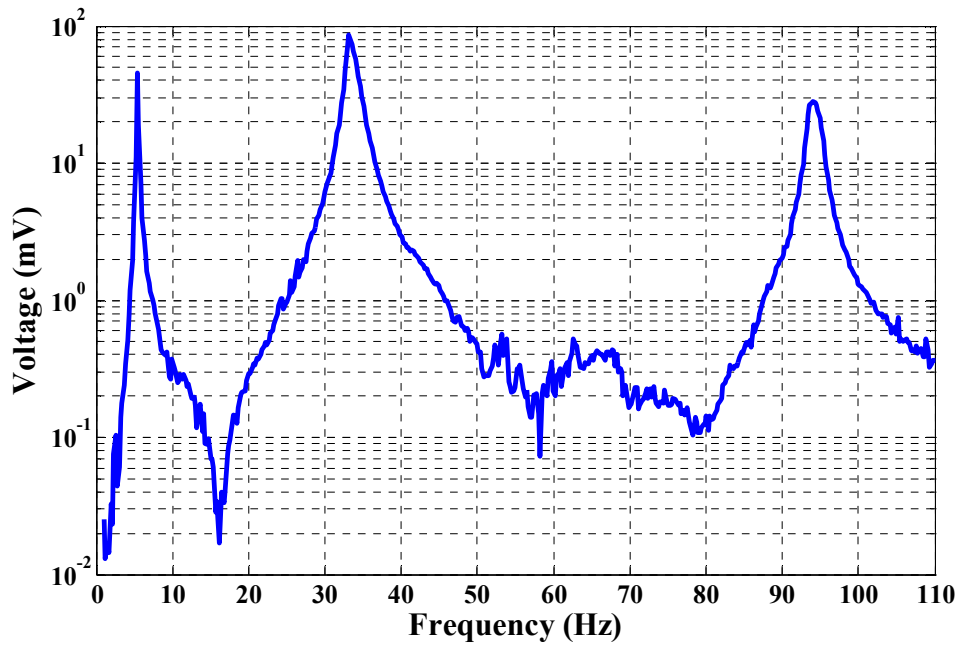
(a) – smart paint sensor
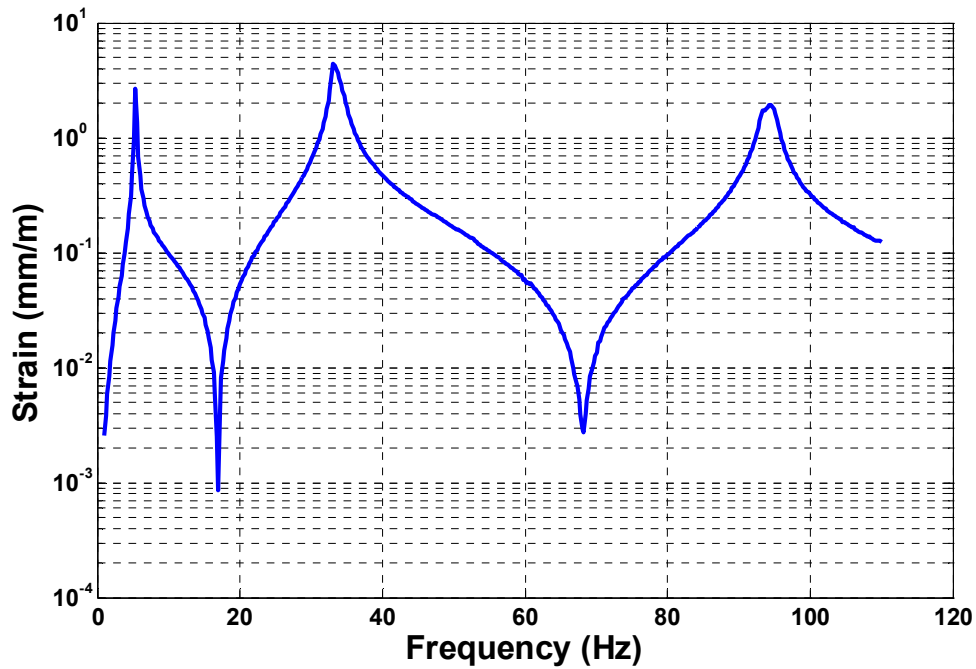
(b) – strain gauge

Figure 4.20: Comparison between the frequency response of the smart paint sensor and the strain gage

b. Effect of Poling on the Frequency Response

Figure 4.21 displays the sequence of improvements that the smart paint sensor undergoes following the initial poling by 10 volts for a period of 5 minutes. The displayed results are recorded before poling, immediately after poling, and then five days after poling on steps of one day. It is clear that the distortion between the second and third modes of vibration decreases gradually and after the fifth day, the smart sensor dramatically replicates the response of the strain gage which is shown in Figure 4.21h for the sake of comparison.

**c. Comparison between Frequency Response Characteristics of the Paint
Sensor and Strain Gage**

Figure 4.22 shows a comparison between frequency response characteristics of the paint sensor and strain gage. The displayed results demonstrate again the accuracy of the paint sensor in monitoring the exact state of strain in the frequency domain as measured by the strain gage.
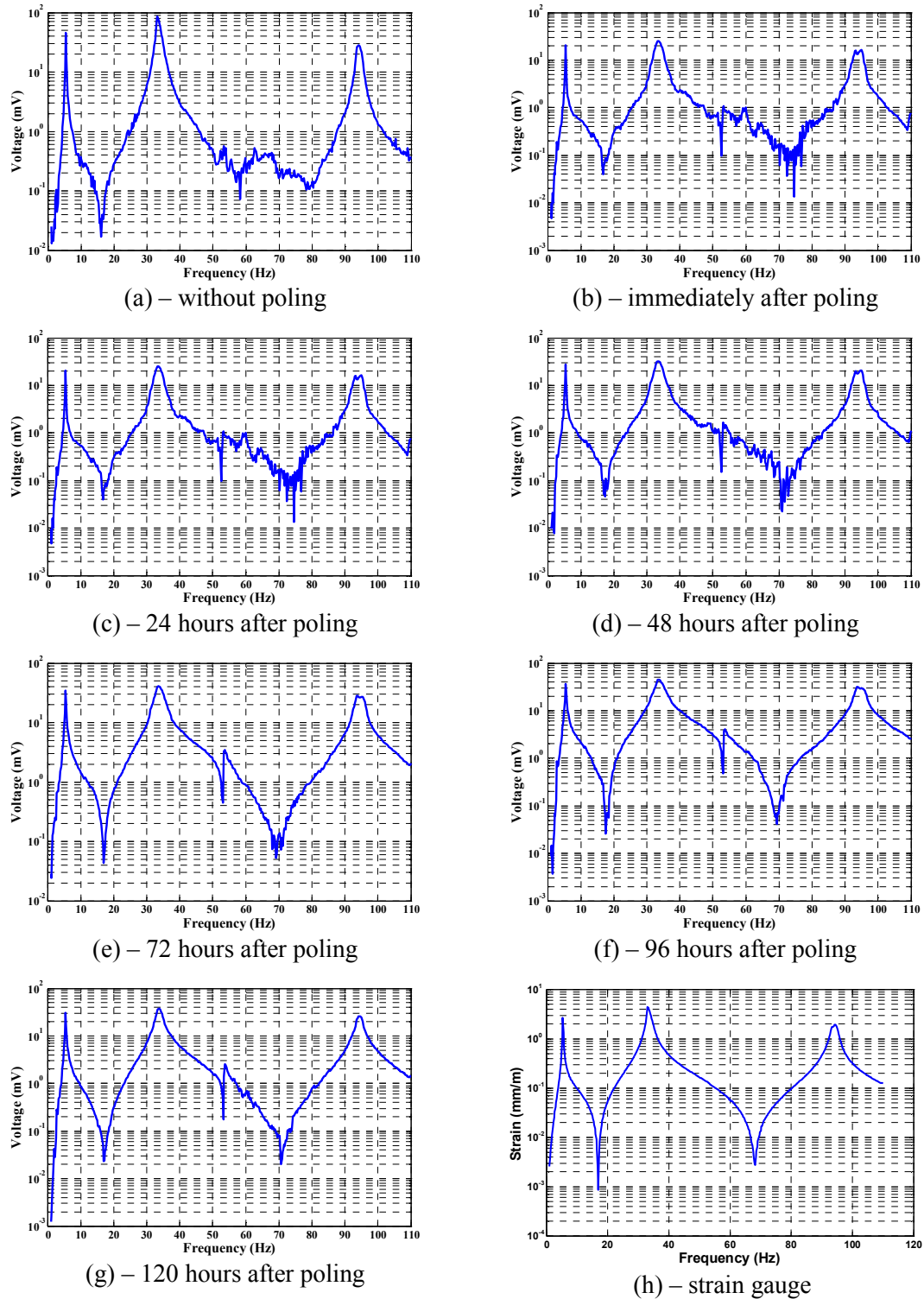
Figure 4.21: Effect of duration after poling on the frequency response of the smart paint sensor and the strain gage
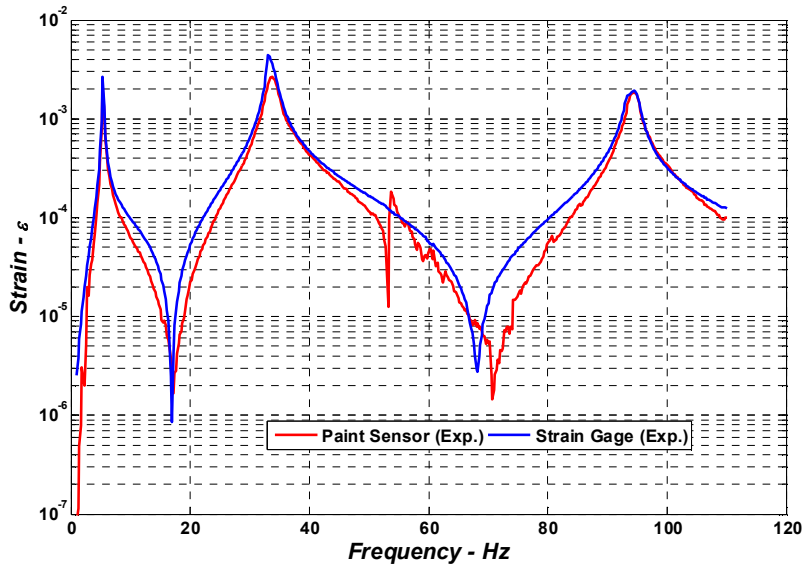
Figure 4.22: The frequency response of the smart paint sensor and the strain gage

d. Transfer Function of the Paint Sensor

i. Typical transfer function characteristics

A typical transfer function characteristics of the un-poled smart paint and the strain gage sensors are shown in Figure 4.23. Note that the transfer function quantifies the relationship between the sensor output and the excitation input to the shaker. It is evident that the transfer function of the paint sensor exhibits considerable distortions both in the magnitude and the phase angle as compared to the clean transfer function of the strain gage sensor.

ii. Effect of poling on the transfer function characteristics

Figure 4.24 displays the sequence of improvements that the transfer function of the smart paint sensor undergoes following the initial poling by 10 volts for a period of 5 minutes
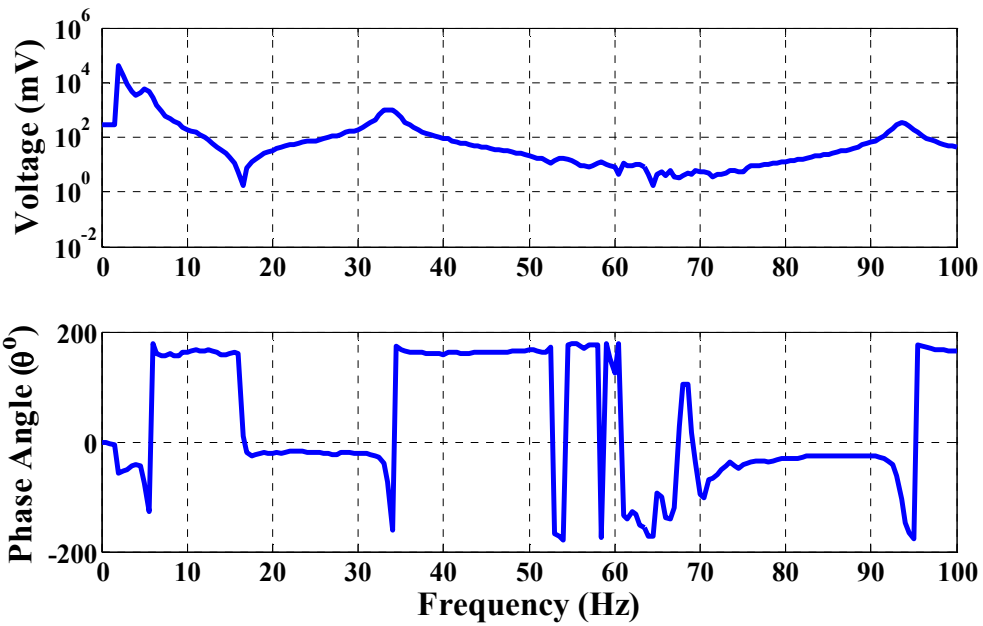
(a) – smart paint sensor
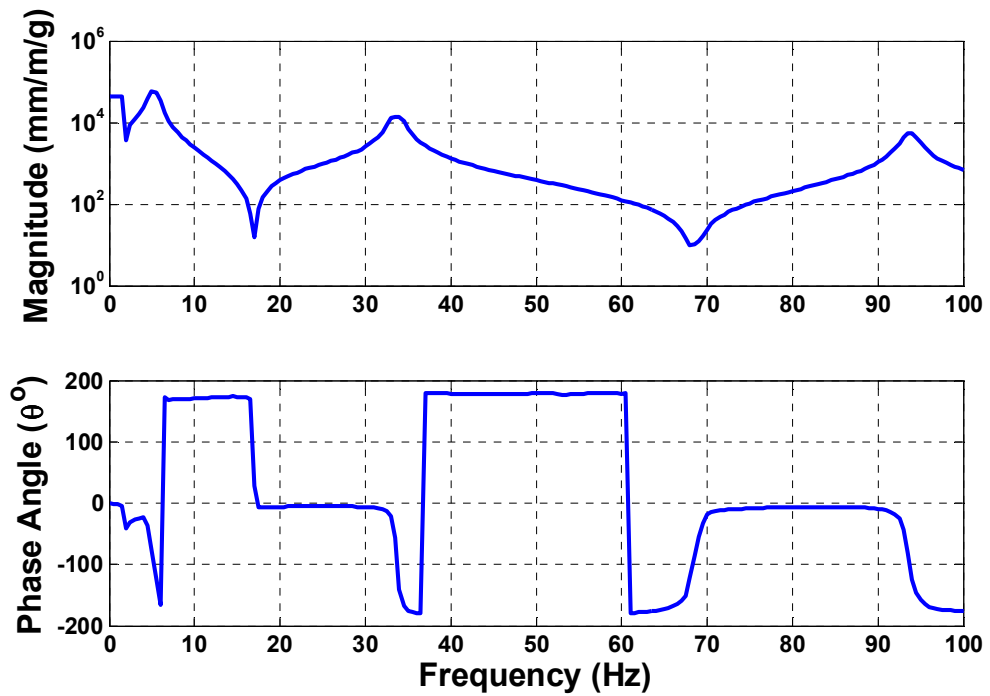
(b) – strain gauge sensor

Figure 4.23: Comparison between the transfer function of the smart paint sensor and the strain gage

(a) – without poling

(b) – immediately after poling

(c) – 24 hours after poling

(d) – 48 hours after poling

(e) – 72 hours after poling

(f) – 96 hours after poling

(g) – 120 hours after poling
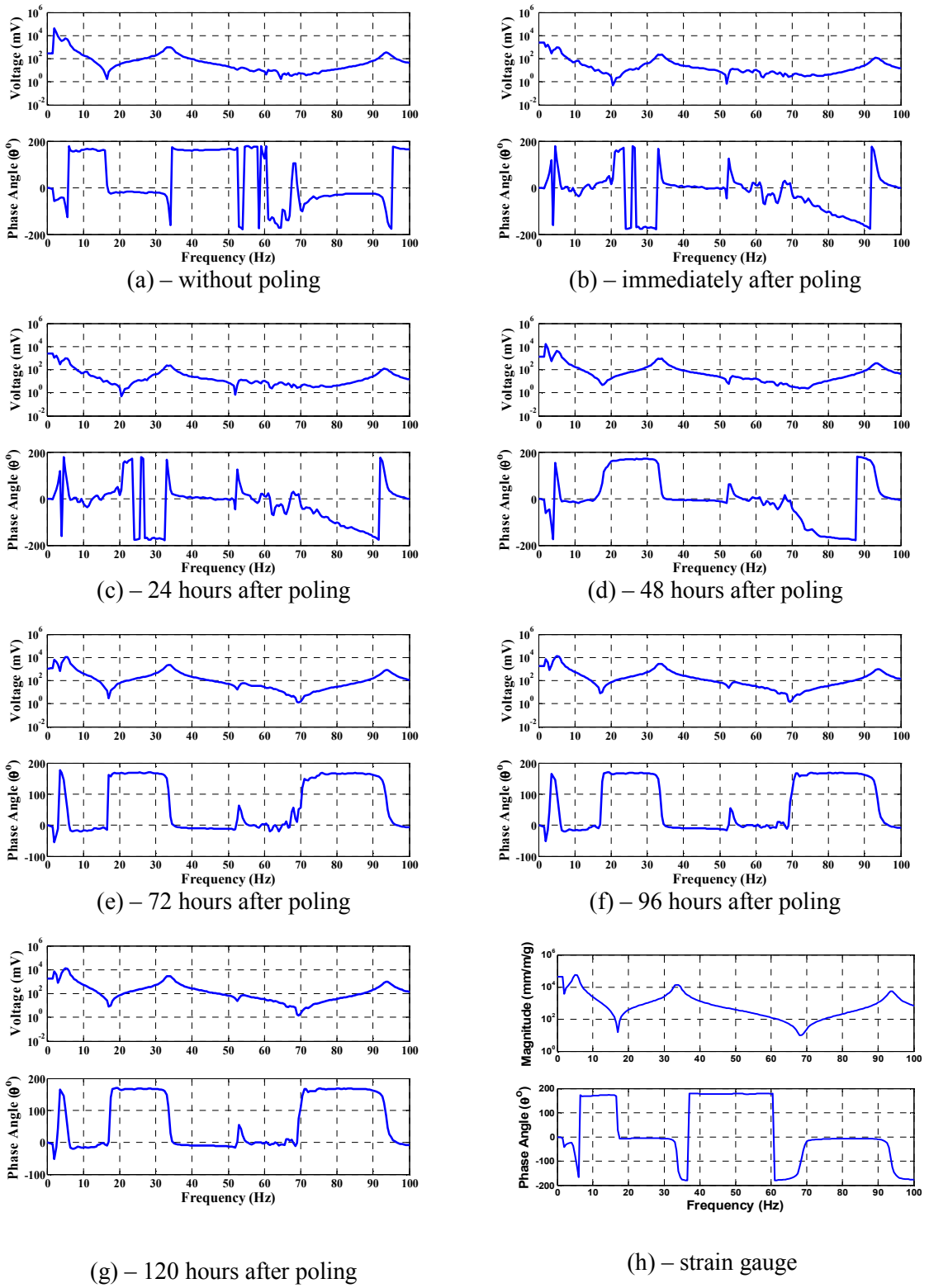
(h) – strain gauge

Figure 4.24: Effect of duration after poling on the phase angle of the transfer function of the smart paint sensor and the strain gage

The results displayed in Figure 4.24 are recorded before poling, immediately after poling, and then five days after poling on steps of one day. It is clear that the distortions both in the magnitude and phase angle of the transfer function, particularly between the second and third modes of vibration, decreases gradually. After the fifth day, the smart sensor dramatically replicates the response of the strain gage which is shown in Figure 4.24h for the sake of comparison.

4.5 Summary

This chapter has presented a comprehensive testing and evaluation of the experimental characteristics of the smart paint sensor. The effects of the carbon black content and load on the piezoresistive characteristics of the sensor are determined. These characteristics define the percolation threshold of the sensor and the effect of the applied strain on the output of the sensor. The viscoelastic properties of the sensor which are namely: its storage modulus and loss factor are also measured as functions of the operating temperature.

The dynamic characteristics of the sensor as quantified by its time and frequency response are measured for up-poled sensor and compared with conventional strain gage sensor. These characteristics reveal high distortions, nonlinearity, and asymmetry of the sensor output as compared to that of conventional strain gages. The application of low poling voltage of 10 volts for short period of time of 5 minutes has radically improved the performance of the sensor especially if the sensor is left to cure for five days. Following such a curing period, the

distortions, nonlinearity, and asymmetry are eliminated completely and the sensor was able to replicate exactly the characteristics of conventional strain gages. The performance of the sensor is checked against that of a strain gage in both the time and frequency domains. In the time domain, the response is checked for the first three modes of vibration of the beam/sensor assembly. In the frequency domain, the frequency response and the transfer function of the sensor are also checked against the corresponding characteristics of the strain gage sensor.

Chapter 5: Finite Element Modeling of Sensor/Structure Assembly

5.1 Overview

This chapter presents a finite element model of the paint sensor/structure assembly that can predict the strain and the output voltage as monitored by the sensor. The model is a one-dimensional model which is based on the Bernoulli-Euler beam theory. It integrates with it the sensor equations, developed in Chapter 4, which are primarily equations 4.7 and 4.14.

5.2 The Finite Element Model

The model divides the beam and sensor assembly into N finite elements sensor as shown in Figure 5.1
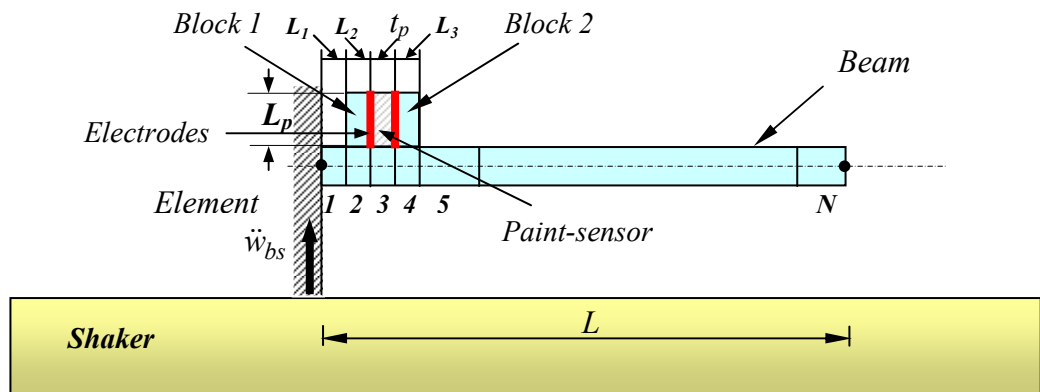
Figure 5.1: Finite element model of the beam/paint sensor assembly

5.2.1 Beam element

Examples of the beam elements are elements 1, 2, 4, 5,..., N as shown in Figure 5.1. A typical schematic drawing for any of these elements is shown in Figure 5.2.
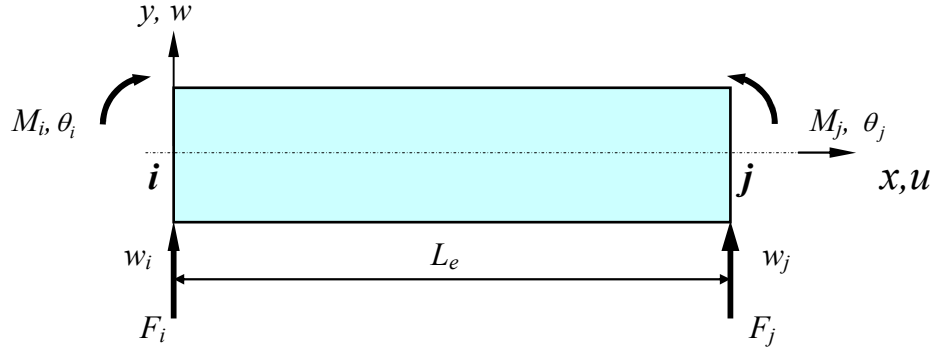
Figure 5.2: Bernoulli-Euler beam element

The beam element has constant area moment of inertia I, modulus of elasticity E and length L. Acting on the beam element are the external transverse loads (F_i and F_j) and moments (M_i and M_j). These loads and moments are external disturbances or loads acting on the element. The element has

The kinetic (KE_b) and potential (PE_b) energies of the beam element are given by:

$$KE_b = \tfrac{1}{2}m_b \int_0^{L_e} \dot{w}^2 \, dx \tag{5.1}$$

and

$$PE_b = \tfrac{1}{2}E_b I_b \int_0^{L_e} w_{,xx}^2 \, dx \tag{5.2}$$

where m_b and $E_b I_b$ denote the mass per unit length and the flexural rigidity of beam respectively. Also, w and $w_{,xx}$ denote the transverse deflection and curvature respectively. Note that $,xx$ denotes second partial derivative with respect to x.

Using the classical finite element cubic interpolating equation:

$$w = \{N\}\{\delta_e\} \tag{5.3}$$

Where $\{N\}$ = interpolating vector and $\{\delta_e\}$ = nodal displacement vector =

$\{\delta_e\} = \{w_i \ \theta_i \ w_j \ \theta_j\}^T$ with w_i and θ_i denoting the transverse and angular deflections of

node i respectively.

Substituting equation 5.3 into equations 5.1 and 5.2, gives:

$$KE_b = \tfrac{1}{2} \ \{\dot{\delta}_e\}^T [M_e]\{\dot{\delta}_e\}, \tag{5.4}$$

and
$$PE_b = \tfrac{1}{2} \{\delta_e\}^T [K_e]\{\delta_e\}. \tag{5.5}$$

where $[M_e] = \displaystyle\int_0^{L_e} m_b \{N\}^T \{N\} dx$ = element mass matrix

and $[K_e] = \tfrac{1}{2} \displaystyle\int_0^{L_e} E_b I_b \{N_{,xx}\}^T \{N_{,xx}\} dx$ = element stiffness matrix.

5.2.2 Beam/sensor element

Example of the beam/sensor element is element 3 in Figure 5.1. A detailed

schematic drawing of the element is shown in Figure 5.3.
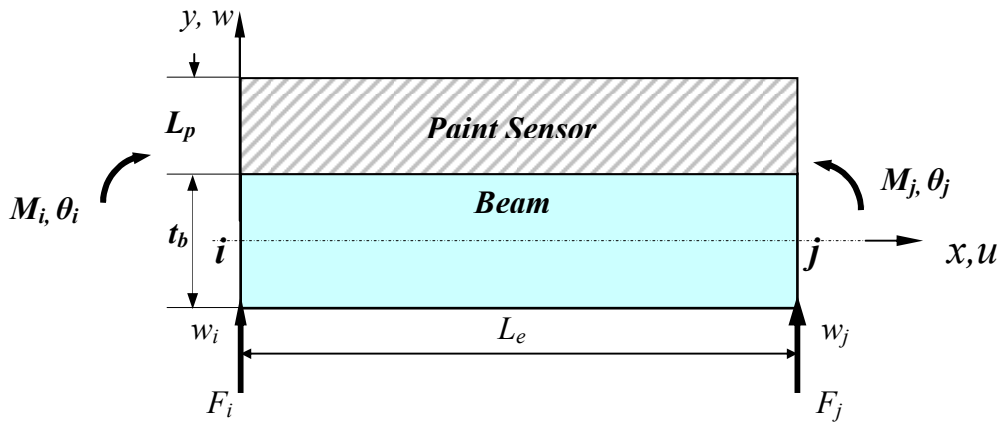
Figure 5.3: Beam/Sensor element

The kinetic ($KE_{b/s}$) and potential ($PE_{b/s}$) energies of the beam/sensor element are given by:

$$KE_{b/s} = \tfrac{1}{2}m_t \int_0^{L_e} \dot{w}^2 \, dx \qquad (5.6)$$

and

$$PE_{b/s} = \tfrac{1}{2}E_t I_t \int_0^{L_e} w_{,xx}^2 \, dx \qquad (5.7)$$

where $m_t=m_b+m_s$ and $E_t I_t=E_b I_b+E_s I_s$ denote the total mass per unit length and the total flexural rigidity of beam/sensor assembly respectively. Subscripts b and s denote beam and sensor respectively.

Using the finite element cubic interpolating equation 5.3, equations 5.6 and 5.6 reduce to:

$$KE_{b/s} = \tfrac{1}{2} \{\dot{\delta}_e\}^T [M_{e_{b/s}}]\{\dot{\delta}_e\}, \qquad (5.8)$$

and

$$PE_{b/s} = \tfrac{1}{2} \{\delta_e\}^T [K_{e_{b/s}}]\{\delta_e\}. \qquad (5.9)$$

where $[M_{e_{b/s}}] = \int_0^{L_e} m_t \{N\}^T \{N\} \, dx =$ element mass matrix

and $\quad [K_{e_{b/s}}] = \tfrac{1}{2}\int_0^{L_e} E_t I_t \{N_{,xx}\}^T \{N_{,xx}\} \, dx =$ element stiffness matrix.

5.2.3 Equation of motion of element

Let **L** denotes the Lagrangian of the beam system, then **L** is given by:

$$\mathbf{L} = KE - PE \qquad (5.10)$$

and the equation of motion of the beam is given by:

$$\frac{d}{dt}\left(\frac{\partial \mathbf{L}}{\partial \{\dot{\delta}_e\}} \right) - \frac{\partial \mathbf{L}}{\partial \{\delta_e\}} = \{Q_e\} \qquad (5.11)$$

where $\{Q_e\}$ is the vector of external loads and moments acting on element = $\{F_i, M_i, F_j, M_j\}^T$.

Equations 5.4, 5.5, and 5.8 through 5.11 yield:

$$[M_e]\{\ddot{\delta}_e\}+[K_e]\{\delta_e\}=\{Q_e\} \tag{5.12}$$

5.2.4 Assembly of element matrices

Assembly of the stiffness and mass matrices of the individual elements aims at forming the overall (or global) matrices of the entire beam/sensor system. During such a process, the compatibility of the deflections of the neighboring elements at the common nodes connecting them must be ensured. Also, the equilibrium conditions of the forces and moments acting at the nodes must be guaranteed.

Let $\{\delta\}$ be the vector of nodal deflections of the entire beam/sensor assembly = $\{w_1\ \theta_1\ w_2\ \theta_2\ w_3\ \theta_3 ....w_N\ \theta_N\}^T$, with N denoting number of nodal points. Then, the compatibility and equilibrium conditions require that:

$$\sum_{e=1}^{n} [M_e]\{\ddot{\delta}_e\}+\sum_{e=1}^{n} [K_e]\{\delta_e\}=\sum_{e=1}^{n} \{Q_e\} \tag{5.13}$$

or
$$[M]\{\ddot{\delta}\}+[K]\{\delta\}=\{Q\} \tag{5.14}$$

where n and $\{Q\}$ are the number of elements and the vector of global forces and moments acting on the beam. Also, $[M]$ and $[K]$ are the overall mass and stiffness matrices of the beam/sensor.

5.2.5 Boundary conditions and base excitation

The boundary conditions of the beam/sensor assembly are taken into account by eliminating the restrained degrees of freedom associated with the base which is anchored to the shaker. This results in the reduced stiffness and mass matrices $[K_0]$ and $[M_0]$. Also, the shaker excitation $\ddot{w}_{bs}$ is included resulting in the following system equation of motion:

$$[M_o]\{\ddot{Z}\} + [K_o]\{Z\} = \{Q\} + [M_o]\{B\}\ddot{w}_{bs}$$

where $\{Z\} = \left\{w_2 - w_{bs}, \ w_{2,x}, \ w_3 - w_{bs}, \ w_{3,x}, \ldots\ldots, \ w_{N+1} - w_{bs}, \ w_{N+1,x}\right\}^T$

and $\{B\} = \{1 \ \ 0 \ \ 1 \ \ 0 \ \ldots\ldots\ldots\ldots 1 \ 0\}^T$

5.2.6 Sensor output voltage

The voltage output from the paint sensor, which is fitted to the eth element can be determined by considering the deformation of the sensor as the beam/sensor assembly vibrates as shown in Figure 5.4.
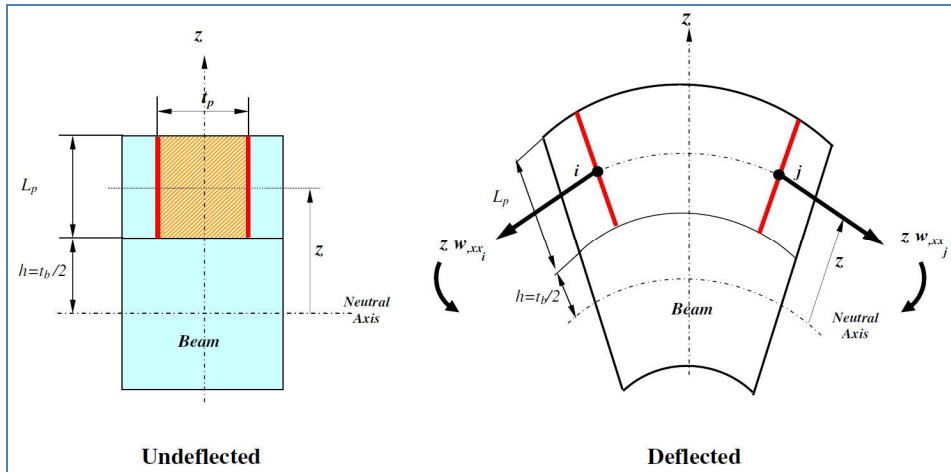
Figure 5.4: Deflection of the paint sensor

Total strain in the paint sensor at location z is:

$$\varepsilon = z\left(w_{i,xx} + w_{j,xx}\right) \tag{5.16}$$

The nodal deflections w_i, $w_{i,x}$, w_j and $w_{j,x}$ are obtained from the finite element model. Then, $w_{i,xx}$ and $w_{j,xx}$ can be determined from the following shape function:

$$w = a_1 + a_2 x + a_3 x^2 + a_4 x^3 \tag{5.17}$$

Differentiating equation 5.17 twice with respect to x gives:

$$w_{i,xx} = 2a_3 \quad , \quad w_{j,xx} = 2a_3 + 6a_4 t_p \tag{5.18}$$

Hence, a_3 and a_4 are to be obtained from,

$$\begin{Bmatrix} a_1 \\ a_2 \\ a_3 \\ a_4 \end{Bmatrix} = \begin{pmatrix} 1 & 0 & 0 & 0 \\ 0 & 1 & 0 & 0 \\ 1 & t_p & t_p^2 & t_p^3 \\ 0 & 1 & 2t_p & 3t_p^2 \end{pmatrix}^{-1} \begin{Bmatrix} w_i \\ w_{i,x} \\ w_j \\ w_{j,x} \end{Bmatrix} \tag{5.19}$$

Then, the values of $w_{i,xx}$ and $w_{j,xx}$ are then used in equation 5.16 to obtain the strain and equation 4.14 can be used to compute the output voltage of the sensor.

5.3 Performance of the Paint Sensor

5.3.1 The main parameters of the beam/sensor assembly

Table 5.1 lists the main geometrical and physical parameters of the beam/sensor system which is shown in Figures 4.7, 4.8, 4.10, and 5.1.

Table 5.1: The main geometrical and physical parameters of the beam/sensor system

PARAMETER	VALUE
Beam	
L	0.35 *m*
L_1, L_2, L_3	0.00687 *m*
t_b	0.003125 *m*
w_b	0.03125 *m*
Density	1,180 kg/m^3
Young's modulus	1.8 *GPa*
Sensor	
t_p	0.001 *m*
L_p	0.00156 *m*
Density	1,000 kg/m^3
Young's modulus	18 *MPa*

5.3.2 Predictions of resonant frequencies

The predictions of the resonant frequencies of the beam/sensor assembly by the finite element model are listed in Table 5.2 along with the experimentally measured values. It can be seen that the predictions are in excellent agreement with the experimental values.

Table 5.2: Theoretical and experimental resonant frequencies

MODE	THEORETICAL FREQUENCY (HZ)	EXPERIMENTAL FREQUENCY (HZ)	ERROR (%)
1	5.41	5.37	0.74
2	33.86	33.11	2.26
3	94.60	94.27	0.35

5.3.3 Performance of the sensor in the time domain

Figures 5.5, 5.6, and 5.7 show comparisons between the theoretical predictions and the experimental results when the beam/sensor system is excited at its first three modes of vibration. In all these figures, the predictions of the strain by the

finite element model are compared with the strain gage output. Also, the theoretical predictions of the output voltage of the paint sensor are compared with the experimental measurements. These comparisons are intended to validate the theoretical model.

It is clear from the figures that the predictions are in excellent agreement with the experimental results for the first and third modes of vibration while there are some discrepancies for the second mode.
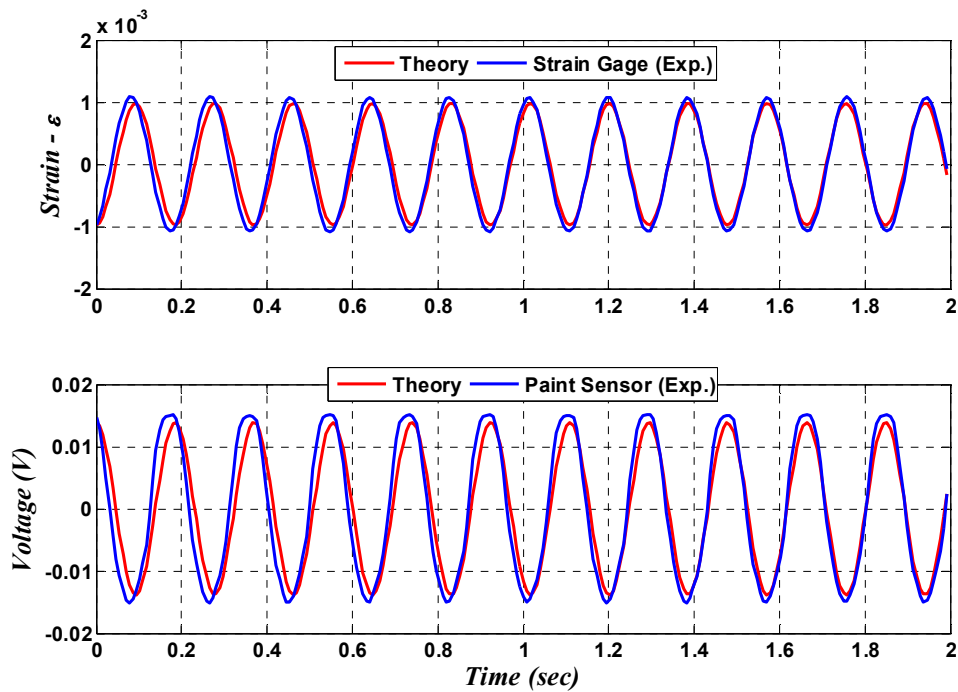
Figure 5.5: Theoretical and experimental performance of the paint sensor and the strain gage when the beam/sensor system is excited at the first mode of vibration (5.360 Hz)
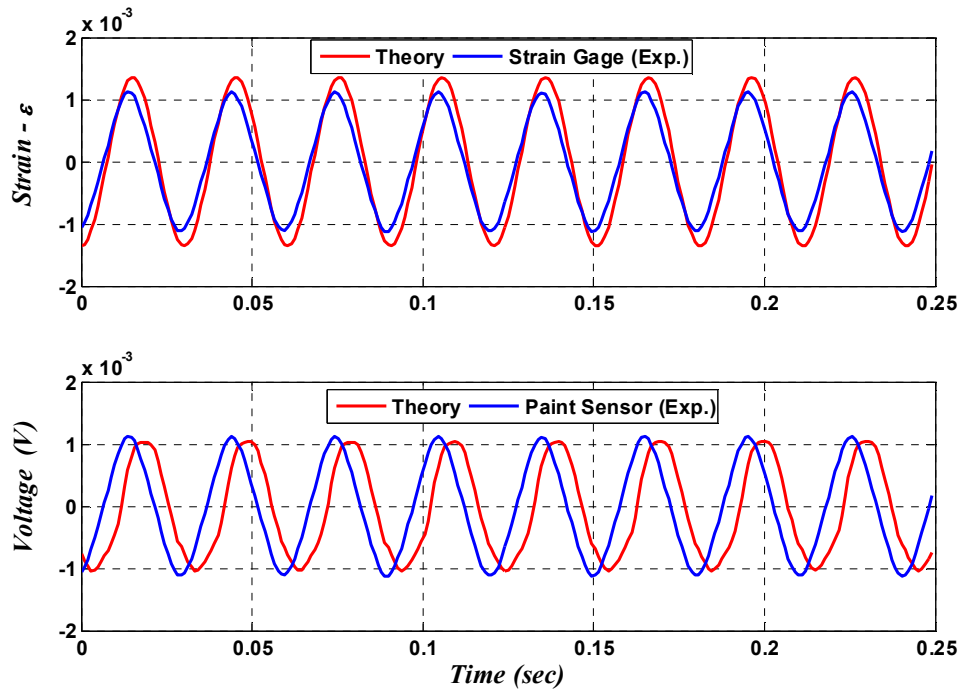
Figure 5.6: Theoretical and experimental performance of the paint sensor and the strain gage when the beam/sensor system is excited at the second mode of vibration (33.11 Hz)
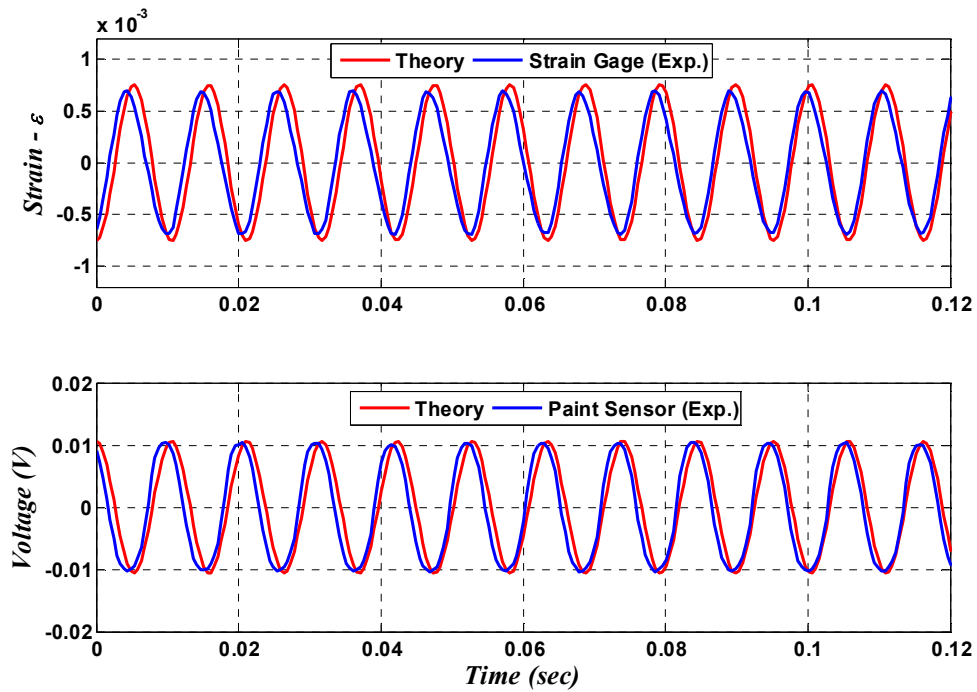
Figure 5.7: Theoretical and experimental performance of the paint sensor and the strain gage when the beam/sensor system is excited at the second mode of vibration (94.27 Hz)

5.3.4 Performance of the sensor in the frequency domain

Figure 5.8 shows comparisons between the theoretical predictions and the experimental results when the beam/sensor system is excited by a swept sinusoidal excitation. The magnitude of the excitation acceleration is shown in the top graph of Figure 5.8. In the figure, the predictions of the strain by the finite element model are compared with the strain gage output. Also, the theoretical predictions of the output voltage of the paint sensor are compared with the experimental measurements.

It is clear from the figure that the predictions are in adequate agreement with the experimental results at the resonant frequencies while there are some discrepancies at the anti-resonant frequencies.
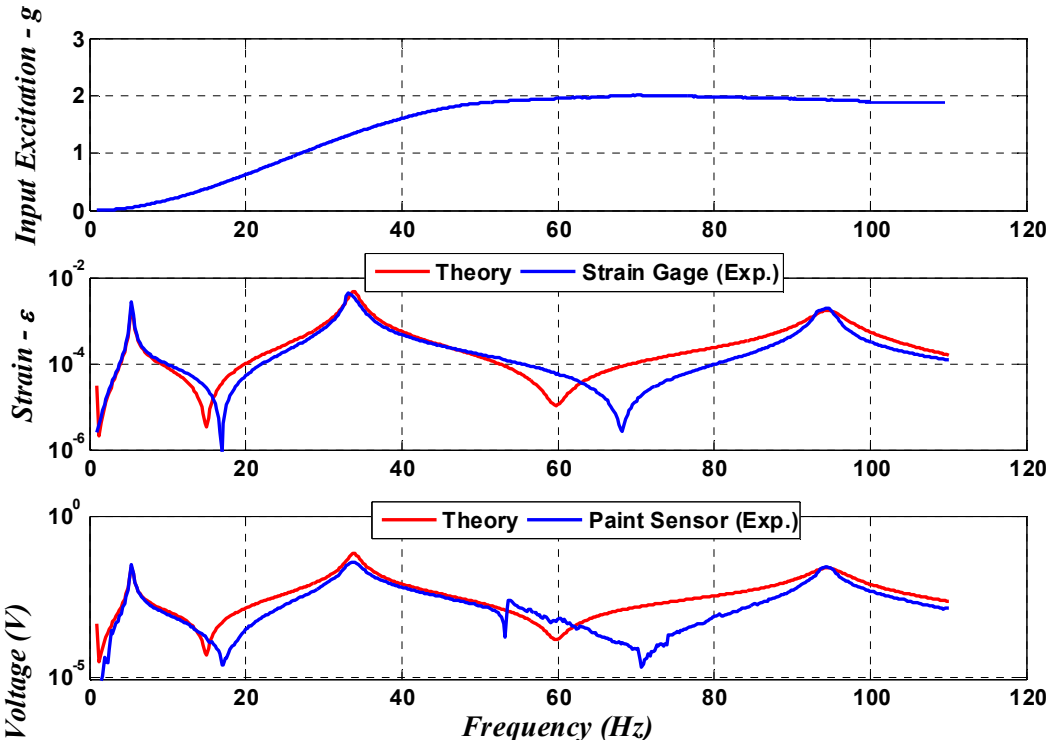
Figure 5.8: Theoretical and experimental performance of the paint sensor and the strain gage when the beam/sensor system is excited by swept sinusoidal excitation

5.4 Summary

This chapter has presented a finite element model of the beam/sensor assembly. The model predicts the strain and the output voltage as monitored by the sensor. The predictions of the model are validated against the experimental results obtained by both the paint sensor and the strain gage both in the time and the frequency domains.

It is found that the model is, in general, capable of predicting the resonant frequencies, the strain, and the output voltage very accurately. However, some discrepancies are observed when predicting the time response of the second mode of vibration and the anti-resonant frequencies in the frequency response.

Chapter 6: Conclusions and Future Work

6.1 Conclusions

This dissertation has presented a class of smart paint sensors for monitoring the structural vibration of beams. The sensor is manufactured from an epoxy resin which is mixed with carbon black nano-particles to make it electrically conducting and sensitive to mechanical excitations.

A comprehensive theoretical and experimental investigation is presented to understand the underlying phenomena governing the operation of this class of paint sensors and evaluate its performance characteristics. A theoretical model is developed to model the electromechanical behavior of the sensor system as a lumped-parameter system using the Debye and the Cole–Cole equations.

Also, the sensor equations are integrated with a finite element model of a base beam to which the sensor is bonded to. The resulting multi-field model is utilized to predict the behavior of both the sensor and the beam when subjected to a wide variety of vibration excitations. The predictions of the multi-field finite element model are validated experimentally and the behavior of the sensor is evaluated both in the time and the frequency domains. The performance of the sensor is compared with the performance of conventional strain gages to emphasize its potential and merits.

It is observed that the model is, in general, capable of predicting the resonant frequencies, the strain, and the output voltage very accurately. However, some

discrepancies are observed when predicting the time response of the second mode of vibration and the anti-resonant frequencies in the frequency response.

It is important here to note that this dissertation has introduced, for the first time, the technique of poling carbon black/polymer composites in order to overcome the serious problems that hampered the practical application of this class of composites. These problems included inaccurate tracking of the true strain state, distortion of the shape of the wave form of the true strain, inaccurate tracking of bidirectional cyclic loading in particular, as well as nonlinear behavior and asymmetric behavior when measuring bidirectional cyclic loading in particular. With low voltage and duration poling, most of these serious limitations were eliminated.

6.2 Future Work

Although this dissertation has addressed many of the fundamental issues related to the manufacturing, modeling, and experimental application of smart paint sensors, it opened the door for many more issues that need to be addressed in future studies. Among the most pressing issues that required immediate attention is to investigate the physical reasons behind why poling has dramatically improved the performance of the paint sensor. Microstructure and electron microscopy analysis is essential to understanding of the rearrangement of the conduction paths that may have resulted from poling. Such analysis should be carried out over extended period of time in order to reveal the effect of the curing on the progression of the conduction paths and rearrangement of the carbon black particles.

More work is needed to study in depth the effect that carbon black particles have on the viscoelastic properties of CB/polymer composites. With such information, it would be possible to improve the mathematical model by incorporating the viscoelastic model of the CB/polymer composites into the finite element model.

Further work is needed to incorporate the Debye or Cole-Cole models of the CB/polymer composites into the finite element model to account for the capacitive and inductive components that were ignored in the present study.

A natural extension of the present study is to develop the smart paint sensor for monitor the vibration and structural power flow of two dimensional structures. Also, it would be beneficial to extend the application of the smart paint sensor for monitoring noise, multi-dimensional acoustic fields, and targets both in air and underwater.

References

Abot J. L., Schulz M. J., Song Y., Medikonda S., and Rooy N., "Novel distributed strain sensing in polymeric materials", *Smart Mater. Struct.*, Vol. 19, 085007, 2010.

Aggarwal M. L., Khan R. A. and Agrawal V. P., "Optimization of Smart Paint Thickness in Structures", July 28-30, 2005, Bangalore, India ISSS-2005/PS-11.

Aldraihem O., W. Akl, and, A. Baz, "Nanocomposite Functional Paint for Vibration and Noise Monitoring", *Sensors & Actuators: A. Physical*, Vol. 149, pp. 233-240, 2009.

Bhattacharyya S. K., *Metal-Filled Polymers: Properties and Applications*, ISBN: 0824775554 - Marcel Dekker, NY, 1986.

Coler M. A., "Conductive plastics and method of making the same", *US Patent* 2,683,669, filed on 15 April 1950.

Das, N.C., Chaki, T.K., and Khastgir, D., "Effect of axial stretching on electrical resistivity of short carbon fibre and carbon black filled conductive rubber composites," *Polymer International*, Vol. 51, pp. 156-163, 2002.

Egusa S. and Iwasawa N., "Piezoelectric paints as one approach to smart structural materials with health-monitoring capabilities", *Journal of Smart Materials & Structures*, Vol. 7, pp. 438-445, 1998.

Flandin L., A. Chang, S. Nazarenko, A. Hiltner, E. Baer, "Effect of strain on the properties of an ethylene-octene elastomer with conductive carbon fillers", *Journal of Applied Polymer Science,* Volume 76, Issue 6 , Pages 894 – 905, 2000.

Gregory J. W. and Sullivan J. P., Wanis S. S., and Komerath N. M., "Pressure-sensitive paint as a distributed optical microphone array", *Journal of the Acoustical Society of America*, Vol. 119, No.1, pp. 251-261, January 2006.

Hale J. M., "Response to Application of Piezoelectric Paints to Damage Detection in Structural Materials", *Journal of Reinforced Plastics and Composites*, Vol. 17, No 4, 1998a.

Hale J. M., "Thick Film Strain Transducers Based on Piezoelectric Paint", *Proc. Computational Methods for Smart Structures and Materials* - SMART 98, Rome September 1998b.

Hale J. M. and Tuck J., "A Novel Thick-Film Strain Transducer Using Piezoelectric Paint", *Proc. 1MechE Part C: J of Mechanical Engineering Science,* Vol.213, No.C6, 1999.

Hilmans, H.A.C., "Equivalent circuit representation of electromechanical transducers: I. Lumped-parameter systems," *Journal of Micromechanics and Microengineering*, Vol. 6, pp. 157-176, 1996.

Hyatt T., "Piezoresistive Nano-Composites: Characterization and Applications", *Masters Thesis*, Brigham Young University, 2010.

Ikeda, T., *Fundamental of Piezoelectricity*, Oxford Press, New York, 1996.

Inman, D. J., *Engineering Vibration*, 3rd Edition, Pearson Education, New York, 2007.

Inzelt G., *Conducting Polymers: A New Era in Electrochemistry*, Springer, pp. 265–269, 2008.

Kimura, T., Yoshimura, N., Ogiso, T., Maruyama, K., and Ikeda, M., "Effect of elongation on electric resistance of carbon-polymer systems [I]," *Polymer*, Vol. 40, pp. 4149-4152, 1999.

Knite, M., Teteris, V., Kiploka, A., and Kaupuzs, J., "Polyisoprene-carbon black nanocaomposites as tensile strain and pressure sensor materials," *Sensors and Actuators A: Physical*, Vol. 110, pp. 142-149, 2004.

Kost J., M. Narkis, A. Foux, "Effects of axial stretching on the resistivity of carbon black filled silicone rubber", *Polymer Engineering and Science*, Vol. 23, No. 10, Pages 567-571, 1983.

Li Z., Dharap P., Nagarajaiah S., Barrera E. V., and Kim J. D., "Carbon nanotube film sensors," *Adv. Mater.*, Vol. 16, No. 7, pp. 640–643, 2004.

Loh K. J., Lynch J. P., Shim B. S. and **Kotov N. A., "**Tailoring Piezoresistive Sensitivity of Multilayer Carbon Nanotube Composite Strain Sensors", *Journal of Intelligent Material Systems and Structures*, Vol. 19, No. 7, pp. 747-764, 2008.

Lu, J., Chen, X., Lu, W., and Chen, G., "The piezoresistive behaviors of polyethylene/foliated graphite nanocomposites," *European Polymer Journal*, Vol. 42, pp. 1015-1021, 2006.

Mahar B., C. Laslau, R. Yip, and Y. Sun, "Development of Carbon Nanotube-Based Sensors—A Review", *IEEE Sensors Journal*, Vol. 7, No. 2, pp. 266-284, 2007.

Mainwaring D., Murugaraj P., Mora-Huertas N., and Sethupathi K., " Enhanced electromechanical response of nonpercolating polymer-nanoparticle composite films", *Applied Physics Letters*, Vol. 92, 253303, 2008.

Moshfegh, S., and Ebrahimi, N. G., "Strain sensors based on graphite fillers," *Iranian Polymer Journal*, Vol. 13, pp. 113-119, 2004.

Nadal-Guardia, R., Brosa, A. M., and Dehe, A., "AC transfer function of electrostatic capacitive sensors based on the 1-D equivalent model: application to silicon microphones," *Journal of Micromechanical Systems*, Vol. 12, 2003, pp. 972-978.

Newbury, K. M., and Leo, D. J., "Linear electromechanical model of ionic polymer transducers Part I: model development," *Journal of Intelligent Systems and Structures*, Vol. 14, 2003, pp. 333-342.

Preumont, A., *Mechatronics: Dynamics of Electromechanical and Piezoelectric Systems*, Springer, The Netherlands, 2006.

Rossi, M., *Acoustics and Electroacoustics*, Artech House, Norwood, MA, 1988.

Schwartz G.; Cerveny S.; Marzocca A.J., "A numerical simulation of the electrical resistivity of carbon black filled rubber ", *Polymer*, Vol. 41, No. 17, pp. 6589-6595, 2000.

Shevchenko, V. G., Ponomarenko, A. T., and Klason, C., "Strain sensitive polymer composite material", *Smart Materials and Structures*, Vol. 4, pp. 31-55, 1995.

Shui X. and D. D. L. Chung, "A piezoresistive carbon filament polymer-matrix composite strain sensor", *Smart Mater. Struct.*, Vol. 5, pp. 243–246, 1996.

Sichel, E. K., *Carbon Black-Polymer Composites*, Marcel Dekker, New York, 1982.

Wang X. and Chung D. D. L., "Continuous carbon fibre epoxy–matrix composite as a sensor of its own strain", *Smart Mater. Struct.,* Vol. 5, pp. 796–800, 1996.

Wang Y.-J., Y. Pan, X.-W. Zhang, K. Tan, "Impedance spectra of carbon black filled high-density polyethylene composites", *Journal of Applied Polymer Science*, Vol. 98, No, 3, Pages 1344 – 1350, 2005.

Yu G., M. Q. Zhang, H. M. Zeng, Y. H. Hou, and H. B. Zhang, "Effect of Filler Treatment on Temperature Dependence of Resistivity of Carbon-Black-Filled Polymer Blends", *Journal of Applied Polymer Science*, Vol. 73, pp. 489–494, 1999.

Zhang M. Q. and Zeng H. M., *Handbook of Thermoplastics*; Olabisi, O., Ed.; Marcel Dekker: New York, 1997.

Zhang, J-F, and Yi, X-S, "Dynamic rheological behavior of high-density polyethylene filled with carbon black," *Journal of Applied Polymer Science*, Vol. 86, 2002, pp. 3527-3531.

Zhang, X-W, Pan, Y., Zheng, Q., and Yi, X.S., "Piezoresistance of conductor filled insulator composites," *Polymer International*, Vol. 50, pp. 229-236, 2001.

Zhang, X-W, Pan, Y., Zheng, Q., and Yi, X.S., "Time dependence of piezoresistance for conductor-filled polymer composites," *Journal of Applied Polymer Science Part B: Polymer Physics*, Vol. 38, pp. 2739-2749, 2000.

Zhang Y., "Piezoelectric paint sensor for real-time structural health monitoring" Paper # 5765-121, *Sensors and Smart Structures Technologies for Civil, Mechanical, and Aerospace Systems Conference,* SPIE Vol. #5765, ed. by M. Tomizuka, San Diego, CA, 7-10 March 2005.

Zhao Q., Wood J. R., and Wagner H. D., "Stress fields around defects and fibers in a polymer using carbon nanotubes as sensors," *Appl. Phys., Lett.*, Vol. 78, No. 12, 2001.